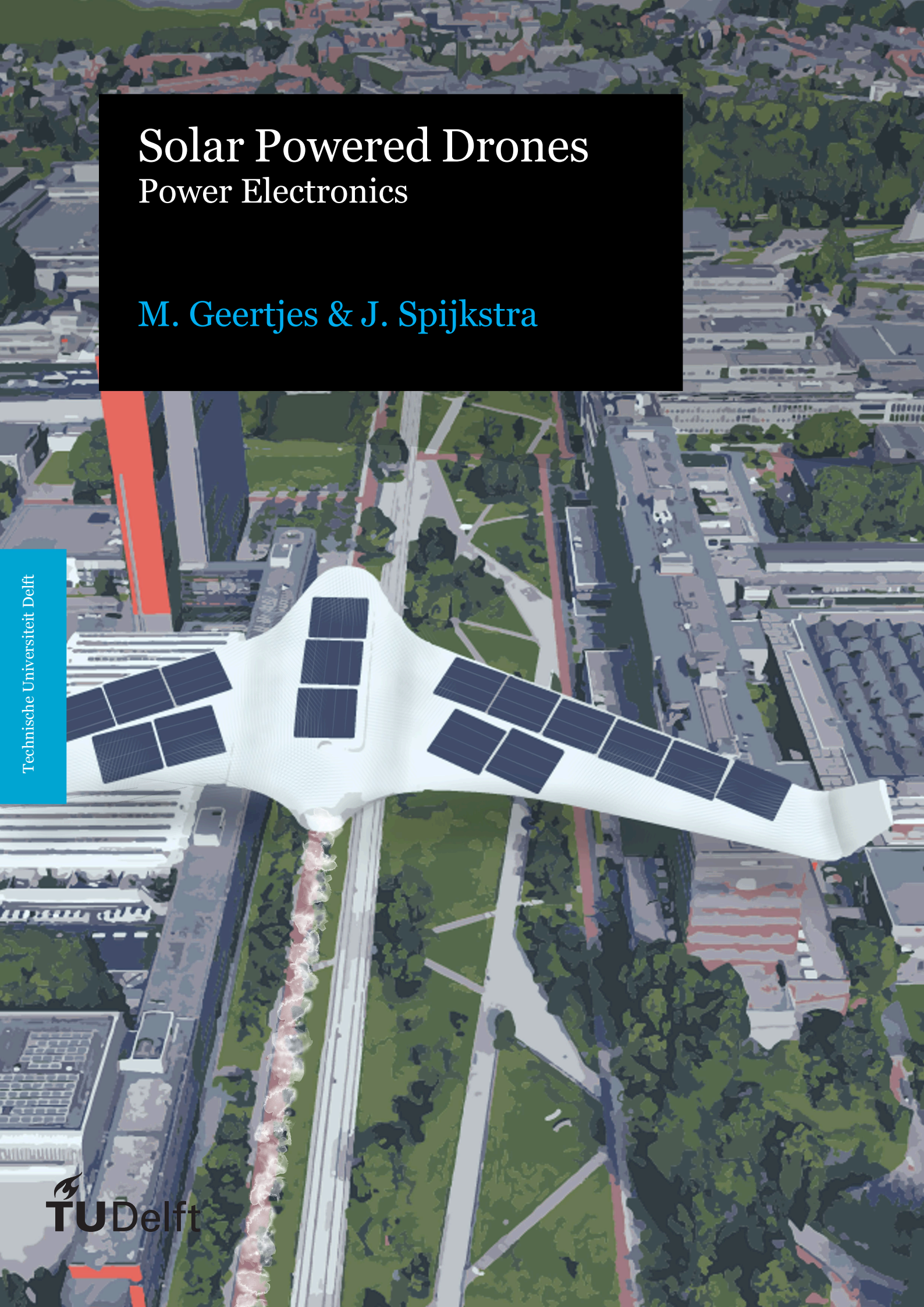


Solar Powered Drones

Power Electronics

M. Geertjes & J. Spijkstra

Technische Universiteit Delft



Solar Powered Drones

Power Electronics

by

M. Geertjes & J. Spijkstra

to obtain the degree of Bachelor of Science
at the Delft University of Technology,
to be defended on Tuesday June 30, 2020 at 13:00 PM.

Project duration: April 20, 2020 – July 3, 2020

Thesis committee: Prof. dr. Ir. J.J.A. Baselmans, TU Delft, Jury Chair
Dr. P. Manganiello, TU Delft, Supervisor
Dr. Ir. G.R. Chandra Mouli, TU Delft, External Assessor
Dr. M. Mutillo, TU Delft, Jury Member

Abstract and preface

Abstract

Sustainable energy technologies are ever-increasing in popularity, not only among companies but also among consumers. Photovoltaic, or PV, cells are amongst the most well known in this field. This project was set up for designing a PV-powered UAV that is able to generate an albedo map of an area equal or bigger than the campus of the TU Delft in a single run. PV cells, however, are highly susceptible to changes in weather conditions and have a range of voltages at which these cells can supply power. Besides that, unnecessary losses occur if the so-called 'Maximum Power Point' (MPP) is not tracked. In this thesis, a boost converter is proposed for the aforementioned system to implement the maximum power point tracking and supply the, by the PV system produced, power as efficiently as possible to the UAV power system.

Preface

We want to extend our sincere thanks to our supervisor Patrizio Manganiello for guiding us through this project. His help has been indispensable in the process, be it in terms of technical support or care and patience. Furthermore, we would also like to thank the assisting supervisors Mirco Muttillio and Andres Calcabrini for their help. We know that the current times have also been challenging for our supervisors and that they did their utmost to bring this project to a successful ending.

Finally, we want to thank our colleagues, Jasmijn Koning and Rik van der Hoorn of the PV generation subgroup and Laura Muntenaar and Sjoerd Groot of the control algorithm and albedo generation subgroup, for their expended efforts and staying with us throughout the project.

*M. Geertjes & J. Spijkstra
Delft, June 2020*

Contents

1	Introduction	1
1.1	Problem analysis	1
1.2	Overview	1
1.2.1	Irradiance	2
1.2.2	Maximum power point tracking	2
1.3	Thesis synopsis	2
2	Requirements	3
2.1	Requirements of the total system	3
2.1.1	Assumptions	3
2.1.2	Mandatory requirements	3
2.1.2.1	Functional requirements	3
2.1.2.2	Non-functional requirements	3
2.1.2.3	Trade off requirements	3
2.2	Power converter requirements	4
2.2.1	Functional requirements	4
2.2.2	Non-Functional requirements	4
2.2.3	Trade-off requirements	4
3	State of the art	5
3.1	Switching type converters	5
3.1.1	PWM converters	5
3.1.1.1	Buck converter	5
3.1.1.2	Boost converter	5
3.1.1.3	(inverting) Buck-Boost converter	5
3.1.1.4	Switched coupled capacitors	7
3.1.2	Switching losses	7
3.1.2.1	Hard switching	7
3.1.2.2	Resonant switching	7
3.2	MOSFET switches	8
3.2.1	Introduction to MOSFETS	8
3.2.2	Power MOSFET models	8
3.2.3	Switch procedure and the Miller plateau region	8
3.2.4	Critical Power Losses	8
3.2.5	Effect of source inductance on switching performance	9
4	Design	10
4.1	Introduction	10
4.2	Constraints	10
4.3	Topology	10
4.3.1	Boost converter	11
4.4	Design equations	11
4.4.1	Continuous vs. discontinuous conduction mode	11
4.4.2	Ripple	11
4.4.2.1	Input ripple	11
4.4.2.2	Output ripple	12
5	Implementation	13
5.1	Ideal implementation	13

5.2	Non-Ideal implementation	14
5.2.1	Components	14
5.2.1.1	Power losses/Equivalent series resistance (ESR)	14
5.2.1.2	Diode losses	16
5.2.1.3	MOSFET	16
5.2.2	Sensors	18
5.2.2.1	Voltage sensor	19
5.2.2.2	Input voltage sensor	19
5.2.2.3	Output voltage sensor	19
5.2.2.4	Current sensor	19
5.2.3	Battery protection	19
5.2.4	Peripherals	20
5.2.4.1	MOSFET driver	20
5.3	LTSpice model	21
5.4	System integration	21
6	Validation	23
6.1	Introduction	23
6.1.1	Simulation results	23
6.1.1.1	LTSpice simulation results	23
6.1.1.2	Efficiency calculations and interpolation	25
6.1.1.3	Duty cycle	26
6.1.1.4	Output voltage	26
7	Discussion	29
7.1	Limited data points	29
7.2	Sampling method	29
7.3	Irradiance	29
7.4	Temperature influence on PV modules	29
7.5	Other non-idealities	30
7.6	Output current sensor	30
7.7	Input voltage	30
8	Conclusions and recommendations	31
8.1	Conclusions	31
8.2	Recommendations	31
8.2.1	Diode replacement	31
8.2.2	MOSFET implementation	31
A	Appendix	33
A.1	Terminology	33
A.2	Symbols	33
A.2.1	General	33
A.2.2	PV System	34
A.2.3	MOSFET	34
B	Drone documentation	35
C	Steady state analysis	70
D	Simulation models	72
D.1	PV model	72
D.1.1	Parameters	72
D.2	LT Spice Power Converter Model	73
D.3	Simulink General Simulation Model	73
D.4	Simulink Power Converter Model	74
E	Codes	75
E.1	Data import	75
E.2	Efficiency calculation	76

E.3	Data points to lookup conversion	77
E.4	Interpolation of the lookup matrix.	78
F	Datasheets	81
F.1	MOSFET datasheet.	81

1

Introduction

1.1. Problem analysis

Drones in general are mostly in small form factors and don't have much space available for energy storage. Oil-based solutions such as petrol and diesel engines allow for more energy storage but the biggest drawback of these solutions is that they are polluting and non-sustainable. Therefore, the feasibility of adding PV cells on top of the wings of a Skywalker X8 is checked.

1.2. Overview

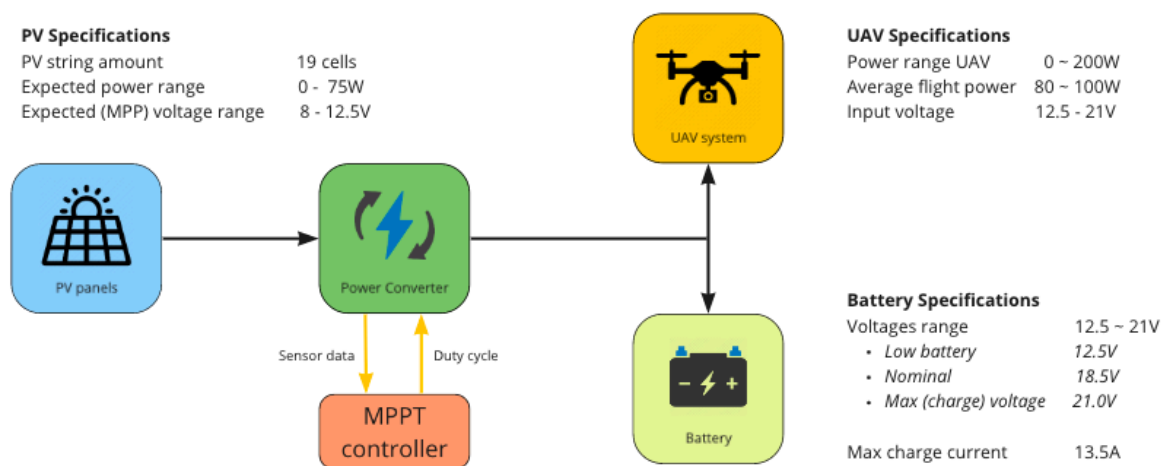


Figure 1.1: Overview of the system surrounding the power converter

In Figure 1.1, the inter-connectivity of the converter within the UAV, and some important numbers that will be considered in more detail later in this thesis are shown. In Appendix B, the complete documentation of the UAV is given.

1.2.1. Irradiance

The maximum power yield of a PV cell is very dependent on the amount of light that is impinging onto it. This amount is represented by the irradiance G [W/m^2]. In Figure 1.2 the expected irradiance in June based on weather data that was provided to aid this research.

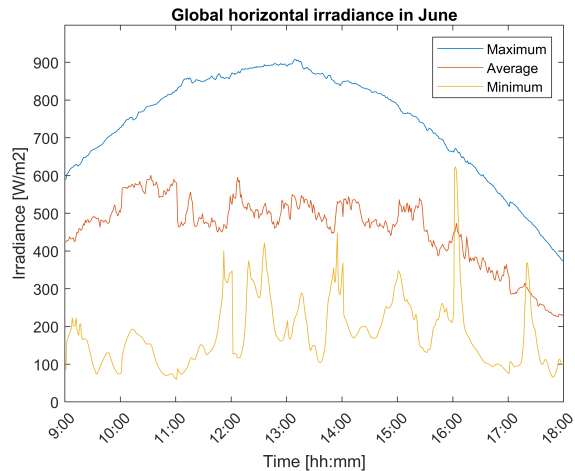


Figure 1.2: Irradiance in June in the Netherlands [9]

1.2.2. Maximum power point tracking

A PV cell's performance is dependent on multiple factors, such as the irradiance and temperature. The power delivery of the cell is determined by a so-called I-V curve. By using this curve the optimal point of operation, or MPP, can be determined. At this point, the output power of the PV cell is highest. The converter that will be designed in this thesis should be able to alter the operating point of the PV system to ensure that the maximum amount of power is delivered to the power system of the UAV.

1.3. Thesis synopsis

In this thesis a certain structure will be followed that coincides with the designing process. First a current state of the art is given. Then, the design, implementation are considered. Subsequently, the results will be validated and limitations to these results will be discussed. Finally, a conclusion and some recommendations are given.

2

Requirements

2.1. Requirements of the total system

The goal of this project is to implement solar panels in a UAV to increase its range, whereas the minimum flight range should cover the area of the TU Delft. This is in order to enable an albedo map to be captured of the area.

2.1.1. Assumptions

We assume the following conditions are met to operate our UAV.

- There is a large enough grass field nearby the location of operation to take off and land a fixed wing UAV.
- The operator flying the UAV is at least certified for ROC and the necessary permits for flying in the area are obtained.

2.1.2. Mandatory requirements

Functional requirements

- The UAV should be able to capture an area the size of the TU Delft campus in a single flight in a maximum time of 60 minutes.
- The UAV should be able to fly 5 times during one day, 2 times before noon, 1 time at noon and 2 times after noon, between flights the battery should be replaced or recharged.
- The UAV's minimum flight altitude is 100m and maximum flight altitude is 120m.
- The UAV should be able to fly with and without solar panels.
- The components of the UAV should be able to be attached into the UAV.
- The weight and size of the components should not prevent the UAV's ability to fly.
- The camera should be able to create images suited for albedo mapping with a GSD (Ground Spatial Distance) of at least 20 cm at a flight height of 120 meters.
- The UAV should be controllable using an autopilot for efficient albedo mapping.
- The UAV should be able to take off and land in a controllable manner.

Non-functional requirements

- The UAV should be less than 4kg to fall within the legal classification of a small UAV.
- The UAV should be able to operate at temperatures ranging from -10 to + 40°C
- Components should be commercial available
- Prices of chosen components should be market conform

Trade off requirements

- The weight of the UAV should be as low as possible to increase flight time.
- The flight path should be optimized to increase area efficiency.
- The effective wing area should be as high as possible to increase power generated by the PV generator.

- The flight speed of the UAV should be as high as possible while keeping the quality of the pictures as high as possible.

2.2. Power converter requirements

The goal of this project is to design a DC/DC power converter that is able to convert power from the PV, which can be used to power the UAV, to increase the flight range. In order to achieve this, the DC/DC power converter...

2.2.1. Functional requirements

- Can handle the maximum input power, voltage and current from the PV system
- Is able to simultaneously supply the UAV and charge the batteries, while the output voltage matches the required voltage for both solutions.
- Controllable to match the Maximum Power Point load of the PV system.
- Has integrated sensors to measure the quantities needed to perform MPPT and switch to battery charging/discharging based on the power drawn by the system and delivered by the PV system.
- Is controlled by a digital controller.

2.2.2. Non-Functional requirements

- Has a minimum efficiency of 85%
- Should have a maximum output voltage ripple of 0.5%

2.2.3. Trade-off requirements

- Has an automatic analog fallback circuit for when the (MPPT) controller fails. Possibly, this can be extended to a MPPT feedback solution.
- Has the conversion efficiency optimized for the average expected PV power.

3

State of the art

3.1. Switching type converters

Switching type converters are the most commonly used converter class, where higher efficiencies are needed. These converters have much higher efficiencies than linear converters with efficiencies up to 98% [18]. It operates the voltage by using a transistor as a switch. Due to the high frequency often used, both the required capacitor and inductor values are a lot lower in general.

3.1.1. PWM converters

PWM, Pulse-Width Modulation, or Chopper, converters are the most commonly used type of switching converters. They allow for voltage regulation and control [7], which is convenient when the input and/or output voltage are variable.

Buck converter

A buck, or step-down, converter is used to convert a DC voltage to a lower DC voltage of the same polarity [8]. It generally has very low power loss, which results in a very high efficiency. As it is only able to step down the voltage, it is unable to perform when the load value is smaller than the optimal MPPT impedance, which results in debatable overall results [18]. An example of a buck converter is shown in Figure 3.1.

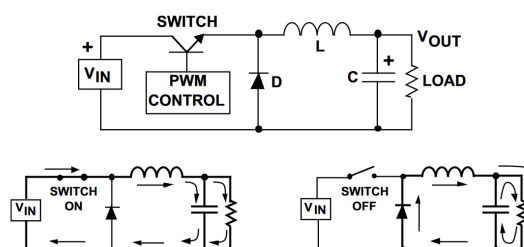


Figure 3.1: Buck converter [8]

Boost converter

A boost, or step-up, converter is used to do the opposite of a buck converter. It is able to convert a lower DC voltage to a higher DC voltage of the same polarity. A boost converter is also very efficient in its operation. Contrary to buck and buck-boost solutions, this kind of converter is only able to step up the voltage, which results in its inability to perform when the impedance of the PV system is higher than the impedance of the converter [12][18]. An example of a boost converter is shown in Figure 3.2.

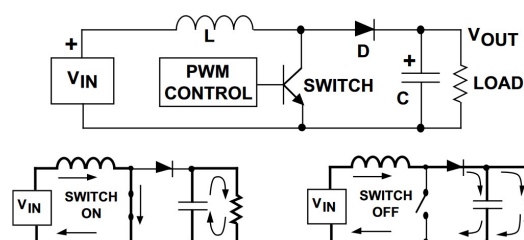


Figure 3.2: Boost converter [8]

(inverting) Buck-Boost converter

A buck-boost, or step-up/step-down, converter is a combination of a buck and a boost converter. It can both convert a higher DC voltage to a lower DC voltage and the other way around. Contrary to the buck

and boost converter, it has a non-operating spectrum, which means it is able to match the apparent impedance for all values of the optimal impedance for the MPPT. For an inverting type buck-boost, another major difference is that it inverts the polarity of the voltage. An example of such a circuit can be seen in Figure 3.3a. The non-inverting, as shown in Figure 3.3b, has a higher efficiency than its inverting counterpart and is therefore most likely a better solution for efficient power transfer [18].

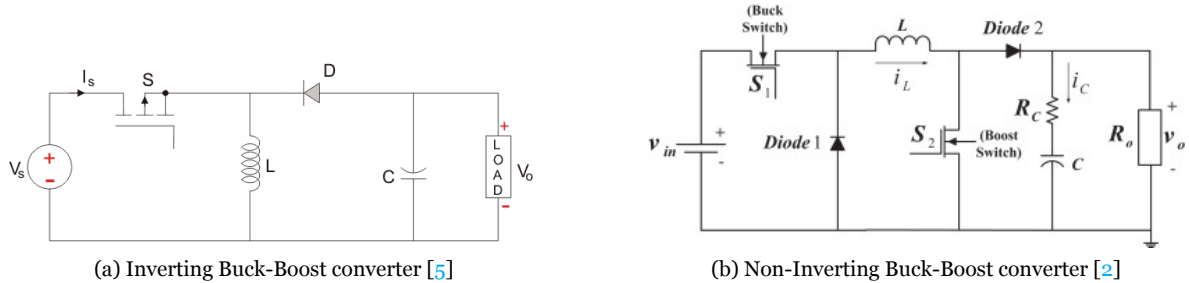


Figure 3.3: Two basic buck-boost converter topologies

Flyback converter is a variation on the standard buck-boost converter. A coupled inductor is placed between the input and the output, additionally, which makes it an isolated converter. It is also able to both step-up and step-down. Contrary to the standard buck-boost topology, it is non-inverting, which means the output voltage has the same polarity as the input voltage.

A flyback converter is very efficient but there are a few complications. First of all, a coupled inductor can be quite bulky when the switching frequency is chosen to be lower. Secondly, also due to the coupled inductor, active clamps, or snubbers, need to be used to counter the magnetic flux losses. If no form of switching loss reduction is used, the efficiency of the system will go down significantly.

Four-Switch buck-boost converter is another variance on the standard buck-boost converter, as is shown in Figure 3.5. As the name implies, it is driven by four switches instead of two. The main advantage of this converter is that it can be controlled by two separate duty cycles, which means more freedom [14]. Besides that, the diodes have been replaced. For low-power, low-frequency systems, this results in a higher efficiency. A drawback is that it adds complexity to the system.

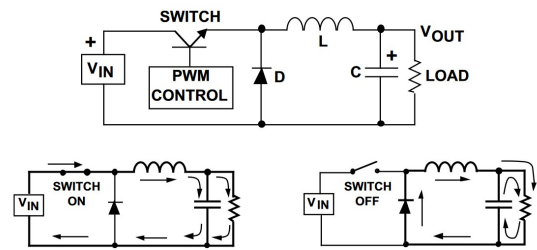


Figure 3.4: Flyback (Buck-Boost) converter [8]

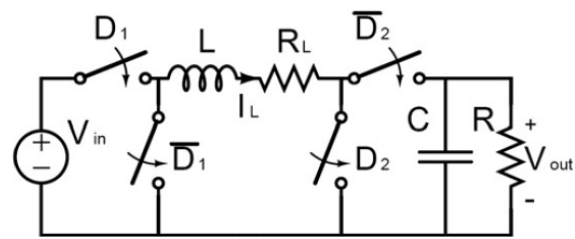


Figure 3.5: Four-Switch buck-boost converter [14]

Ćuk converters are an inverting buck-boost type converter. The main advantages of this type of converter is that the input is almost ripple-free, it has a continuous input current and the switch terminal is connected to the ground, which makes the gate drive design for switching less complex. A major drawback, however, is that the coupling capacitor needs to be large and expensive [18]. Additionally, this capacitor is put under much stress, which leads to less robustness for the overall circuit. An example of a Ćuk converter can be seen in Figure 3.6.

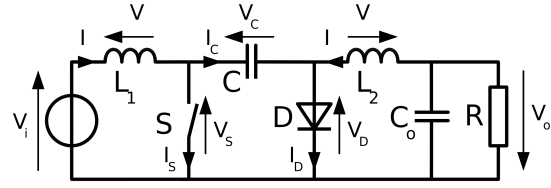


Figure 3.6: Ćuk converter [19]

SEPIC or a Single-Ended Primary Inductor Converter, is another type of non-inverting buck-boost type converters. It consists of a boost and inverted buck-boost converter added together. Like the Ćuk converter, it has the switch terminal connected to the ground. Furthermore, unlike the Ćuk converter it does not mostly operate over the coupling capacitor but over both a capacitor and inductor, which results in less stress on the individual components [18].

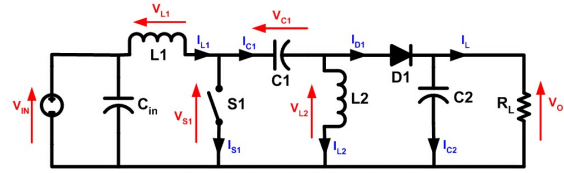


Figure 3.7: SEPIC converter [19]

Switched coupled capacitors

A switched coupled capacitors, or charge pump, converter is a step-up or step-down type converter that has no inductors within its circuit. It instead delivers power by charging and discharging capacitors. Its efficiency and complexity are in between the inductive switch type and linear converters. However, charge pump gains are fixed [11]. Therefore, this type of converter will not be considered as a possible solution for this project.

3.1.2. Switching losses

Switching losses occur due to the fall and rise time of the MOSFET. In Equation 3.1[16], the switching losses are shown.

$$P_{loss_{switch}} = \frac{(t_r + t_f)}{2} \cdot V_{PV} \cdot I_{out} \cdot f_s \quad (3.1)$$

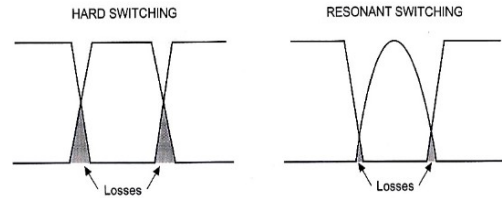


Figure 3.8: Hard switching and resonance switching visualised [15]

Hard switching

By default, voltage converters that use switches have switching losses caused by hard switching. Hard switching is a switching method that uses the device its own switching ability [1]. An example of hard switching can be seen in the left of Figure 3.8. In this Figure, the effect of non-zero current or voltage switching is shown.

Resonant switching

Resonant switching is a more efficient method of switching. This method allows for (near) zero voltage switching and/or zero current switching, which leads to decreased losses. This is especially significant for very high switching frequencies, such as frequencies above 500kHz [15]. Within the given time frame, implementing resonant switching will not be considered in this thesis, but it could be interesting for future research.

3.2. MOSFET switches

3.2.1. Introduction to MOSFETS

MOSFET's have two major advantages over bipolar junction transistors, the first advantage being the ease of use of MOSFET's for high frequency switching applications. Besides that, once the MOSFET transistor is turned on, its drive current is near zero. This results in a higher efficiency for converters[4].

3.2.2. Power MOSFET models

Figure 3.9 shows MOSFET models for three different problem areas. The first model is based on the actual structure of the MOSFET device and can be used mainly for DC analysis. The second model can be used very effectively to model the dc/dt induced breakdown characteristics of a MOSFET. The last model shows the most important parasitic components for when the MOSFET is switching. [4]

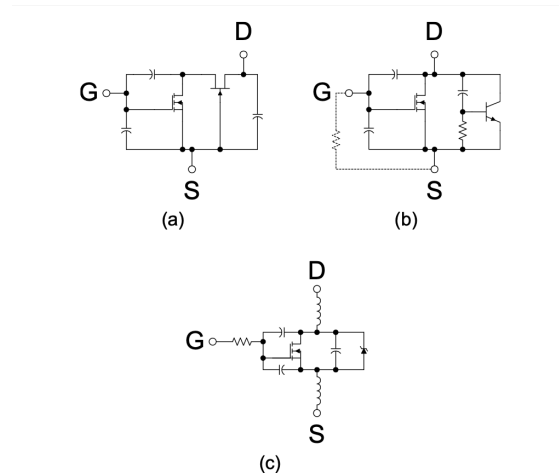


Figure 3.9: Power MOSFET models[4]

3.2.3. Switch procedure and the Miller plateau region

The switch procedure of a MOSFET can be divided into four intervals. When the MOSFET is turned on, the input capacitance of the device is charged from 0V to V_{th} . These capacities are connected to the drain and source, shown in the third model of figure 3.9. After the threshold voltage is reached, the MOSFET becomes in a linear operating mode. During this period, the charging of the input capacitance continues and the drain current increases, shown in equation 3.2, proportional to the gate voltage. When the gate voltage reaches the Miller plateau level, the drain current becomes stable in the third period starts. The miller plateau level is described in equation 3.3 or could be found in the datasheet. In this period, the gate current starts discharging the C_{GD} capacitor of the MOSFET what induces a fast drain-source voltage drop and so decreases the on-resistance rapidly. A remarkable point, the gain voltage stays stable at the Miller Plateau level during this period. That is why it is called the Miller Plateau region. In the last step the gate capacitors will charge to the final driver voltage and the on-resistance will improve to it's final value. The same procedure in the other way around follows when the MOSFET is turned off[4].

$$I_D = (V_{GS} - V_{th}) * g_{fs} \quad (3.2) \quad V_{GS,Miller} = V_{th} + \frac{I_D}{g_{fs}} \quad (3.3)$$

The trans conductance, g_{fs} showed in equation 3.4, is the small signal relationship between drain current and gate-to-source voltage as shown in equation. 3.4.

$$g_{fs} = \frac{dI_D}{dV_{GS}} \quad (3.4)$$

3.2.4. Critical Power Losses

Gate drive loss [4] Gate drive loss arise by turning on or off the MOSFET, which results in charging or discharging the parasitic capacitors inside the MOSFET. The power loss is described by Equation 3.5, where V_{DRV} is the amplitude of the gate drive waveform, f_{DRV} the gate-drive frequency, and Q_G is the gate charge.

$$P_{Gate} = V_{DRV} * Q_G * f_{DRV} \quad (3.5)$$

Driver power dissipation

$$P_{DRV,ON} = \frac{1}{2} * \frac{R_{HI} * V_{DRV} * Q_G * f_{DRV}}{R_{HI} + R_{Gate} + R_{G,I}} \quad (3.6)$$

$$P_{DRV,OFF} = \frac{1}{2} * \frac{R_{LO} * V_{DRV} * Q_G * f_{DRV}}{R_{LO} + R_{Gate} + R_{G,I}} \quad (3.7)$$

$$P_{DRV} = P_{DRV,ON} + P_{DRV,OFF} \quad (3.8)$$

Total switching loss approximation[4]

Calculating the exact switching losses is almost impossible. The following described linear approximation seems to be a reasonable enough compromise to estimate switching losses in the MOSFET.

$$P_{SW} = \frac{V_{DS(off)} * I_L}{2} * \frac{t2 + t3}{T} \quad (3.9)$$

where

$$t2 = C_{ISS} * \frac{V_{GS,Miller} - V_{TH}}{I_{G2}}, t3 = C_{RSS} * \frac{V_{DS,off}}{I_{G3}}, \quad (3.10)$$

$$I_{G2} = \frac{V_{DRV} - 0.5 * (V_{GS,Miller} + V_{TH})}{R_{HI} + R_{GATE} + R_{G,I}}, I_{G3} = \frac{V_{DRV} - V_{GS,Miller}}{R_{HI} + R_{GATE} + R_{G,I}} \quad (3.11)$$

3.2.5. Effect of source inductance on switching performance

For the switching performance is the source inductance, which stems from the wires, is the most dominant of all parasitic components. When switching and the gate current is changing very rapidly, the current must flow through the source inductor and will be slowed down. With as result, a longer switching time. After that, the source inductor and capacitance C_{ISS} of the MOSFET (described in the datasheet) form a resonant circuit, as shown in figure 3.10, what induces the oscillatory spikes observed in most gate drive circuits. This oscillation can be damped by the series resistive components of the loop, which include the driver output impedance, the external gate resistor, and the internal gate mesh resistor. For the optimum performance, the gate resistance can be calculated by equation 3.12 where C_{ISS} and L_S are given by the MOSFET datasheet.

The second effect of the source inductance is a negative feedback whenever the drain current of the device is changing rapidly in the second period in the switching process when the MOSFET is turned on (or third when turned off). A significant voltage has to be applied across the source inductance to increase the drain current quickly. Consequently, the voltage will drop across the drive impedance with as result a lower change in drain current. The balance between both is established through the negative feedback by the source inductor. [4]

$$R_{gate,opt} = 2 * \sqrt{\frac{L_S}{C_{ISS}} - (R_{drv} + R_{g,i})} \quad (3.12)$$

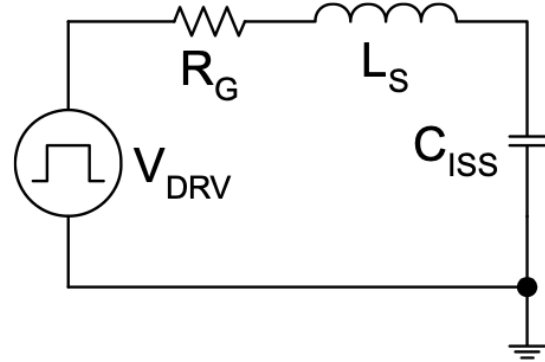


Figure 3.10: Gate-Drive Resonant Circuit Components, fig 7 in [4]

4

Design

4.1. Introduction

This chapter explains the design choices made in the process of creating the power converter. First, the constraints are elaborated on, then the decided topology is explained, and finally, the corresponding design equations are worked out.

4.2. Constraints

Some design constraints regarding the converter need to be taken into account. First of all, because the converter will be eventually implemented inside a UAV with PV cells, there are two options regarding the power supply of this system. The first option is that the UAV flies on the PV power alone. However, it is already shown in Appendix B that it already consumes more power, while cruising, than the PV system is able to supply. The second option is the attachment of a battery to the system that is able to provide the system with the necessary power when needed. It is clear that the second option is the only possible option for this particular case. For this reason, a battery is attached to the converter in parallel to the load, as is shown in figure 4.1. As previously stated in Appendix B, a brush-less DC motor is able to operate more efficiently at higher voltages. Due to this, a battery with a nominal voltage of $18.5V$ was chosen, which equals five cells connected in series to match the maximum voltage the motor allows. When discharging, the voltage can drop down with $12.5V$ as a minimum, and the maximum charging voltage of the battery equals $21.0V$. Therefore, an output range of $12.5V$ to $21.0V$ needs to be accounted for.

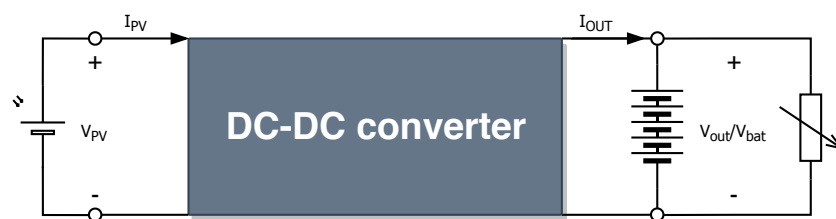


Figure 4.1: Simplified blackbox design of the DC-DC converter, including design constraints

4.3. Topology

In the requirements, it is specified that the converter is able to operate at the voltages that are supplied to it by the PV system attached to the UAV. More specifically, for the design of the converter, it is assumed from the PV specifications that the input voltage is ranging from $8 - 12.5V$. The chosen topology must be able to convert this voltage to the voltage of the battery. Since the battery voltage is always higher than the assumed output voltage of the PV system, a boost converter topology was chosen.

4.3.1. Boost converter

A boost, or step-up, converter is able to convert a lower DC voltage to a higher DC voltage of the same polarity. Next to the relatively simple implementation of a boost converter, it is also very efficient in its operation.

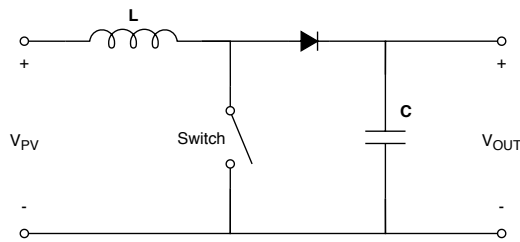


Figure 4.2: Topology of an ideal boost converter

In Figure 4.2, a representation of an ideal boost converter is shown. When the switch is closed, a current will start to flow through the inductor, charging it. When the switch is opened, a current will start to flow from the charged inductor towards the right-hand part of the circuit, inducing a voltage in the capacitor, due to the change in current. When the switch is closed once more, the capacitor will discharge and keep the output voltage more or less constant.

4.4. Design equations

Now that the topology has been selected, an analysis of the circuit needs to be done in order to assess the design equations for the converter. Furthermore, a steady-state analysis has been done later on to assess the relation between the input and output voltage and the non-idealities of the circuit, of which the complete calculation can be found in Appendix C.

4.4.1. Continuous vs. discontinuous conduction mode

Before assessing the formulas for the components, an important choice has to be made, whether the converter will operate in continuous conduction mode (CCM) or discontinuous conduction mode (DCM). In continuous mode, the energy storage of the inductor never reaches zero. On the other side, this does happen when in DCM, which implies that $L_{DCM} < L_{CCM}$. Taking a look at Ohm's law provides us with the fact that a lower inductance will result in a higher peak-to-peak current, which is the effect of higher ripple current. Therefore, CCM is chosen as the operating mode of the converter, resulting in a duty cycle for the switch that is given by Equation 4.1. Besides that, losses may occur since not all supplied power by the PV system can be stored. Both of the issues described will be covered in the next sections.

$$D = 1 - \frac{V_{PV}}{V_{out}} \quad (4.1)$$

4.4.2. Ripple

Ripple currents and voltages are deviations on top of the average values. Most of the time, ripple values are expressed in both a percentage and in amperes or volt, respectively. For this converter, the main requirements have been set to limit ripple at the input and the voltage ripple at the output.

Input ripple

As this converter will be connected to a PV system, the MPP will be controlled by it as well. Depending on which method is used for the MPPT, the input current ripple may play a significant role in the accuracy of the chosen method. The method that was chosen by for this vehicle's cells, perturb and observe, or simply P&O, is also susceptible to this variation. Hence, the input ripple needs to be limited in order to minimize the deviation of the MPPT.

$$I_{pp} = r_l \cdot I_{max} \quad (4.2)$$

$$L = \frac{|V_{PV} - V_{out}| \cdot T_{on}}{I_{pp}}, \text{ where } T_{on} = D \cdot T_{sw} \quad (4.3)$$

The formula for a ripple current is given by Equation 4.2. In this case, the peak-to-peak current ripple is defined as a percentage of the maximum current provided by the PV system. Using Ohm's law and applying a switching frequency yields Equation 4.3 for the value of the inductor.

Another thing that is not caused by the input ripple but can influence it is the total energy storage of the left-hand side of the circuit. The maximum energy storage needed is given by Equation 4.4, at the maximum PV power and highest on time for the switch. The maximum energy that can be stored in an inductor can now be calculated by means of Equation 4.5. Dependent on the energy storage capability of the inductor, a more substantial inductance value or an additional input capacitance can be added for $E_{L,MAX} < E_{store,MAX}$. The addition of an input capacitance leads to LC filter characteristics and is able to smooth the input voltage, on top of that. Therefore if the need for this arises, a capacitor will be implemented besides the already present inductance. The need for such a capacitor is described under Chapter 5.

$$E_{store,MAX} = P_{PV,MAX} \cdot T_{sw} \quad (4.4)$$

$$E_{L,MAX} = \frac{1}{2} \cdot L \cdot I_{MPP,MAX}^2 \quad (4.5)$$

$$E_{C,MAX} = \frac{1}{2} \cdot C \cdot V_{MPP,MAX}^2 \quad (4.6)$$

Output ripple

The output ripple is another ripple that is taken into consideration for this converter. As the converter is directly connected to the battery, it is best to ensure that the ripple is minimal, and it is less likely to heat up due to ripple in the operating voltage, subsequently. Defining the ripple as by Equation 4.7 and using the same principle as for deriving Equation 4.3 by the voltage/current relationship of capacitors, Equation 4.8 is obtained.

$$V_{pp} = r_V \cdot V_{out} \quad (4.7)$$

$$C_{out} = \frac{T_{on}}{(V_{pp}/I_{pp})} \quad (4.8)$$

For the purpose of this converter, the output capacitor will be operating at the same voltage as battery voltage, as it is directly connected. Because the output voltage, therefore, is relatively fixed, during the state, when the switch is closed, the capacitor will stay mostly charged.

5

Implementation

In this chapter, the component selection will be discussed. First, an ideal implementation is covered, after which non-idealities are taken into account. Lastly, the simulation model and the system integration of the model are described.

5.1. Ideal implementation

Before determining the component values of the boost circuit, it has to be assessed what parameters are the most important to take into account. A high efficiency can be obtained by reducing the switching frequency and thus switching losses, as can be derived from Equation 5.1.

$$P_{loss_{switch}} = \frac{(t_r + t_f)}{2} \cdot V_{pV} \cdot I_{out} \cdot f_s \quad (5.1)$$

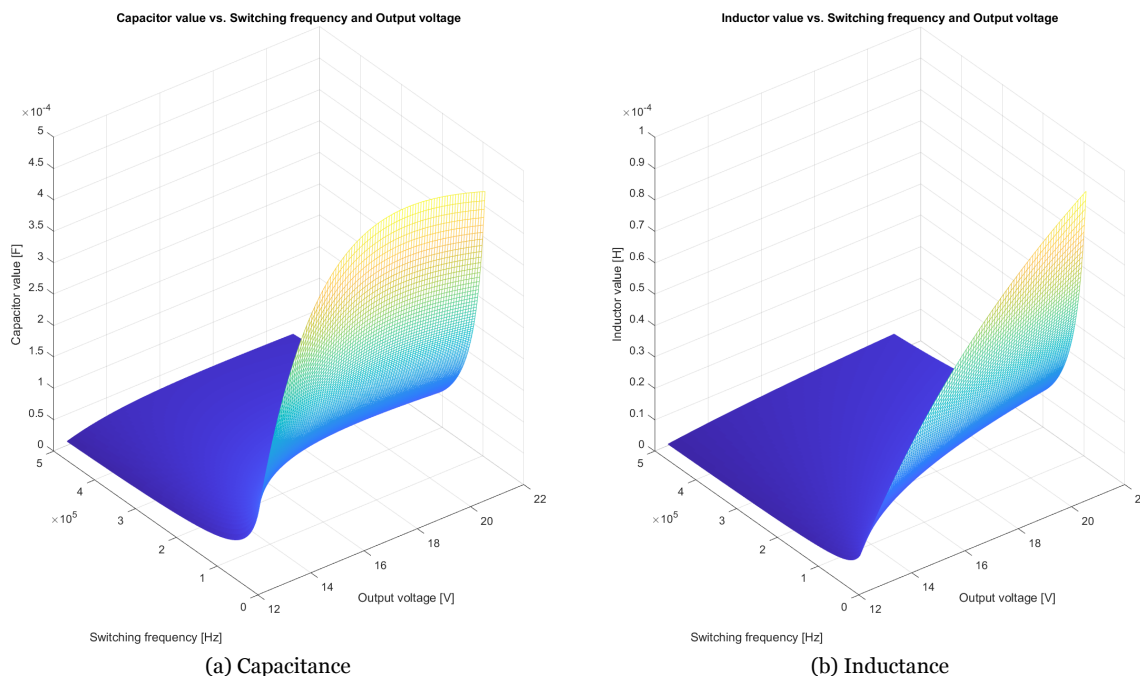


Figure 5.1: Capacitance and inductance values versus the switching frequency and output voltage of the converter

However, decreasing the switching frequency will require larger component sizing, which may lead to increased volume and weight and subsequently power loss due to a higher required motor power.

Therefore, a trade-off between the component value and switching frequency needs to be made. Furthermore, the output voltage, which is equal to the battery voltage, needs to be taken into account as well, in order to ensure that the set requirements are met. For the calculations of these components, Equations 4.2, 4.3, 4.7 and 4.8 are used. In Figure 5.1, the results are shown. From this figure, it can be seen that both the capacitance and inductance increase exponentially for a switching frequency lower than 150kHz . At the same time, the decrease in component values for frequencies lower than 150kHz slows down.

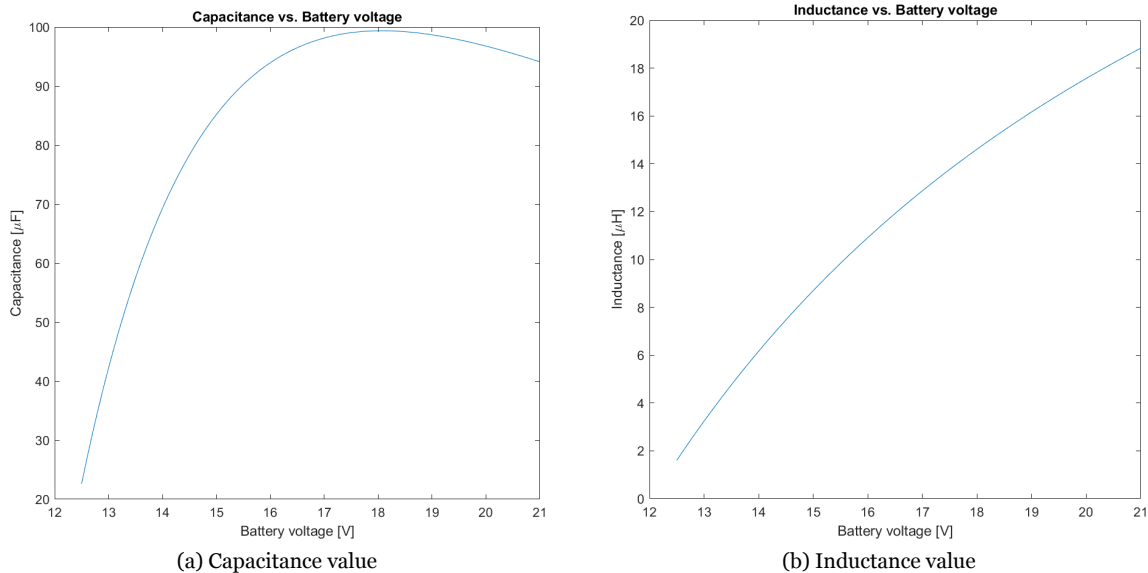


Figure 5.2: Capacitance and inductance value versus the battery voltage at 150kHz

Besides this, the effect of the battery voltage on the required component values for a frequency of 150kHz can be observed in Figure 5.2. The maximum value is found at a battery voltage of 18V for the capacitance, and 21V is found for the inductance. In Figure 5.3, the influence of the frequency on the component value can be seen even more clearly. From Figure 5.3, a minimum required value of $99.37\mu\text{F}$ is determined. The same principle applies to the minimum inductance value of $18.83\mu\text{H}$ that is determined from Figure 5.3b. In reality, the closest commercially available component values are $100\mu\text{F}$ and $22\mu\text{H}$, which are the values that will, therefore, be used inside the simulation models. It is found using Equations 4.4, 4.5 and 4.6 that for these values, in order to store the maximum power that can appear in the left-hand circuit, as is described in Section 4.4.2, an additional input capacitor is required with a minimum value of $1.14\mu\text{F}$. Once more, a similarly valued, commercially available, counterpart will be rated at a value of $1.5\mu\text{F}$, which is also the value that will be used for simulation purposes.

5.2. Non-Ideal implementation

In reality, the circuit that is shown in Figure 4.2 is missing some parameters that are accountable for losses in the circuit. These losses need to be taken into account for the simulation in order to have a realistic model. In Figure 5.4, a non-ideal boost converter topology is shown that has accounted for the losses that will be taken into account.

5.2.1. Components

Power losses/Equivalent series resistance (ESR)

Non-ideal components like capacitors and inductors are in fact not without parasitic effects next to its ideal implementation, which can induce losses but also have other properties that can be taken into consideration. After assessing and prioritising these effects, a component can be selected to minimise the power losses.

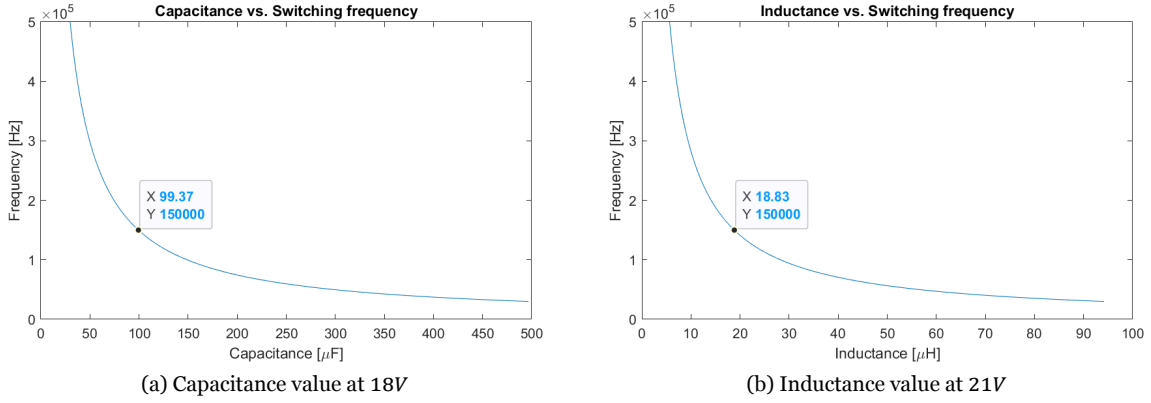


Figure 5.3: Capacitance and inductance value versus the switching frequency

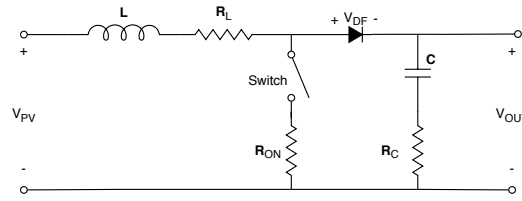


Figure 5.4: Representation of a non-ideal boost converter

Inductor The electrical losses caused by the inductor can be separated into two categories: Core losses and conductor losses. The core losses majorly depend on the type of core and the switching frequency. Because the core losses (mW) are much lower [6] in comparison to the conducting losses (W), the core losses are not into account.

The conductor losses, which is caused by the ESR, which subsequently consists of the DC and AC resistance, come from the wire that the inductor consists of [13]. This results in a new voltage relationship, that can be seen in Equation 5.2 and Equation 5.3. The resistance of this wire is dependent on the length of the wire, but also the diameter or thickness of the wire. The longer the wire, the higher the resistance and weight of the inductor. The thicker the wire, the lower the resistance will be, but it will also increase the weight of the inductor.

Next to the electrical losses, there is also a power loss caused by the inductor's weight. Due to the increase in weight, the UAV will consume more power in order to fly. According to the aerodynamic model, an increase of 1kg leads to an increase in power consumption of 28W. Therefore, a trade-off between the ESR and the weight of the inductor has to be made. Ohm's law for the maximum input current and ESR is compared to the power needed per weight increase in Table 5.1. The possible choices for the inductors are all rated for peak currents of 12 ampere, which has been determined by taking into account the maximum input current, input current ripple, and a safety factor of 1.5. Finally, it is the Pulse Electronics (PA4343.223NLT) inductor that is chosen to implement in this converter due to it showing the least power losses.

Table 5.1: Comparison in the power losses of several inductor types

Manufacturer	Type	L (μH)	I_{max} (A)	R ($m\Omega$)	Mass (g)	P_{lossR} (W)	$P_{lossmass}$ (W)	P_{tot} (W)
Coilcraft	VER2923	22	9	2,3	37	0,014375	1,0471	1,061475
Würth Elektronik	74435572200	22	11	14,6	13	0,09125	0,3679	0,45915
Pulse Electronics	PA4343.223NLT	22	12	37	0,123	0,23125	0,0034809	0,2347309
Coilcraft	MSS1583-223MEB	22	10,4	36	4,4	0,225	0,12452	0,34952
Bourns	SRP1265A-220M	22	12	32	6,1	0,2	0,17263	0,37263
Vishay	IHLP6767GZ	22	9,5	20	11,8	0,125	0,33394	0,45894

$$V_L = V_{R_L} + V_{out} - V_{PV}, \text{ when MOSFET turned off} \quad (5.2)$$

$$V_L = V_{PV} - V_{R_L}, \text{ when MOSFET turned on} \quad (5.3)$$

Capacitor For the capacitor, there is also an ESR present. In this case, however, the ESR is not directly correlated to the weight of the capacitor. The capacitor's ESR is highly dependent on the type of capacitor that is used. Electrolytic capacitors are low cost but have a high ESR, which induces losses at the output. Ceramic capacitors have a very low ESR and have a good frequency response but have less effective capacitance stability at higher values. Due to the extremely low ESR, ceramic type capacitors are very suitable for an input capacitance [17]. However, at some frequencies, a dip in ESR may occur [3]. Besides that, to ensure good smoothing of the voltage, it is essential that the ESR is not too low [13]. This is why a tantalum type capacitor was chosen for the output instead. Although it has a little higher ESR, the effective capacitance is more stable, and the ESR is never too low. The chosen type for the output capacitor is the KEMET T521X107M025ATE060, which has a capacitance of $100\mu F$, a series resistance of $60m\Omega$ and a rated voltage of $25V$, and a Murata GCM21BR71C155MA37, which has a capacitance of $1.5\mu F$, a series resistance of $< 1m\Omega$ and rated voltage of $16V$.

Diode losses

Forward voltage drop The forward voltage is present in all non-ideal diodes. The internal resistance of the diode causes a voltage drop at the output. One of the unusual properties of a diode is that the voltage drop remains relatively constant. This means for low-voltage, high-current applications that the power loss is quite high. The power loss in a diode can be calculated by means of Equation 5.4. Schottky diodes have a lower voltage drop than PN-junction diodes and are therefore more prevalent in use for power converters.

$$P_{loss\ diode} = V_{DF} \cdot I_D \quad (5.4)$$

Reverse bias leakage current The reverse bias leakage current is also something that causes losses when operating a diode. In an ideal situation, the diode prevents current from the output to the input side of circuit. In reality, however, a reverse bias current flows backward through the block of the diode. The higher the bias voltage across the diode, the higher the reverse bias current. For simplicity of the steady-state analysis, the reverse bias current is not taken into account, as the losses originating from this are negligible since $I_{rev.bias} \ll I_{out}$.

Chosen diode As previously stated, Schottky diodes have a lower forward voltage than PN-junction diodes. For this reason, this type will also be used in the implementation of the converter. For the selection of the specific diode, the forward current rating and breakdown voltage have been taken into account. The maximum voltage potential between the input and output terminal occurs at a minimum input voltage, of $0V$, and a maximum output voltage, of $21V$, which is therefore also the minimum required breakdown voltage. The Rohm RBR30NS30A suffices for both these parameters, with a current rating of $30A$ and a breakdown voltage of $30V$.

MOSFET

The MOSFET is used to switch the inductor current between the ground and the output. The maximum drain-source current (I_{DS}) is equal to the max inductor current, which is theoretically 6.25 ampere for the maximum expected power output of the solar panels. However, this current can have an increase when the PV cell temperature or irradiance changes. That's why a safety margin of factor 1.5 is included over the max drain current. After this safety margin, the converter is resistant for peak currents from PV with outside temperatures till 40 degrees and irradiances up to $1500W/m^2$, assuming linear scaling of the power. The minimal drain-source voltage (V_{DS}) of the MOSFET is determined by the maximum output voltage with the forward diode voltage together. To be able to handle voltage spikes over the MOSFET induced by parasitic switching effects, this voltage is multiplied by a factor 2 , which results in a minimal V_{DS} around 40 volts.

The main losses in a MOSFET switch (equation 5.5) are gate switching losses (equation 5.6) and conduction losses (equation 5.7). While the switching loss in the MOSFET driver is also dependent on the MOSFET, an approximation of the driver loss has been made to get the best overview before selecting the MOSFET.

The switching losses are dependent on the values of the switching frequency, driver and gate resistances, and the gate charge Q_G . To be more specific, the Q_G is dependent on the gate capacity, which is dependent on the MOSFET design, and the driver voltage.

In order to reduce the conduction losses, the on-resistance R_{DS} should be minimized. R_{DS} is dependent on the MOSFET design and the gate, or driver, voltage. When minimizing the total power loss, the gate capacity and on-resistance must be low as possible. Unfortunately, as is determined by the design of a MOSFET, a lower Q_G results in a higher R_{DS} and vice versa. Finding the optimum for all these parameters can be a time-consuming process. Due to the lack of available time, a more straightforward method was implemented, which first assesses which parameters are more critical.

When equalizing the losses in the gate, driver, and on-resistance by doing an approximation for the gate resistances, a ratio could be found between R_{DS} and Q_G (equation 5.11) for different input powers. This ratio indicates when the switching losses are equal to the conduction losses. Figure 5.5 shows the ratio as a function of the input power. For this plot are the gate with driver resistances approximated at 10Ω , the input voltage is fixed at $12V$ and the output voltages are fixed at $18.5V$.

The figure illustrates the relevance of gate charge and on-resistance for different input power scenarios. When the input power is decreasing (visible for input powers lower than $10W$), the gate charge would be more critical. So a lower Q_G (or higher R) is needed to find an equilibrium between the losses. On the other hand, when the input power increases higher than $10W$, the losses in the drain-source resistance is dominating over the switching losses and will be much more critical.

The expected average input power from the solar cells is $32W$, so the drain-source resistance will be the most critical parameter to select the MOSFET.

$$P_{MOSFET} = P_{Gate} + P_{DS}(+P_{DRV}) \quad (5.5)$$

$$P_{Gate} = V_{DRV} * Q_G * f_{DRV} \quad (5.6)$$

$$P_{DS} = I_{DS}^2 * R_{DS} \quad (5.7)$$

$$P_{DRV,ON} = \frac{1}{2} * \frac{R_{HI} * V_{DRV} * Q_G * f_{DRV}}{R_{HI} + R_{Gate} + R_{G,I}} \quad (5.8)$$

$$P_{DRV,OFF} = \frac{1}{2} * \frac{R_{LO} * V_{DRV} * Q_G * f_{DRV}}{R_{LO} + R_{Gate} + R_{G,I}} \quad (5.9)$$

$$P_{DRV} = P_{DRV,ON} + P_{DRV,OFF} \quad (5.10)$$

$$\frac{R}{Q} = \frac{V_{DRV} * f_{DRV} + \frac{(0.5 * R_{HI} * V_{DRV} * f_{DRV})}{(R_{HI} + R_{Gate} + R_{G,I})} + \frac{0.5 * R_{LO} * V_{DRV} * f_{DRV}}{(R_{LO} + R_{Gate} + R_{G,I})}}{(I_{DS}^2 * DC)} \quad (5.11)$$

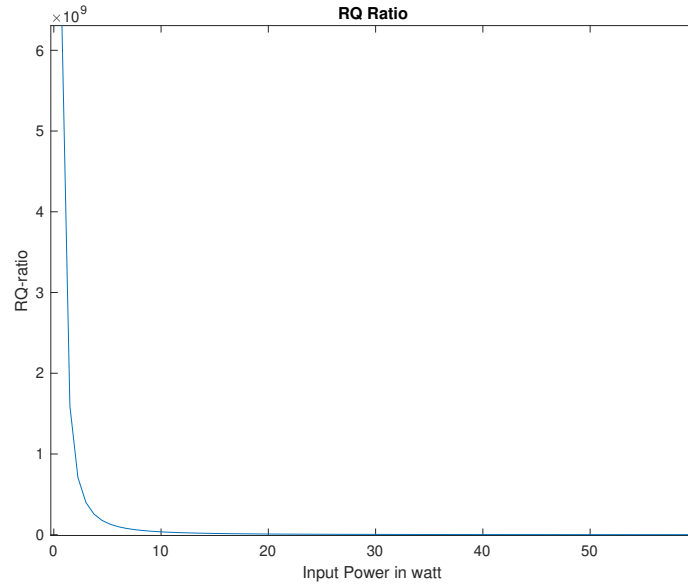


Figure 5.5: RQ ratio for different input powers

To conclude, the following method is used to select the MOSFET: ---

1. Filter MOSFETs with a rated V_{DS} of minimal 40V
2. Order MOSFETs with minimal R_{DS}
3. Select MOSFET with minimal R_{DS} and lowest Q

In table 5.2 is the result of the specified selection procedure for three different manufacturers based on the parameters from the respective datasheets. The selected MOSFET for the boost converter is the Nexperia BUK9JoR9-40H; for the datasheet see Appendix F.1. The expected power losses for the selected MOSFET are in a range of 40mW to 75mW, as shown in figure 5.6.

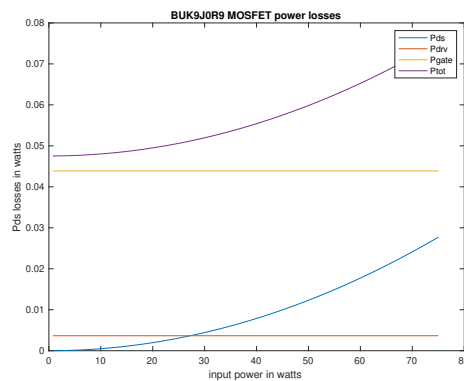


Figure 5.6: Nexperia BUK9JoR9-40H expected power losses

5.2.2. Sensors

For MPPT of the PV system, it's required to know the input voltage (PV), input current (PV) of the converter. Also, the output voltage (battery) is required for the protection of the battery. Furthermore, a current sensor is implemented at the output, in order to have the possibility for a MPPT fallback circuit that is regulated by output power, rather than input power. In this section we discuss how and which sensors are chosen to implement.

Table 5.2: Comparison in R_{DS} and Q_G for different MOSFETs from three different MOSFET manufacturers

Manufacturer	Type	Max Vds	Rds @Vds = 4.5	Qg @Vds = 4.5
Vishay	SiDR402DP	40	0.00116	53
Texas Instruments	CSD18510Q5B	40	0.00160	118
Nexperia	BUK9JoR9-40H	40	0.00097	50
Nexperia	PSMNR90-40YLH	40	0.00097	54

Voltage sensor

The sensor will be used by a microcontroller that has a 5 volts, usual 10-bit ADC, input. For this application, to options to consider are the voltage divider or an optocoupler. Because of simplicity, the voltage divider is a more suitable option for this power converter. The resistors will be selected from the RN73 resistor series of KOA Speer Electronics. This resistor series has high precision, high reliability and is very stable for elevated temperatures, which makes it perfectly suitable for measurement applications for a good price.

The disadvantage of the voltage divider is the constant current through the resistors, so to avoid this issue, the sensor resistance must be high. The sensor will also influence the voltage when the sensor resistance is too low. To avoid this issue, the resistor values for the sensor are chosen factor 1000 higher than the resistance of the output load. When the sensor is implemented in the real system, it is essential to use low resistance cables to prevent voltage drop over the cables.

Input voltage sensor

The input voltage of the converter is in a range from 5V to 12.5V. A micro-controller will be measuring the voltage with an ADC with a maximum input voltage of 5 volts.

With a margin of 10% over the converter input voltage, the ratio R_1/R_2 must be around 13.2/5. The resistors chosen for the voltage sensor are $R_1 = 4.9k\Omega$ and $R_2 = 13.2k\Omega$. Both with a very low tolerance of 0.1%.

This results in a sensitivity of $269mV/V$ and a maximum deviation of $0.4mV$.

Output voltage sensor

The output voltage of the converter is in a range from 12.5V to 21V. The voltage will be measured by a micro-controller with an ADC with a maximum input voltage of 5 volts.

With a margin of 10% over the converter output voltage, the ratio R_1/R_2 must be around 23.1/5. The resistors chosen for the voltage sensor are $R_1 = 4.9k\Omega$ and $R_2 = 24k\Omega$. Both with a very low tolerance of 0.1%.

This results in a sensitivity of $170mV/V$ and a maximum deviation of $0.3mV$.

Current sensor

Current sensing requires a low resistance to be as accurate as possible and avoid power losses. Resistive solutions to current sensing result in a higher power loss than magnetic solutions. For this reason, a (magnetic) hall sensor was chosen as the current sensing method. The current range for the input and output of the converter is from 0 to 7A. The current sensor applied in the power converter is the Allegro ACS724LLCTR-10AU-T. This is a digital sensor with a linear output for a current range till 10A and an accuracy of $400mV/A$. The sensor has a very low conductor resistance of $1.2m\Omega$ and has an input voltage of 5V and an input current around 10mA. The UBEC will supply this sensor.

5.2.3. Battery protection

Although even while the UAV is cruising, the energy consumption is higher than the maximum energy yield, the battery still needs to be protected in case the PV is still delivering power when the UAV is on stand-by. As such, in order to prevent overcharging of the battery, a method needs to be devised to cut off the PV power. For this, a possibility would be to implement a controllable switch such as a MOSFET. However, it is also possible to either let the PV cells operate in short- or open-circuit mode. This results in the PV operating at a very low efficiency and thus protects the battery from overcharging without

the need of an extra component. In short circuit mode, I_{sc} will run through the ESR of the inductor and R_{on} of the MOSFET. This will result in a small induced voltage from this, which will saturate the inductor and continuously put the MOSFET under load. The open-circuit operation mode is, therefore, better suited for this. As the potential in the right-hand side of the circuit is 21V when the battery is fully charged, it is much higher than the open-circuit voltage of the PV cells in series and will try to let a current flow through the diode, which will be blocked. Still, a reverse bias current will flow, but as this current is very low (μA) it is not a problem for the PV system.

5.2.4. Peripherals

MOSFET driver

The function of the MOSFET driver is to optimize the switching performances. Because the driver is not within the scope of this project, only the requirements will be indicated.

First, the driver must have a switching frequency of 150kHz. When the MOSFET is turned on, in an ideal situation, it will only be used in saturation mode. To achieve this mode, the gate-source voltage of the MOSFET must reach a higher voltage than the Miller plateau voltage of the MOSFET. When the driver voltage does not overcome the Miller plateau voltage, the MOSFET stays in linear or resistive mode what causes high energy losses in the MOSFET. Further increase of the gate-source voltage gives a small decrease in on-resistance R_{ds} and a linear increase of the gate charge Q_G . In order to obtain the highest efficiency, the optimal driver voltage must be determined.

Figure 11 of the MOSFET datasheet in Appendix F.1 shows the relationship between the on-resistance as a function of the drain current. The drain current will remain below 10A in the converter. Also illustrated in the figure, the R_{DS} is constant for every chosen driver voltage in this operating region. After that, the figure illustrates the decreasing on-resistance when increasing the gate voltage. Figure 13 of the datasheet shows the gate capacity in comparison to the gate-source voltage. The Miller plateau is reached after a voltage of around 3V.

Because the resulting switching power losses for the chosen MOSFET are higher than the losses in the on-resistance, it was decided to optimize the driver for a minimum gate capacity. This is why the driver must be optimized to the minimal gate-source voltage after the MOSFET reaches the saturation mode. On the other hand, the power loss will increase dramatically when the gate voltage stays low and does not reach the optimum on-resistance. This could be caused by voltage drops in the source inductor, gate resistances or temperature changes. To be very sure this won't happen, the driver voltage must be 4.5V.

The last requirement for the MOSFET driver is the minimum peak current. When the MOSFET turned-on or turned off, the MOSFET driver must be able to supply all the requested power to charging and discharging the gate capacitance. In order to minimize the power losses, the switching period must be minimized when the MOSFET carries a drain-current for a relatively high R_{DS} . Figure 7 of the MOSFET datasheet shows an example for the on-resistance as a function of gate-source voltage what illustrates the high on-resistance of the MOSFET before it reaches the saturation mode. Equations 5.12 and 5.13 show an approximation for the two most critical time periods when the MOSFET is switching through the linear and Miller-plateau region [4]. These equations confirm that, when the driver has an insufficient output current range, the driver will decrease the switching time in the MOSFET, which results in an increase in power losses.

For simplicity, the peak current is empirically determined by LTspice simulations. These simulations show that the maximum gate peak current can reach around 800mA. Because this current could reach higher ranges by temperature changes and higher drain-source voltages, a safety margin must be included. The driver should be able to deliver a peak current of 1000mA.

$$t_2 = C_{ISS} \cdot \frac{V_{GS,Miller} - V_{TH}}{I_{G2}} \quad (5.12) \quad t_3 = C_{ISS} \cdot \frac{V_{DS,off}}{I_{G3}} \quad (5.13)$$

For resonance reduction in the gate, the combined resistances of the driver with gate must conform equation 5.14 [4]. The source inductance L_S must be determined after the converter is real implemented on a circuit board. The C_{ISS} and R_{gi} variables are given in the datasheet of the MOSFET.

$$R_{gate} + R_{driver} = 2 \cdot \sqrt{\frac{L_s}{C_{iSS}}} - R_{g,i} \quad (5.14)$$

5.3. LTSpice model

LT spice is preferred to simulate the electrical circuit. LTSpice is a high-performance simulation software from Analog Devices specific for analog circuits. Besides that, for component models, the software is supported by many electrical component manufacturers, which results in a significant advantage over MATLAB or Simulink. The software is also free to use, making the simulation model easily accessible by other people.

The LT spice boost converter model is shown in Appendix 5.7. The used PV model, on the left, is showed in Appendix D.1. The complete LT spice model with settings and parameters can be found in Appendix D.2.

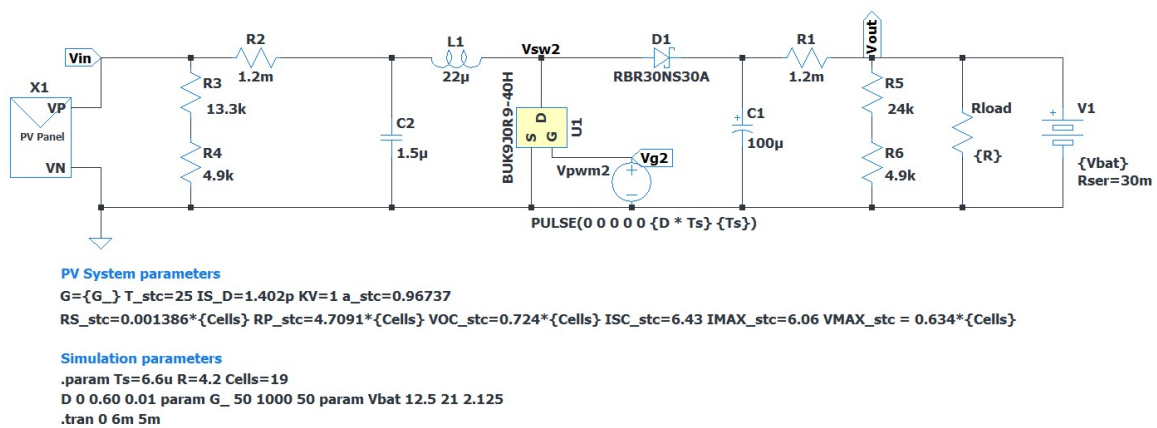


Figure 5.7: LT spice boost converter model

5.4. System integration

For the real implementation, figure 5.8 shows the connections between the power converter and the rest of the systems. The input power has two connections, the positive and negative outputs of the solar panels. The output can be connected to the UBEC or the battery. But because the goal of the project is to increase the flight range, the power converter must be connected to the UBEC, reducing wire resistances. In order to supply the current sensors, the converter needs an input voltage of 5 volts, powered by the UBEC. The power converter has four output signals from the sensors and needs one input signal from the MPPT controller.

Because the results of the solar powered UAV are not tested in real but by simulations, the power converter is implemented in a Simulink model showed in Appendix D.3. The implemented power converter model, showed in Appendix D.4, is simplified to a lookup table to reduce the overall simulation time. These table contains all efficiencies for different situations. These efficiencies can be obtained from three input variables: the PV input power, the switch duty cycle from the MOSFET driver, and the (battery) output voltage. Because the output voltage of the converter is fixed by the battery voltage, is the output of the power converter transposed to a current. This amount of current is added in the system by a variable current source.

The conversion from the LTspice simulation data to the lookup table is done using the Matlab code showed in Appendix E.3 followed by function codes. Because the LTspice simulations will be done in different steps and different computers, the input date files can differ in size or the order of signal sequences. To avoid mistakes being made, the code is automated and adaptive when it loads the data into Matlab. After that, the efficiencies will be calculated. An critical remark, the data from LTspice

are not in constant separated time steps. This issue can be solved by integrating the input and output powers over time, as illustrated in figure 5.9. This results in the approximated in and out flowing energies through the converter over a pre-defined timestep. Dividing the output energy by the input energy results in the converter efficiency. When this job is done, the results will be added to the (existing) lookup table and the data conversion will be finished. Afterwards the lookup table will be saved for the next simulation file.

After converting all data to the efficiency lookup table, the missing data points must be interpolated before it is ready for the Simulink model. The Matlab code to interpolate the lookup table results can be found in Appendix E.4.

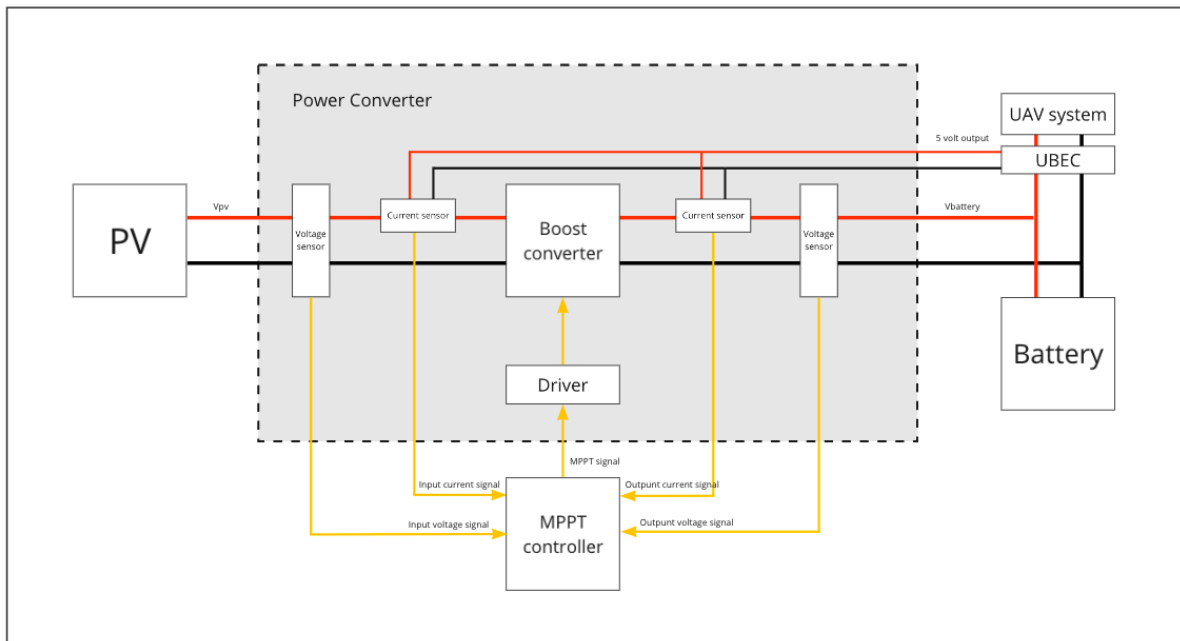


Figure 5.8: Schematic for real implementation

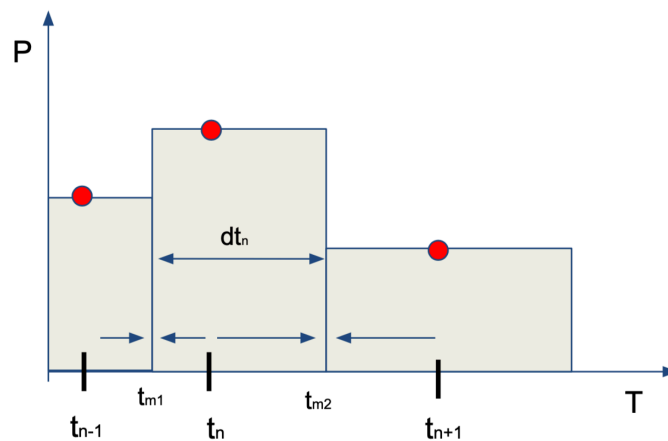


Figure 5.9: Energy calculation

6

Validation

6.1. Introduction

The simulation results of the power converter can be found in this chapter. The ideal simulations are done to get a feeling with the system and to understand the parasitic effects of the real components in the non-ideal simulations. In the non-ideal simulation, the real components are implemented. The resulting efficiencies of the non-ideal power converter are integrated using a lookup table in the Simulink drone simulation.

6.1.1. Simulation results

LTSpice simulation results

Due to the limited time available, approximately 10000 runs have been done for the steps specified Table 6.1. For the duty cycle, a minimum duty cycle of 0 and maximum duty cycle of 0.60, for 8V to 21V conversion, with a safety margin have been chosen.

Table 6.1: Stepped parameter values

Parameter	Values
Output voltage V_{bat}	12,5 – 21V with a step size of 2.125V
Irradiance (G)	50 – 1000 and 25 – 475 W/m^2 with a step size of 50, additional step with value $1W/m^2$
Duty cycle (D)	0 – 0.60 with a step size of 0.01

Power losses The total power loss in the circuit can be expanded to the power losses in the individual components. In Table 6.2, two possible scenarios are considered at its MPP at the minimum, nominal, and maximum output voltage. For the first scenario, an irradiance of $1000W/m^2$ is considered. From Figure 1.2, it is assumed that the average expected irradiance in June is approximately $450W/m^2$. Therefore, this value was chosen for the second scenario.

Table 6.2 shows results corresponding to the expectation of the converter; It is shown that the inductor and diode losses decrease but also that the capacitor and MOSFET power losses increase as the output voltage rises. The higher diode losses at a lower voltage are caused by the lower duty cycle, which leads to a larger time interval in which the diode will conduct. For the MOSFET, this is the exact opposite, as the duty cycle increases, it will conduct for a longer time interval, which leads to increased losses due to the R_{on} . Furthermore, the inductor losses decrease with a higher duty cycle, as the voltage is divided over the ESR of the inductor and the R_{on} of the MOSFET, instead of the much lower ESR of the capacitor. Lastly, a higher potential across the capacitor leads to increased losses at a higher voltage. These capacitor losses are minimal compared to other losses in the circuit due to a relatively low ESR, even when the output voltage is increased.

Table 6.2: Power losses per component at MPP at STC irradiance and average expected irradiance in June in the Netherlands

Duty Cycle	V_{out} [V]	I_{out} [A]	Inductor	Capacitor	Diode	MOSFET	Sensor (I_{in})	Sensor (I_{out})	Sensor (V_{in})	Sensor (V_{out})	Total loss
$G = 1000W/m^2, V_{in} = 12V, I_{in} = 6.06A$											
0.08	12.5	5.48	1.39W	0.02W	2.23W	0.12W	0.04W	0.04W	0.01W	< 0.01W	3.88W
0.35	18.5	3.72	1.30W	0.10W	1.52W	0.52W	0.04W	0.03W	0.01W	0.01W	3.52W
0.43	21	3.43	1.27W	0.12W	1.32W	0.68W	0.04W	0.02W	0.01W	0.01W	3.47W
$G = 450W/m^2, V_{in} = 12.1V, I_{in} = 2.74A$											
0.06	12.5	2.53	0.29W	< 0.01W	0.92W	0.10W	0.01W	0.01W	0.01W	< 0.01W	1.34W
0.35	18.5	1.69	0.26W	0.03W	0.62W	0.25W	0.01W	< 0.01W	0.01W	< 0.01W	1.19W
0.42	21	1.46	0.22W	0.04W	0.54W	0.31W	0.01W	< 0.01W	0.01W	0.01W	1.15W

Input current ripple The specified input ripple was to be around 30%. This percentage had been chosen, such that the inductor operates in CCM under average operating conditions but does not take long to reach steady-state, since the input power is variable over time, and the converter is required to respond quickly to changes. According to the inductor calculations, the ripple is at its highest when the converter is supplied with maximum power, and the difference in voltage potential is at its maximum as well. In Figure 6.1, the maximum input ripple is shown for these maximized values. It is seen that the input current ripple has a maximum value of 1.6A, which corresponds to 25,6% of the input current. The lower percentage is due to the input capacitor that has been added.

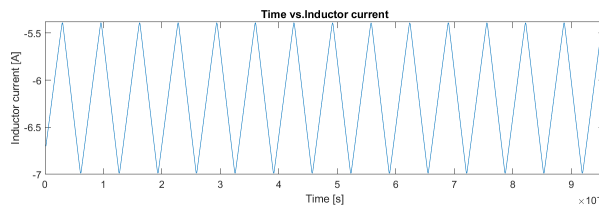


Figure 6.1: Maximum inductor ripple current

Output voltage ripple To check whether the output voltage ripple meets the specified value, the point at which the maximum voltage ripple would occur is taken for measuring this. In Figure 5.2a, it is shown that the maximum capacitance needed occurs at 18V, which corresponds to the highest output voltage ripple. At 18V, Figure 6.2a shows the voltage ripple at the highest possible input power from the PV system, which corresponds to a duty cycle of 0.33 at $V_{MPP} = 12.046V \approx 12V$. It is clear from this figure that a peak-to-peak voltage of $18.05 - 17.91 = 0.14V$ is present. This leads to a ripple percentage of 0.78%. Unfortunately, this is a little bit higher than the specified value. In Figure 6.2b, the output voltage ripple for an ideal circuit is shown. This figure shows that the theoretical calculations were indeed correct, as it has only a ripple of 0.46%. The higher peak-to-peak voltage in the non-ideal model is a result of the parasitic properties of the capacitor, due to the voltage across the resistor in series with the capacitor, the capacitor voltage is actually reaching for a voltage that is a little lower than the battery, or output, voltage when charging. When the switch connects the input of the diode to the ground, the current running through the capacitor will reverse and cause the voltage polarity of the resistor to change, which leads to a small voltage drop at the output terminal. However, it can also be seen that the slope of the voltage decrease, when discharging, is less steep due to the parasitic resistance.

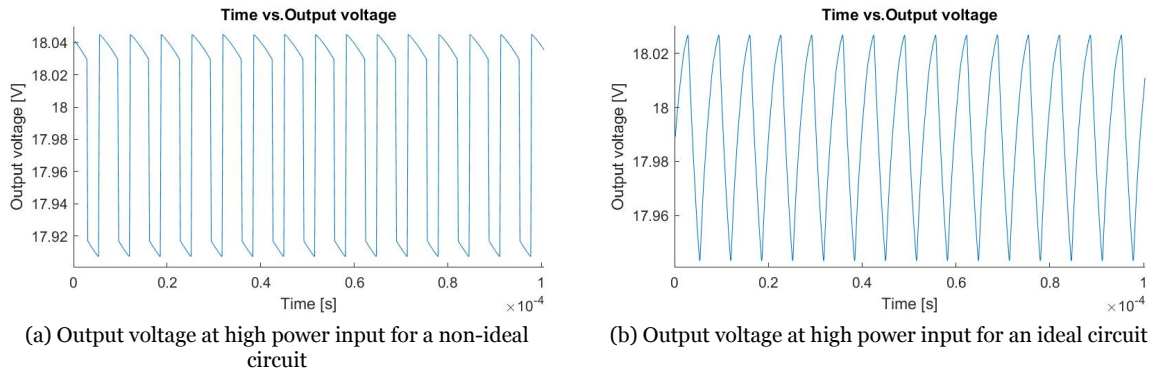


Figure 6.2: Ideal and non-ideal circuit output voltages

Efficiency calculations and interpolation

The code used for importing the data export from LTSpice can be found in Appendix E.1. Figure 6.3 shows the simulated data points. It is shown that the converter’s efficiency decreases quickly for an input power below 1W, which is also shown in Figure 6.5b. The Figures within Figure 6.5 are a 2D representation of the simulated datapoints, as seen in Figure 6.4. For higher input powers, an average efficiency of 95.6% is found. This amply satisfies the requirement of a converter efficiency of 85%. It should also be noted that the efficiency decreases after approximately 8W input power, due to the increased current running through the component resistances.

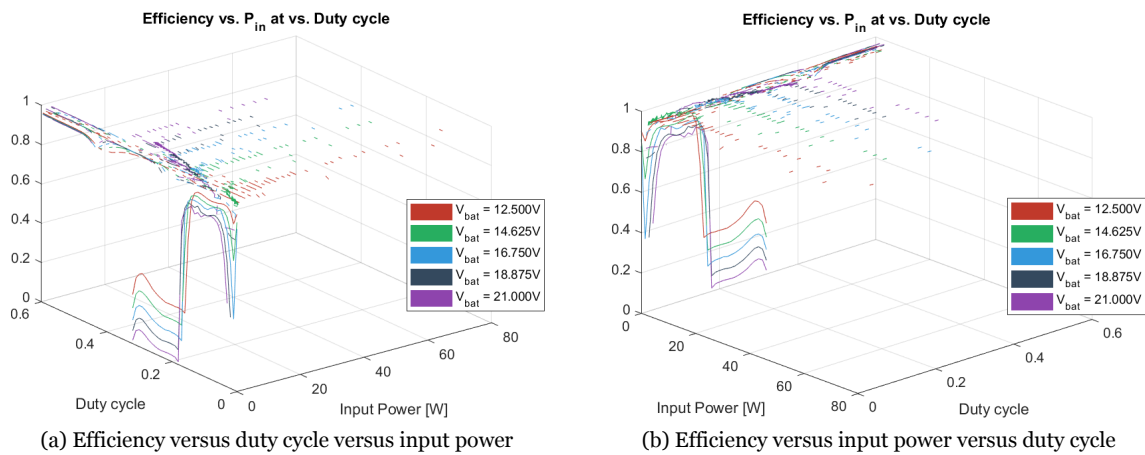


Figure 6.3: Acquired data from the efficiency calculation in Matlab

Duty cycle

The duty cycle influences the operating point of the PV system, which influences the yield of the PV system. In Figure 6.5a, this influence is shown. It should also be noted that the operating mode of the converter will transition to DCM for low input power and current ($< 1A$). However, in Figure 6.5b, it is also shown that no notable difference is observable in terms of efficiency when the converter changes its operating mode. At an efficiency below 90%, five curves for the five different battery voltages are shown with a dip in efficiency. These dips occur at very low input powers, which can be seen from Figure 6.3. The lowest battery voltage shows the best efficiency, which is due to a better matched power point, since at a low input power and duty cycle, the input voltage is also low. In Figure 6.4 is also seen that the respective voltages each have a certain duty cycle at which the PV system it is able to deliver more power. At this point, the maximum power point is reached. At higher and lower duty cycles, a lesser input power is reached. From this, a conclusion can be derived that at this point, the maximum input power is delivered.

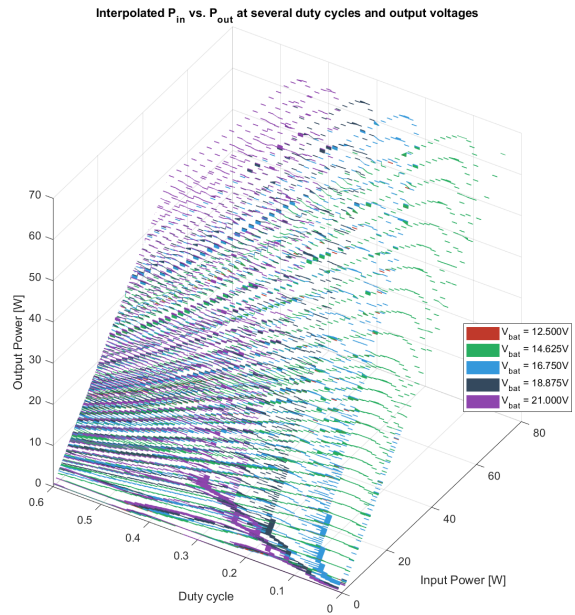


Figure 6.4: Input power versus the output power versus the duty cycle with partial interpolation

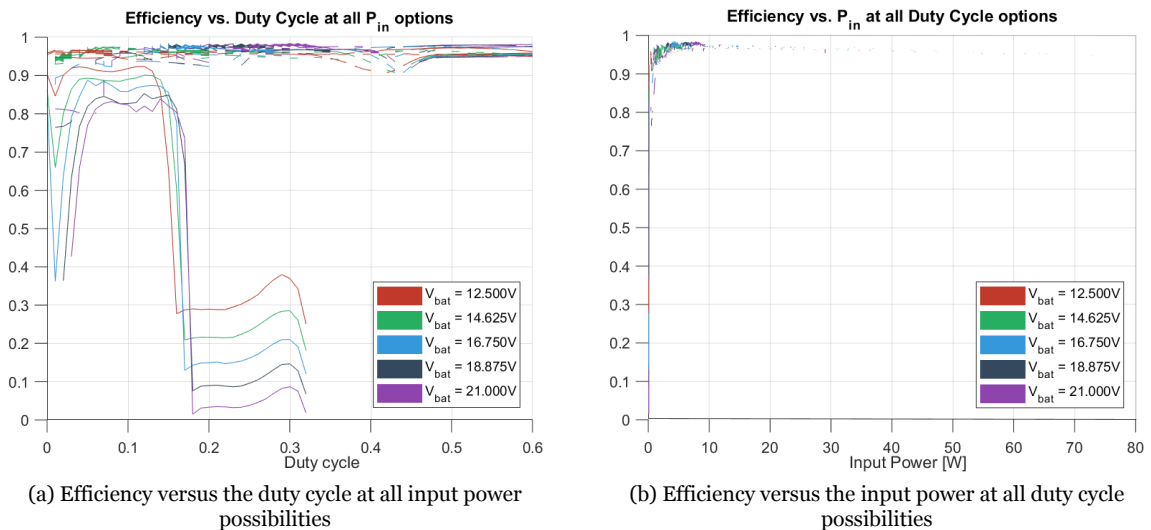


Figure 6.5: Comparison on the influence of the input power and duty cycle on the efficiency

Output voltage

Another factor to be taken into account is the output voltage. The battery voltage range has been separated into 5 values for simulation. The resulting efficiency figures are shown in Figure 6.6. Here, similar efficiency spectra are shown. In Figure 6.6a, the overlay of the Figures 6.6(b-f) is shown. This shows that the interpolation is not always representing an efficient point of operation of the PV. For example, a duty cycle of 0.60 in combination with a battery voltage of 12.5V will result in a low power point. This would correspond to an input voltage of approximately 5V and, according to the PV specifications for an irradiance of $1000W/m^2$, $V_{MPP} = 12.046$. The input power at this point would be 31.4W instead of the around 70W, that is shown in the graph. Therefore, the MPPT algorithm will not move the operating point in this region in the general simulations.

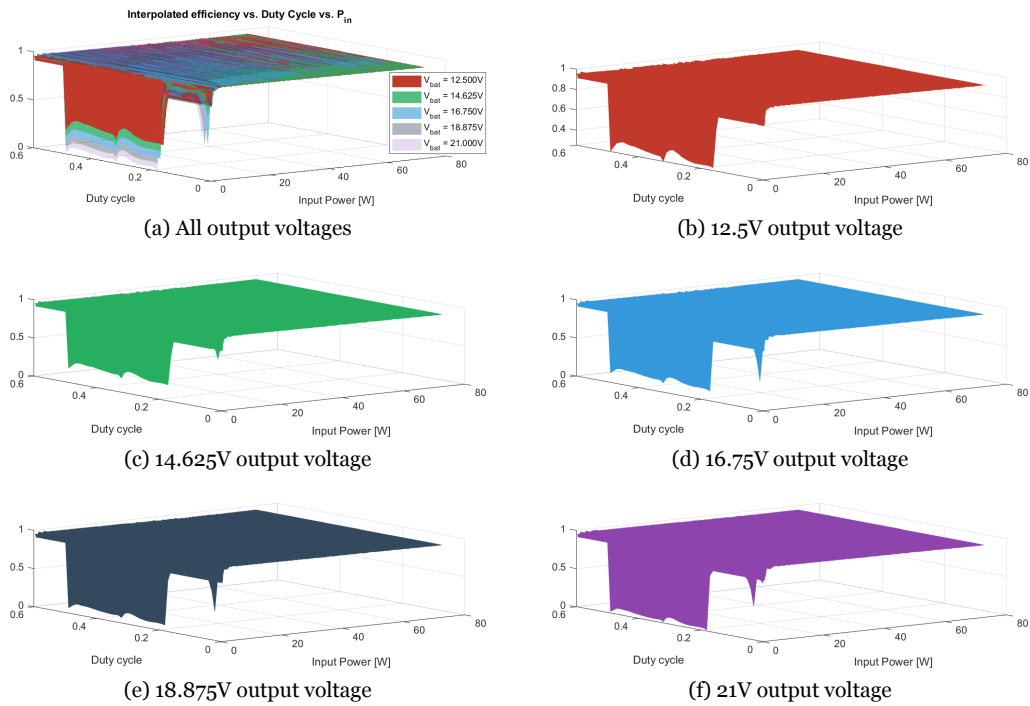


Figure 6.6: Interpolated efficiencies at several output voltages versus the duty cycle and input power

Comparing the input and output power shows another interesting detail. In Figure 6.7a, the data points that have been acquired from the simulation are shown without interpolation. From this figure, it is seen that higher output powers at higher duty cycles are acquired at a battery voltage of 21V. The interpolated data is shown in Figure 6.7b, where the interpolation shows that the higher output voltages for the most part also result in higher output power. The most apparent reason for this is that at a higher output voltage, the diode forward voltage has a lesser effect on the efficiency, as a higher output voltage results in a lower output current for the same output power. This results in a lower current through the diode and thus also less dissipation as the voltage drop remains relatively constant.

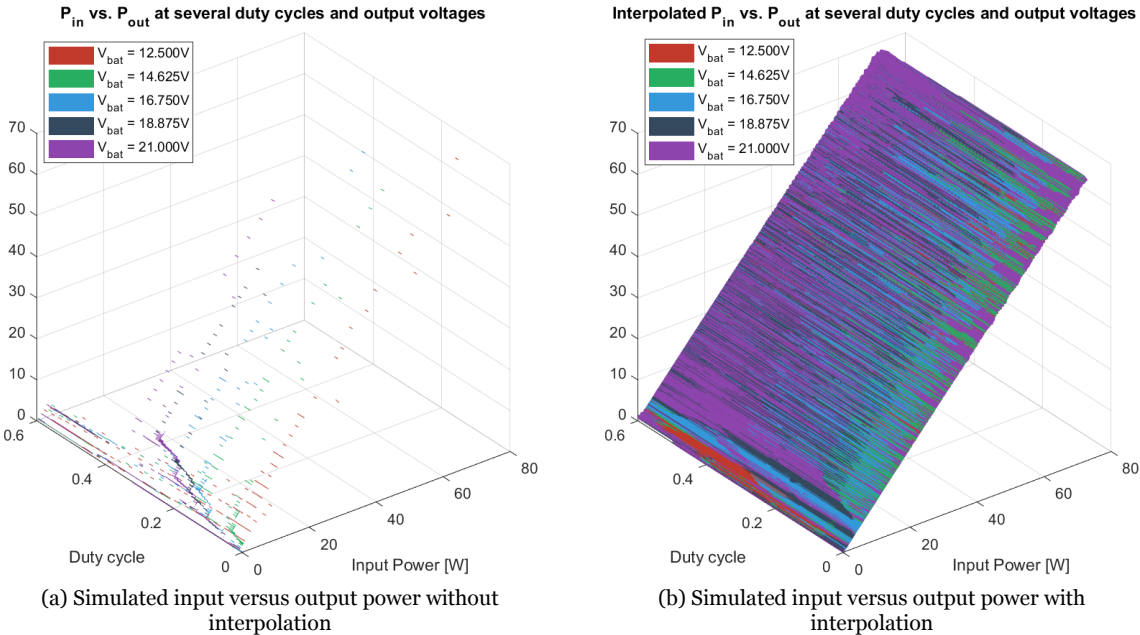


Figure 6.7: Comparison on the performance of the converter input, output power versus the duty cycle

7

Discussion

7.1. Limited data points

Due to the limited time available, about 10000 runs have been done for the simulations. The limited amount of runs resulted in a coarse sweep, in which selective ranging of the duty cycle, output voltage, and irradiance had to be applied. I.e. the duty cycle ranges have only been done from 0.00 to 0.60 with a step size of 0.01. A smaller step size would have granted more data points, and from this, it could lead to more accurate results. The same principle goes for the output voltage and irradiances, where also relatively large step sizes have been applied, of $2.125V$ and $25/50W/m^2$, respectively. The results between the output voltages have been interpolated in order to grant more data points. However, using this method, unexpected behaviour that occurs in between these points can not be accounted for.

7.2. Sampling method

The sampling method that is shown in Figure 5.9 for determining the efficiency of the converter for some run also has some limitations. As it uses a Riemann sum like approach, the efficiency acquired from this is subject to a small deviation. Comparisons between the Matlab approximation and the LT-Spice integral method have shown that the maximum error in efficiency for this is 0.5%. However, not all samples have been compared, and therefore, it is possible for a larger deviation to exist somewhere.

7.3. Irradiance

In this thesis, it is assumed that the irradiance will never be higher than $1000W/m^2$, as is in accordance with Figure 1.2. However, in certain scenarios, the irradiance can be higher than $1000W/m^2$. The effect of this higher irradiance on the functioning has not been taken into account. In future research, this could be considered.

7.4. Temperature influence on PV modules

Another potential issue that is not accounted for is the influence of the variation of temperature on the PV cells. In Figure 7.1, the effect of temperature on PV modules is shown for several different temperatures. It shows that as the temperature increases, the short-circuit current increases, and the open-circuit voltage decreases. This may lead to a higher input current, which subsequently can cause a higher output ripple and more losses in components. It should be noted, however, that the increase in current at a higher temperature is tiny. In the figure, it is also seen that the short-circuit currents do not have a great difference. Therefore, the effect might be negligible. Nevertheless, before a definite conclusion on this, this should be researched and taking the temperature into account for future research could be an improvement over the existing model.

7.5. Other non-idealities

For the sake of simplicity, non-idealities such as ESL, ESC, and wiring resistances have been ignored. This may lead to a deviation in results and could be considered for future research.

7.6. Output current sensor

The output current sensor in the model at this point has no particular function within the model. The initial implementation of this sensor was in order to have all possibilities open for an analog fallback circuit. However, since this turned out to not be possible in the given time frame, it has no function. Therefore, however small the losses in the current sensor are, it should have been omitted in the final model, as it does affect the efficiency of the converter.

7.7. Input voltage

Lastly, the assumption has been made that the maximum power point voltage of the PV system will not lie higher than 12.5V. It is possible that there exists a better operating point above 12.5V in a certain scenario, such as, for example, when the temperature of the PV cell is very low. However unlikely, if in this specific case, the battery voltage is at its lowest, this boost converter will not be able to track the maximum power point properly.

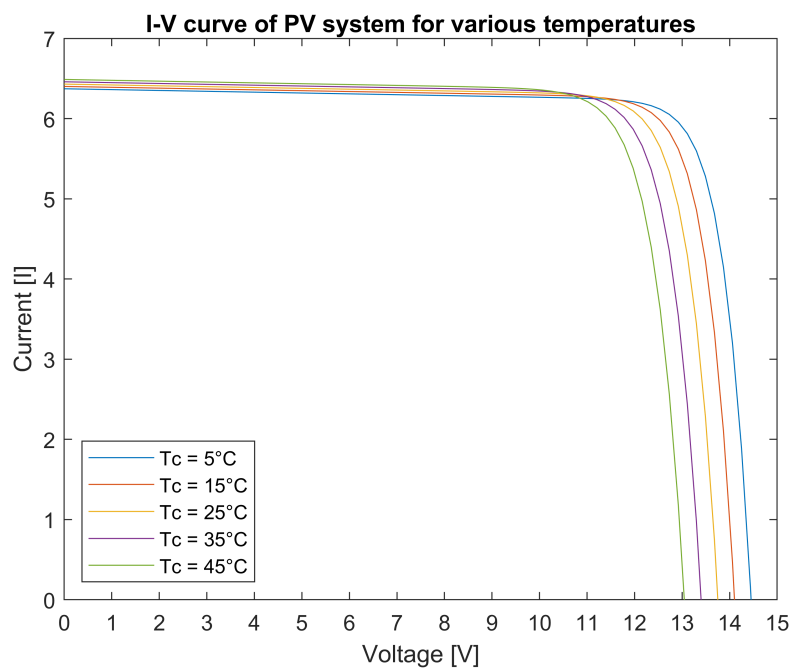


Figure 7.1: Influence of temperature on PV modules (Irradiance: $1000W/m^2$) [9]

8

Conclusions and recommendations

8.1. Conclusions

In this thesis a boost converter that is able to control the MPP is proposed. This model has integrated current and voltage sensors, at both the input and output in order to provide the necessary measurements for the MPPT controller. It is shown that, according to the simulated model, the converter is able to operate efficiently at an expected efficiency of 95.6%. The peak-to-peak voltage that was simulated turned out to be 0.28% higher than the specified voltage ripple of 0.5% due to the ESR of the capacitor. Although this difference is greater than specified, it did show better smoothing capabilities than the ideal capacitor implementation.

In Appendix B, the results of the final simulation, which has the converter's lookup table integrated, show that at the worst case assumed irradiation the range of the drone is decreased with 4%. In the best case scenario, the range is increased by 83%.

8.2. Recommendations

8.2.1. Diode replacement

Although the efficiency of the topology used in this report is high, it is clear that most of the losses originate from the diode, especially at lower battery voltages with a lower duty cycle. Due to the lack of time, it was not possible to further optimize the circuit by replacing the diode by a MOSFET. However, as can be seen in Figure 8.1, a MOSFET would result in less losses for a output current $I_{out} < 30A$. This model does not account for switching losses. However, for future research, a MOSFET should be considered, in order to possibly optimize the efficiency even further.

8.2.2. MOSFET implementation

The selection of the MOSFET is done by ordering the critical values and checking the most significant power loss in the MOSFET. In this design, the MOSFET is optimized for the higher input powers, that's why a low drain source resistance is chosen above a low gate capacity. Another possible improvement over the current model is discussed. More specifically, for choosing a better MOSFET, in order to optimize the power converter efficiency even further.

The resulting power losses of the selected MOSFET could be found in figure 8.3a. This figure illustrates that the constant switching losses are higher than the drain source losses. So finding a better balance between Q and R_{DS} results in a MOSFET with a higher power efficiency. For illustration, the expected powerlosses at $V_{ds} = 4.5V$ for the Nexperia PSMN3R3-40YS MOSFET can be found in figure 8.3b. This MOSFET has a better balance between the gate charge and on-resistance what results a decreased total power loss in comparison to the chosen BUK9J0R9-40H MOSFET.

At the end, it is clear from the RQ ratio, described in section 5.2.1.3, when there are low input powers, the gate capacity becomes more dominant. For a better efficiency at low input powers, it can be interesting to implement a second MOSFET with a minimal gate capacitance. Figure 8.2 illustrates the

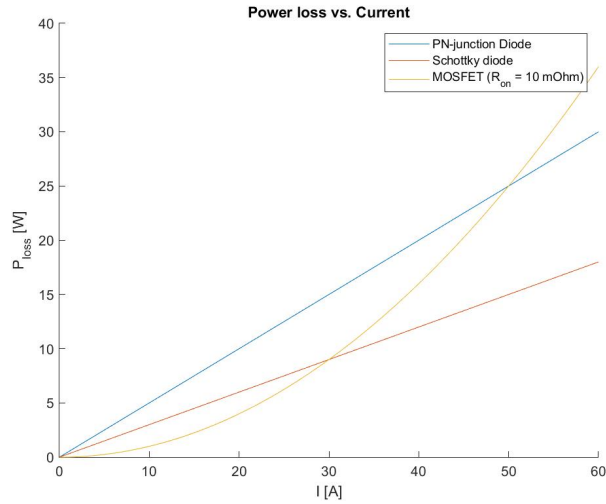


Figure 8.1: Comparison between a MOSFET (NMOS), PN-Junction diode and

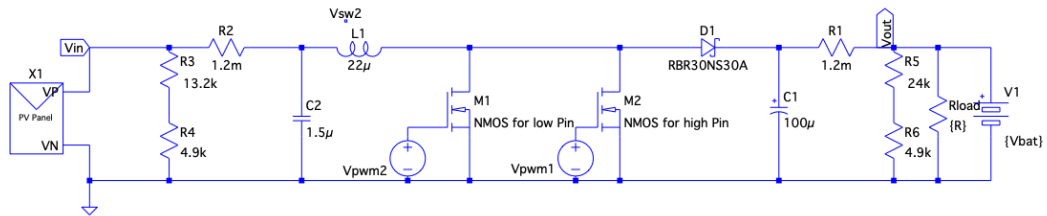
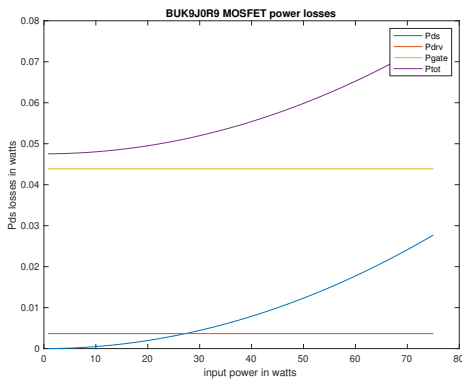
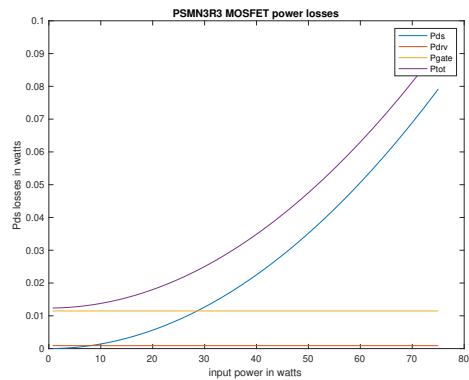


Figure 8.2: Double MOSFET design

design how to implement this second MOSFET. For low input powers, the MOSFET with the optimized gate capacitance is switching the inductor. For higher input powers, the MOSFET with an optimized drain source resistance will operate. This operation could be controlled by the MPPT controller or the MOSFET driver.



(a) Expected powerlosses BUK9J0R9-40E MOSFET @Vds=4.5V



(b) Expected powerlosses PSMN3R3-40YS MOSFET @Vds=4.5V

Figure 8.3: Comparison on the the expected power losses of two different MOSFET types

A

Appendix

A.1. Terminology

- UAV - Unmanned aerial vehicle
- MPP - Maximum power point
- MPPT - Maximum power point tracking
- ESR - Equivalent series resistance
- ESL - Equivalent series inductance
- ESC - Equivalent series capacitance
- ESC (alt.) - Electronic speed controller
- PWM - Pulse width modulation
- MOSFET - Metal-oxide-semiconductor field-effect transistor

A.2. Symbols

A.2.1. General

- P_{in} - Input power of the converter [W]
- r_I - Current ripple percentage [%]
- I_{pp} - Peak-to-peak current [A]
- r_V - Voltage ripple percentage [%]
- V_{pp} - Peak-to-peak voltage
- V_{out} - Output voltage of the converter [V]
- V_{bat} - Battery voltage [V]
- I_{out} - Output current of the converter [A]
- I_D - Diode current [A]
- V_{DF} - Forward voltage across the diode [V]
- C_{in} - Input capacitance [F]
- C_{out} - Output capacitance [F]
- $E_{Store,MAX}$ - Maximum energy capacity to be stored during one cycle [J]
- $E_{L,MAX}$ - Maximum energy capacity that can be stored in the inductor [J]

- $E_{C,MAX}$ - Maximum energy capacity that can be stored in the input capacitor [J]
- D - Duty cycle

A.2.2. PV System

- V_{PV} - PV system output voltage [V]
- $V_{PV,MAX}$ - PV system maximum output voltage [V]
- I_{PV} - PV system output current [A]
- $I_{PV,MAX}$ - PV system maximum output current [A]
- P_{PV} - PV system output power [W]
- $P_{PV,MAX}$ - PV system maximum output power [W]
- V_{MPP} - Voltage at the maximum power point voltage [V]
- I_{MPP} - Current at maximum power point [A]
- P_{MPP} - Power at maximum power point [W]
- N_c - Number of PV cells in the PV system
- V_{oc} - Open-circuit voltage at STC [V]
- I_{sc} - Short-circuit current at STC [A]
- G - Solar irradiance [W/m^2]

A.2.3. MOSFET

- Q_G - Gate charge [C]
- R_{Gate} - Gate resistance [Ω]
- $R_{G,I}$ - Gate input resistance [Ω]
- R_{on} - On resistance [Ω] (alt. R_{DS})
- R_{HI} - Driver 'On' resistance [Ω]
- R_{LO} - Driver 'Off' resistance [Ω]
- V_{GS} - Gate-source voltage [V]
- V_{DS} - Drain-source voltage [V]
- I_{DS} - Drain-source current [A]
- V_{DRV} - Driver voltage [V]
- $P_{DRV,ON}$ - Power dissipated by the driver during the "ON" state [W]
- $P_{DRV,OFF}$ - Power dissipated by the driver during the "OFF" state [W]
- P_{DRV} - Power dissipated by the driver [W]
- f_{DRV} - Driver frequency [Hz] (alt. f_{sw})
- P_{Gate} - Power dissipated by the gate [W]
- P_{sw} - Switching power [W]
- f_{sw} - Switching frequency [Hz] (alt. f_{DRV})
- T_{sw} - Switching time [s]
- T_{on} - The time that the MOSFET is switched on [s]

B

Drone documentation

BACHELOR END PROJECT

DRONE DOCUMENTATION

June 19, 2020

– Solar Powered drones –
Laura Muntenaar,
Martin Geertjes,
Rik van der Hoorn,
Jasmijn Koning,
Jetse Spijkstra,
Sjoerd Groot

Contents

1	Introduction	1
2	UAV selection	2
2.1	Multi-rotor	2
2.2	Single-rotor	3
2.3	Fixed-wing	3
2.4	Fixed-wing hybrid.	3
2.5	UAV type selection	4
2.6	UAV selection	6
3	Component selection	7
3.1	Auto-pilot.	7
3.2	Propeller	7
3.3	Motor	8
3.4	Speed controller	9
3.5	Battery	9
3.6	Camera	10
4	System overview	11
4.1	Introduction	11
4.2	Costs	11
4.3	Component fit	12
4.4	Inter-Component relationship	13
5	Flight simulation	14
5.1	Introduction	14
5.2	Aerodynamic model	14
	Simulink implementation of the aerodynamics	14
	Mass and angle of attack sweep	16
6	Final simulation	18
6.1	Introduction	18
6.2	Simulink Implementation.	18
6.3	Results of final simulation.	19
6.4	Flight path calculation	20
6.5	Power consumption in flight	22
	Bibliography	24
A	Components	25
B	Results	31

1

Introduction

With renewables being on the rise, green solutions are being investigated for every market. This thesis revolves around the idea that the flight range and flight time of commercially available drones could possibly be elongated by the addition of solar panels. In order to do this, a drone is proposed which has the ability to accommodate solar panels and thus can provide its on board system with additional power to elongate the flight range.

This thesis is structured as follows. First the UAV type is selected, then the actual drone frame and the additional components are selected. Finally the drone is simulated and final results are elaborated on.

2

UAV selection

For the UAV selection, it is important to understand which types of UAVs there are. Four types of UAVs are considered and discussed: multi-rotor, single-rotor, fixed-wing and fixed-wing hybrid.

2.1. Multi-rotor

A quadcopter is what is generally thought of when thinking of a UAV, which is a subclass of the multi-rotor class. Typically it is driven by four rotors, where the direct opposite rotors spin in the opposite direction. This type of UAV is the easiest to engineer, since as long as the rotors are spaced in a symmetrical way it will fly without problems. Stability and flexibility are two of the main advantages of a quadcopter; it can suspend itself in the air and take photos from a still position. Furthermore, it can move very flexibly, in any direction at any given time, which may prevent crashes in tightly packed neighbourhoods. Finally it will not need a lot of space for take-off since it can take-off vertically. However, there are also some disadvantages to this design, among which is the fact that it is less-efficient than airplane solutions [6]. Secondly it is difficult to keep the camera angle compared to the ground constant, since the angle of the quadcopter changes when moving and hovering. One of the most important advantages is the fact that a quadcopter could have a large area available for the placement of PV panels, which would benefit the purpose of our project. An extensive overview of advantages and disadvantages of a quadcopter are listed in table 2.1.



Figure 2.1: Quadcopter example [8]

Table 2.1: Advantages and disadvantages of a quadcopter

<i>Advantages</i>	<i>Disadvantages</i>
Easy to engineer	Less energy efficient than airplane solutions
Can take still photos	Photos while moving changes camera angle
Very flexible movements	Simple square shape is more fragile
Possibly a lot of area for solar panels	Low payload

2.2. Single-rotor

A single-rotor, or helicopter, type of UAV is contrary to the fact that it is called a single-rotor type, two rotors. These rotors consist of a large rotor and a smaller, tail rotor. These types of UAVs are much more efficient than its multi-rotor counterpart [10], but still less efficient than a fixed-wing solution according to [6]. Besides that, such a solution has little to no suitable room for solar solutions. Therefore, these types will not be further considered since they are not a suitable solution for solar powered UAVs.



Figure 2.2: Single rotor example [1]

2.3. Fixed-wing

Next to this distinction, another type of drone can also be investigated, the fixed-wing. Fixed-wing type UAVs are entirely different in build and using purposes. Where rotor types are able to suspend themselves in mid-air, fixed-wing UAVs are constantly moving at a certain horizontal speed. They remain at altitude by the lift force generated by the wings, which counteracts the gravitational force. This way, it moves in a more efficient way than a rotor type UAV. This, and the fact that it is always moving, is why it is very suitable for long distance operations, such as mapping. The main disadvantage of a fixed-wing solution is that it is less flexible in moving around mid-air and needs either a runway (a small grass field is usually enough) or some sort of launching base to propel it into the air

Table 2.2: Advantages and disadvantages of a fixed-wing UAV

<i>Advantages</i>	<i>Disadvantages</i>
More energy efficient	No photos from still position / cannot suspend in mid-air
Constant angle while moving (at equal altitude)	Only suitable area for solar panels is on the wings
More robust shape	Needs a runway or launching mechanism
Higher payload	

2.4. Fixed-wing hybrid

The final type researched is a fixed-wing hybrid UAV. This type of UAV has VTOL (Vertical Take-Off and Landing) capabilities and can take-off and land vertically as the name suggests, while in the air flies like a fixed-wing UAV. With this design the aim is to combine the benefits of a multi-rotor with the flying efficiency of a fixed-wing UAV. However this leads to a complex design and a bigger chance of complications during flying.



(a) Fixed wing drone [12]



(b) Fixed wing hybrid [7]

Figure 2.3: Fixed wing vs Fixed wing hybrid

2.5. UAV type selection

For the drone selection, a few criteria are important. The table on the next page shows these criteria per section for the four types of drones we distinguished. All the way on the right, the weight per criteria is indicated, with '10' being the most important and '1' being not important at all. From this table it becomes clear that a fixed wing is the best option, especially when the red factors are taken into account. The quadcopter has a low payload capacity and mounting the PV cells would be difficult. For the single-rotor UAV, the placement of the PV cells would also be difficult. The concept of a VTOL UAV is quite new, so the simulation would be difficult to make and the complexity of the design would make it more difficult to make it solar powered. Next to that, it would also be rather expensive.

UAV Types	Multi-rotor	Fixed-wing	Single-rotor	Fixed-wing hybrid	Importance
General specs	Range	short	long	long	10
	Speed	limited	variable	variable	4
	Efficiency	low	high	medium	10
	Flight time	20-30 min	couple of hours	higher than multi-rotor	10
	Payload capacity	small	medium	high	variable
Controllability	In air stability/ camera control	high	medium	high	8
	Runway	VTOL	yes	VTOL	2
	Skill training	not needed	required	required	2
	Controllability	easy	medium	easy	7
	Ability to stay at same height	oke	oke	oke	8
Robustness	Maintenance	not often	not often	often	2
	Waterproof	per case	per case	per case	2
	Shockproof	per case	per case	per case	4
	Possibility changing casing	per case	per case	per case	1
	Attachment solar cells	not easy (payload capacity)	easy	low	medium
Adjustability	Impact of changes on efficiency	high	low	Low	6.5
	Efficiency optimization	low	high	high	10
	Rotor adjustability	high	Medium/High	high	2
	PV potential/Area	High	Medium/High	None	8
	Risk of use	possibly	possibly	yes (strong big blades)	possibly
Other	Easily simulatable	medium	yes if drag constants are known	medium	8
	Costs	low	medium	high	7
	Datasheet	per case	Per case	per case	5
	Remarks				
	Link				

2.6. UAV selection

In the last section, the decision was made to design a fixed-wing UAV. To optimize the performance of the drone all the components needed for the drone are chosen manually and described in chapter 3. To select a frame, the payload capacity has to be high enough to carry all the components and a decent camera for albedo mapping. Furthermore, it should be possible to attach PV cells on the frame. There are a lot of frames available, but in the end the frame of the Skywalker X8 was chosen as it was a frame that was commercially available, easily implemented for simulations and has a large wing area. Next to this, it was a relatively cheap UAV. Models of the frame have been found as well to analyse the aerodynamics of the frame needed for modeling of the entire UAV.



Figure 2.4: The Skywalker X8 [15]

The Skywalker X8 is a fixed wing, single rotor UAV. The specifications of the Skywalker X8 are as follows:

Model	Skywalker X8
Wingspan	2122 mm
Length	820 mm
Payload volume	9550 cm ³
Mean aerodynamic chord	357mm
Max wing curve	8.9 degrees
Typical cruising speed	65 km/hr
Maximum speed	85 km/hr
Body weight	880 g
Maximum take off weight	3200-4200 g

Table 2.3: Frame specifications

The specifications show a large payload volume and high payload capacity for all the components and equipment. Large wings to place the PV cells on, but with a wingspan of 2122mm and the possibility to detach the wings from the body, compact enough for transportation. Finally it is important that there are models available of the frame and aerodynamic specifications can be found or calculated to simulate the characteristics of the frame.

3

Component selection

In this chapter the different components that were chosen for the implementation of our system are discussed. To complete the skywalker X8, an Auto-pilot, propeller, motor, speed controller, battery and a camera needed to be selected.

3.1. Auto-pilot

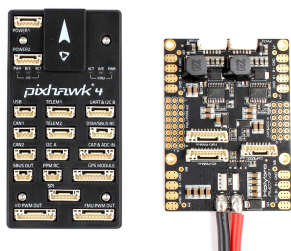


Figure 3.1: Chosen Auto-pilot [3]

The autopilot is a mini computer that controls the motor and servos during the flight using sensor and telecommunication hardware. The requirements for our autopilot are the following:

1. It is commercially available product.
2. Works with other selected components and is easy to implement.
3. Can fly stand-alone.
4. Easy to set way points/flight route to fly.
5. Functionality to implement safety instructions.

Because the the auto-pilot will not be simulated in Simulink and no physical implementation will be made. Little research was done for this component. The above mentioned requirements were taken into account but no comparison was made between all the available auto-pilots on the commercial market. For our application we have chosen the Holybro Pixhawk 4, because this device is affordable and meets our requirements. See the appendix A.2 for the further specifications.

3.2. Propeller

The propeller is able to convert the rotational energy into thrust force. Generally, the greater the propeller area, the higher the thrust force and propeller efficiency, as long as the motor is able to supply the required torque. Also, the propeller needs to fit on the UAV. The recommended maximum propeller size for the frame that was chosen, is 11" x 7", so for the propeller this size is taken. To have useful propeller data, a Graupner Nylon 11" x 7", which is covered in PropCalc [17], was used. The test data provided by this program is shown in figure 3.3, where efficiency is plotted against the speed.



Hobbydirekt.de

Figure 3.2: Chosen Propeller [5]

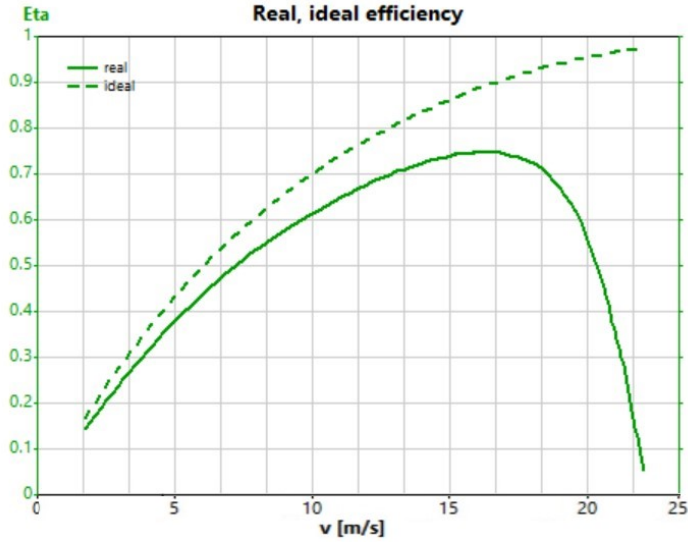


Figure 3.3: Propeller efficiency of the Graupner Nylon 11" x 7" [17]

3.3. Motor

For the motor, the goal is not to create the most efficient drone but to prolong the flight time as long as possible. The most important consideration that is taken into account is the KV. The KV, or RPM/V, depicts how much the RPM of the motor will increase per volt. The KV is linearly dependent on the torque, as is seen in Equation 3.1, where K_t is the torque constant. Furthermore, it is beneficial to have the motor operate at a higher voltage, as this results in a higher efficiency [13].



$$K_V = \frac{1}{K_t} \quad (3.1) \quad \text{Figure 3.4: Chosen Motor [2]}$$

Subsequently, higher torque is needed to drive a higher diameter propeller as a higher diameter propeller has more air resistance or, in other words, can propell more air around. This is why the lowest recommended KV motor was chosen, which is the Turnigy Aerodrive 4250 KV500. However, next to this, the motor should also be able to deliver a power of at least 200W, as this is the expected consummated power by keeping the UAV in the air. The chosen model's specifications are shown in table 3.1.

Specification	Unit
Motor model	Turnigy Aerodrive 4250 KV500
KV	500 RPM/V
Maximum power (5S)	1350W
Maximum current	57A
Burst current	70A
Weight	269g

Table 3.1: Motor specifications

3.4. Speed controller

A speed controller is responsible for the three-phase control of the motor. Therefore it must be able to handle the maximum rated current of the motor, which is 60 A. Other requirements regarding the selection of the speed controller is that it should be light weighted and commercially available.

For the selection of the speed controller the following speed controllers were considered; the Aerostar RVS 60A Electronic Speed Controller w/Reverse Function 5A BEC, YEP 60A (2 6S) SBEC Brushless Speed Controller, Turnigy Plush-32 60A Speed Controller w/BEC and the HobbyKing 60A ESC 4A SBEC. From these options, the Aerostar RVS speed controller was chosen for a number of reasons. First, this controller is able to handle a 60A motor rating that is able to handle the voltage of a five series battery cell configuration. It is also light weight in comparison with the Yep en Turnigy speed controllers, namely 20 gram. Furthermore, it has a build-in Battery Eliminator Circuit (BEC) and the efficiency is known.



Figure 3.5: Chosen Speed controller[11]

The specifications of the chosen speed controller can be found in table 3.2

Specification	Unit
Motor model	Aerostar RVS 60A Electronic Speed Controller w/Reverse Function 5A BEC
Maximum current	60A
Weight	44g
Size	56 x 30 x 14mm
Efficiency	83-87% (Higher efficiency at lower voltages)

Table 3.2: ESC specifications

3.5. Battery

When choosing a battery, a trade-off regarding the battery size should be made. A bigger battery capacity will not always extend the flight range because the weight will also impact the payload and so the power consumption. Therefore, a light weighted but high capacity battery is preferred and a high energy to mass ratio is wanted. The battery also needs to be sufficient for the high current demands of the motor, it must be commercial available and the characteristics of the battery need to be specified for the simulations.



Figure 3.6: Chosen battery[14]

When taking these specifications into consideration, it can be found that li-ion batteries offer the highest energy density and have a storage efficiency close to 100%. The lithium nickel cobalt manganese-oxide (NCM) compound meets the requirements for high specific capacity (mAh/g) and this technology is commercial available.

Within the different commercial NCM li-ion cells, the following types are compared; the Sanyo NCR2070C, Molicel INR21700-P42A, the Samsung INR21700-40T, the Samsung INR21700-30T and the Molicel INR20700A. There was found a good energy/mass ratio of 0.224wh per gram for the Molicel INR21700-P42A. This cell is also able to deliver a high maximum output current of 45A.

After comparing different configurations of this battery cell, the configuration with 5 cells in series and 3 of these series configurations in parallel meets the required capacity, input voltage and the continues current.

Also the weight, volume and expected price fits in the range of the drone specifications. Therefore, this configuration is chosen. The specification of this battery pack can be found in table 3.3. For every series string, a safety component is added that prevents high charge and discharge currents flowing through the battery. The specifications of this safety component can be found in the appendix.

Specification	unit
Battery model	Molicel INR21700-P42A
Voltage	18.5V
Capacity	12000 mAh
Max continues current	135 A
Weight	990 gr
Volume	115.8 cm ³

Table 3.3: Battery Pack specs

3.6. Camera

To be able to create Albedo maps, a camera is needed that is able to create high quality images. Since there are flight-height restrictions imposed by the Dutch government that withholds UAV's to fly higher than certain heights, the camera should be able to create quality images around 120m. To be able to do this it should have a maximum ground spatial distance (GSD) of 20cm at a shutter time less or equal to 1/1000s. Another requirement is that the camera should be able to create RAW linear images to make sure the images are easily edited for Albedo map creating. The camera should have stabilisation in order to be less affected by the turbulence of the UAV and lastly, it should be lightweight and as cheap as possible. The options that were considered were the GoPro MAX, HERO8 Black, AKASO V50, Insta360 ONE X, HERO 7 Black and the Sony Alpha-6000 because these camera's are all compact while having considerably good specifications. However, based on above mentioned specifications the The Sony Alpha-6000 camera with SELP1650 lens is chosen.



Figure 3.7: Chosen Camera [4]

The specifications of the chosen camera can be found in table 3.4

Specification	unit
Camera model	Sony Alpha-6000 camera with SELP1650 lens
Weight	460 gr
Pixels	24.3 MP
Frames per second	11 (in burst mode)
Shutter time	1/4000 s
Maximum field of view	83 degree
Aperture	f/2.8
ISO	100-25600
focal point	15-60mm
focal length	35-75mm
Image output	RAW and JPEG

Table 3.4: Camera specifications

4

System overview

4.1. Introduction

This chapter describes the system overview. First an overview of the weight and cost of the UAV is given. Then the selected components and the selected drone are 3D modeled to show the fit of the described system. Then the inter-component wiring is described and the total system overview is explained.

4.2. Costs

To ensure that the UAV will fly as efficiently as possible, the system needs to be optimized for weight. Next to this, as a business plan has to be generated, the system also has to be optimized for cost. The total weight and cost of all the components and the UAV are described in table 4.1.

Table 4.1: Total weight and cost of UAV

Component	Weight (grams)	Estimation (€)	Costs incl. tax (€)
Body	880	140	239.9
Motor	269	40	38.37
ESC	60	30	30.74
Servo (2x)	40	15	14.22
Propellor	20	15	8.95
Auto pilot/controller	37	180	159.3
Gps for auto pilot	32		
Receiver FrSky R9	5.8	30	29.95
Camera	344	550	650
lens for camera	116		
Battery (18V, 12Ah = 216Wh)	1050	86	123
3x Battery protection	45		45
Wiring and mounting	100		
FrSky Taranis X9 Lite remote ctrl	nvt	120	109
PV panels	616.6	nvt	213.32
Total	3615.4	1206	1661.75

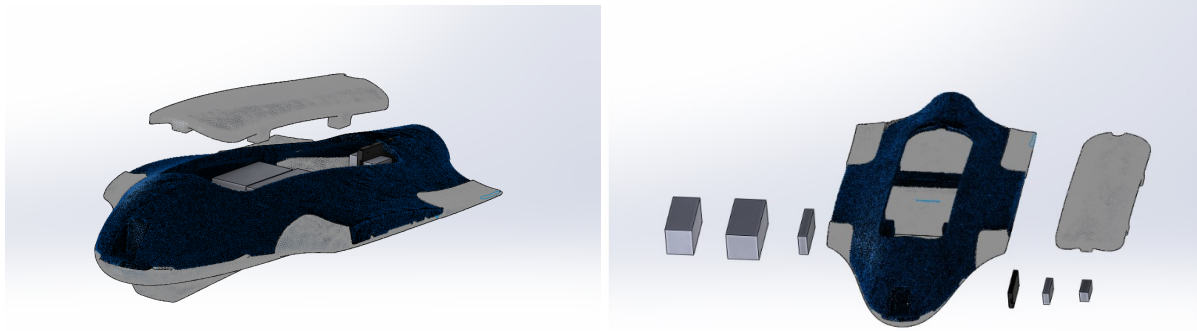
4.3. Component fit

After the selection of all the components and the drone, a model of the components can be fitted into the drone. Although the physical UAV will not be created, an estimate of the component fit and thus the weight distribution can be made. Table 4.2 shows the components referenced in chapter 3 and their respective dimensions.

Table 4.2: Overview of the component dimensions

Component	Length (cm)	Width (cm)	Height (cm)	Total volume (cm^3)	Total volume + 2cm marge (cm^3)
Battery	13.2	6.6	7	609.84	1176.48
Camera	12.0	6.7	4.5	361.8	791.7
Motor	not relevant (own space)	not relevant(own space)	not relevant(own space)		
Speed controller	5.6	3.0cm	1.4	23.52	129.2
Propellor	not relevant (own space)	not relevant (own space)	not relevant (own space)		
**DC-DC controller(power management solar panels)	4.5	2.5	2.0	22.5	117
*micro controller - power management	10.16	5.33	2.0	108.3056	356.5312
flight controller(+ auto pilot)	5.5	3.8	1.55	32.395	154.425
**power system	10	5	2	100	336
GPS Module	5.0	5.0	2.5	62.5	220.5
TOTAL				1320.8606	3281.8362

Figure 4.1 shows the 3D fit of the components in the UAV in solid works. Here, the battery is placed more towards the front (the main box visible) to center the weight of the components around the center of mass of the UAV. Thus stabilizing the UAV.



(a) Top view of components in UAV

(b) From Left to right: Camera, Battery, Power system, Autopilot, Speed Controller, DC-DC

Figure 4.1: Top view and closed view of components in the uav

4.4. Inter-Component relationship

Figure 4.2 shows the general overview of the total system. The power supplies are displayed in blue. On the left, the battery cells are connected to the battery management system. This manages the internal cell voltage and ensures enough power is supplied to the secondary systems, such as the ESC and BEC, which is actually integrated inside the ESC but is displayed separately for the completeness of the model. Below, the PV system is interconnected with the power converter. The power converter, subsequently, is supplied with the necessary control data from the (MPPT) micro controller.

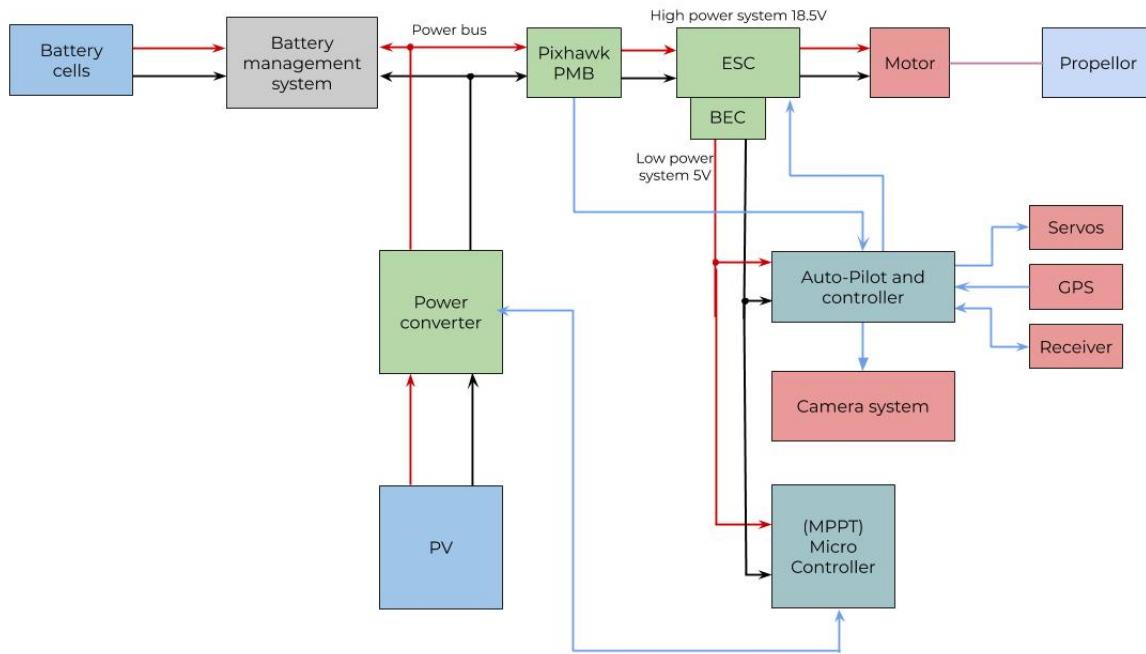


Figure 4.2: System overview diagram

5

Flight simulation

5.1. Introduction

This chapter describes the modelling of the drone. To accurately represent the drone the aerodynamic forces need to be modelled as they influence the power and energy needed for flight. First the general modelling of an air vehicle is explained, then the implementation of the Aerodynamic model in simulink is elaborated on. Next the integration of the electrical And Aerodynamic model is explained. At last, the effect of the aircraft mass and aircraft angle is investigated with the implementation of a mass sweep and an angle sweep.

5.2. Aerodynamic model

When looking at an aircraft, 4 main forces can be identified. The Lift, Drag, Thrust and gravitation force indicate the way the aircraft will fly. Figure 5.1 shows these four forces and their respective orientation with the UAV.

The Lift force is the result of the airflow above and over the wing lowering the air pressure on the top of the wing, which pulls the wing up-wards and will thus push the aircraft up-wards. It is generally seen as the force which counteracts gravity.

The drag force is the result of the air resistance which the UAV encounters whilst moving through the air. This can be viewed as the amount of force it takes to move the UAV through air. The counteract force to drag is the thrust force. The thrust force indicates the force the motor provides to move the aircraft forward.

Figure 5.1 also shows the angle of attack and the flight path angle. The flight path angle (γ) is the angle of the aircraft path with respect to the ground. The angle of attack (α) is the angle between the incoming air the aircraft experiences with respect to the angle of the aircraft.

The aerodynamic model of the airplane is based on the measurement results and aerodynamic simulations presented in [9] and the electric aircraft Model in Simscape [18].

Simulink implementation of the aerodynamics

The main goal of the aerodynamic model is to determine the power that the motor should provide. The architecture of the model is similar to the implementation of [18] however our model does take the angle of attack into account for determining the lift and drag coefficients as seen in Figure 5.2.

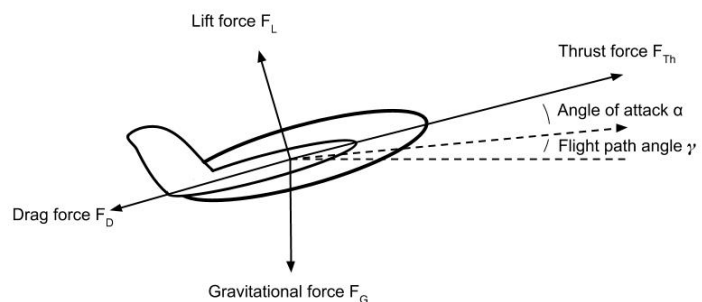


Figure 5.1: Forces on the plane

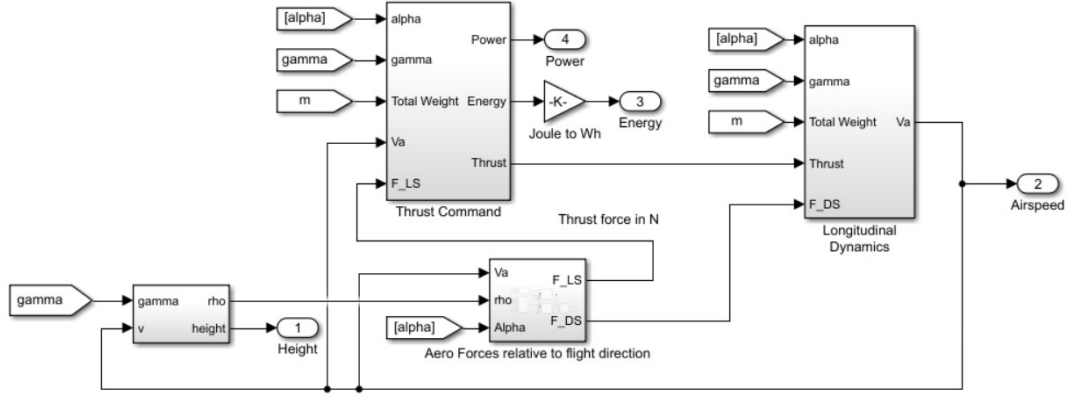


Figure 5.2: Aerodynamics overview

Aerodynamic forces

Table 5.1: Aerodynamic coefficients used as measured by [9]

C_{L_0}	0.0867
C_{L_α}	4.0203
C_{D_0}	0.0197
$C_{D_{\alpha 1}}$	0.0791
$C_{D_{\alpha 2}}$	1.0555

First, the lift and drag coefficients, C_L and C_D respectively, are derived from the angle of attack α according to Equation 5.1 and 5.2.

$$C_L = C_{L_0} + C_{L_\alpha} \alpha \quad (5.1)$$

$$C_D = C_{D_0} + C_{D_{\alpha 1}} \alpha + C_{D_{\alpha 2}} \alpha^2; \quad (5.2)$$

The lift and drag forces, F_L and F_D respectively, are then calculated using the airspeed V_a , air pressure ρ , wing area S_{wing} and the coefficients described above.

$$F_L = \frac{1}{2} \rho V_a^2 S_{wing} C_L \quad (5.3)$$

$$F_D = \frac{1}{2} \rho V_a^2 S_{wing} C_D \quad (5.4)$$

Forces reference system

Three reference frames are present in the simulation as seen in Figure 5.3. Firstly the inertial frame (green) is relative to the ground. This is used for the gravity that is always pointing down. The stability frame (blue) is in the orientation that the airplane is flying. This is the orientation that is relevant to calculate if the airplane accelerates/decelerates and if the lift and motor force counteract the gravity. The third reference frame is the body frame (black) pointing in the same direction as the airplane. This differs from the stability frame because of the angle of attack of the airplane.

The forces of lift, drag and the motor are in the body frame reference. These are therefore rotated by the angle α to go from the body frame to the stability frame.

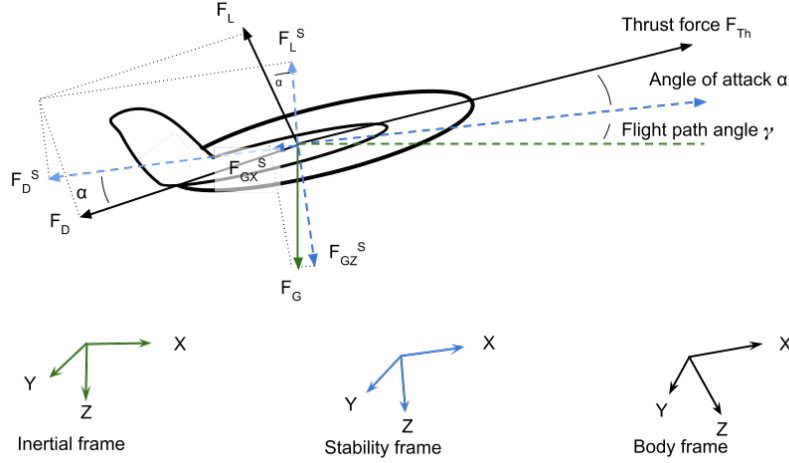


Figure 5.3: Reference systems of Aerodynamic forces

Thrust command and longitudinal dynamics

The required thrust F_{th} , is calculated based on the difference between aerodynamic lift and opposing force of the weight. The propulsion power P , is determined by multiplying the thrust force by the airspeed.

$$F_{th} = \frac{1}{\sin(\alpha)} (F_G^S - F_L^S) \quad (5.5)$$

$$P = F_{th} V_a \quad (5.6)$$

Where F_G^S F_L^S are the gravitational force with respect to the stability frame visible in 5.3. From this thrust, the drag and gravitational forces in the stability reference frame, F_{Gx}^S and F_D^S respectively and the total airplane mass m , the acceleration \dot{v} is determined. The airspeed is determined by integrating this acceleration.

$$\dot{v} = -F_{Gx}^S - \frac{F_D^S}{m} + \frac{F_{thx}^S}{m} \quad (5.7)$$

By integrating the airspeed and taking the flightpath angle into account the height of the plane is tracked and the corresponding air density is determined.

If the airplane didn't had enough lift to counteract the gravity the motor thrust will become larger, this will increase the airplane velocity and this results in more lift generated. This feedback loop ensures that the aircraft will acquire a steady state, ascending or descending according to the flight path angle.

Mass and angle of attack sweep

Figure 5.4 was obtained by simulating the airplane model. On the vertical axis the Maximum flight range, the maximum flight duration the cruising speed and the cruising power draw is shown. In each simulation the airplane starts off thrown at a height of 2 meter and an airspeed of 2 m/s. The plane is instructed to climb to a height of 120m and than to maintain level flight until the battery is empty.

This simulation is performed for different airplane weights and different alpha values to obtain the maximum range for all weight configurations.

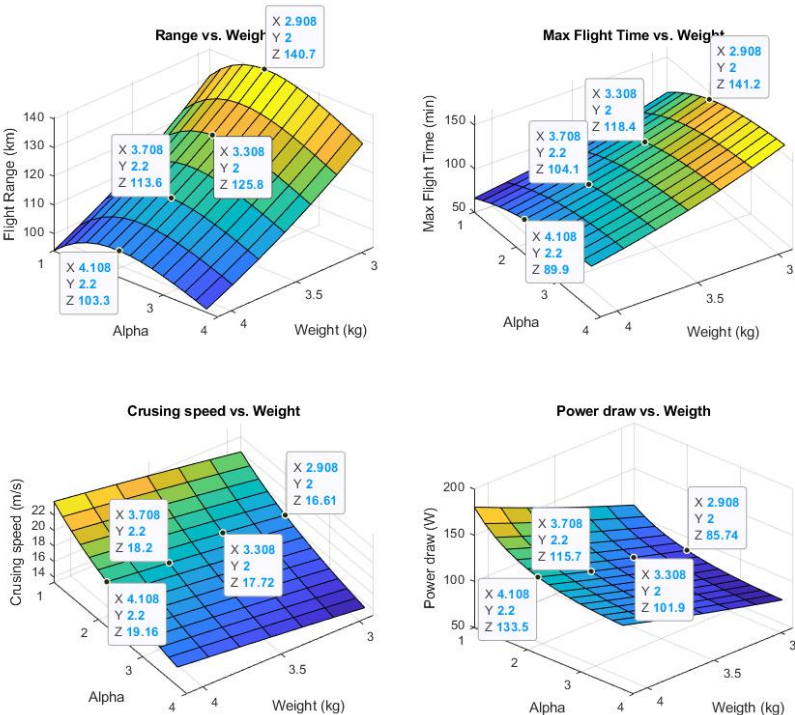


Figure 5.4: Simulation results under varying weight and angle of attack (alpha in degrees)

6

Final simulation

6.1. Introduction

This chapter elaborates on the final simulation done. In this simulation, all the sub-systems were integrated into one big simulation. First the simulink is explained after which the results are discussed.

6.2. Simulink Implementation

The overview of the final simulation can be viewed in 6.1. Here, on the left, the battery and the PV power are inputted which provide power to the system. The PV power can be turned on or off to simulate a cloudy day or a sunny day. On the top right, the flight controller and the aerodynamic model can be found. These simulate the take-off, level flight and landing by adjusting the flight path angle in the aerodynamic model.

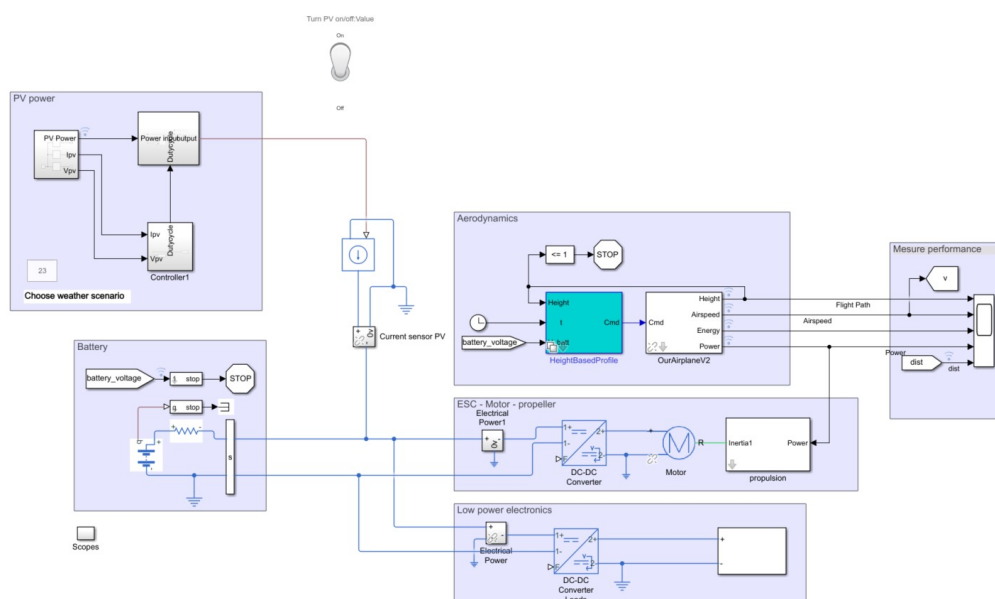


Figure 6.1: Final electrical simulation of the aircraft

The middle block shows the propeller and the motor. The aerodynamic model outputs the power needed to stay in the air. The propeller and motor then adjust accordingly to provide the necessary torque. Lastly, the bottom block represents all the secondary systems which need power like the auto-pilot or the speed controller.

6.3. Results of final simulation

Figure 6.2 shows the additional flight range that the PV panels provide. On the left, the worst case scenario is displayed in which the solar irradiance is 129 W/m^2 and the temp equals 21.1 degrees Celsius. Here the flight range is decreased with 4% by the addition of PV as the PV panels add more weight and dus more power is needed than the PV panels deliver. On the Right, the best case scenario is displayed. In this case, the the solar irradiance is 782 W/m^2 and the temp equals 18.5 degrees Celsius. Here the flight range is increased by 83%.

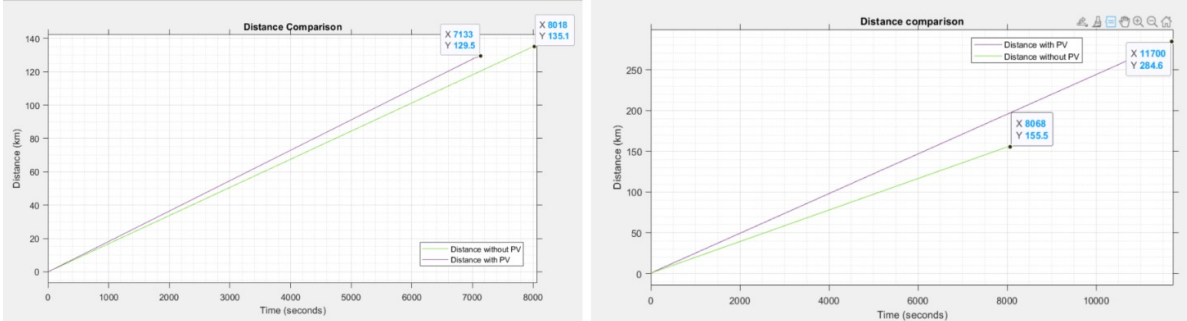


Figure 6.2: Addition to flight range from PV under different weather scenario's

Figure 6.3 shows the overall results of he total simulation, this figure can be found as a larger figure in appendix B.2. In the figure, the purple line represents the simulation in which PV panels are used. The green line represents the simulation without the PV panels. The right On he top left, the increased flight time becomes visible. We can see that the drone will fly for a long period of time before it lands. On the bottom left, it becomes visible that the discharging of the battery goes slower when PV panels are added.

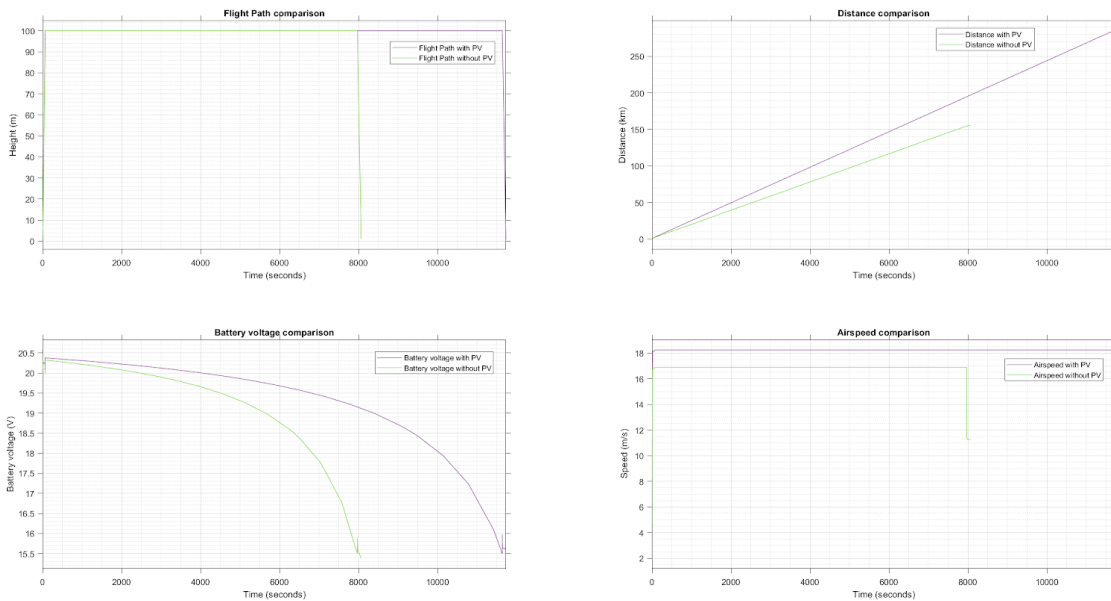


Figure 6.3: Comparison of flight path with and without PV

On the left, the difference in range becomes clear. In this particular situation, as mentioned in 6.2, the solar panels added 83% increase in range.

6.4. Flight path calculation

The flight path of the UAV is dependent on UAV and camera specifications based on the program of requirements, its path should be able generate high quality images while being time efficient. The image will have a good quality when the ground sampling distance (GSD) is lower than 20 cm [16]. The GSD can be calculated using formula 6.1.

$$GSD = \frac{p * H * 1000}{f * \cos d(0.5 * FOV)} \quad (6.1)$$

Here p is the pixel size (micron), H is the flight height (m), f is the focal length (mm) and FOV is the field of view (degrees). The camera specifications can be found in section 3.6. The pixel size can be calculated using formula 6.2

$$p = \frac{s_w}{p_w} + \frac{s_h}{p_h} \quad (6.2)$$

Here s_w and s_h are the sensor width and sensor height respectively and p_w and p_h are the pixel width and pixel height respectively. Based on these calculations, the GSD is 17.93cm when flying at a height of 120m, which is sufficient. Now, another specification that is needed to guarantee the quality of the generated albedo map is image overlapping. There is a forward overlap of images needed of 65% and a sideward overlap of 40% [16]. The following formula's are used.

$$d_{fmax} = \frac{v}{f ps * 3600} \quad (6.3)$$

$$d_{sneed} = \frac{(1 - o_{side}) * H * s_w}{f * 1000} \quad (6.4)$$

In formula 6.3 the forward distance between every picture d_{fmax} (m) is calculated based on the speed v of the UAV (m/s) and the frames per second $f ps$ (1/s), and is 1.6 meter. The needed side overlap d_{sneed} is calculated in formula 6.4 to be 48.5 meters. Lastly, in order to create a flight path, the turning radius of the UAV needs to be calculated. This is done via the following formula's.

$$R_f = \frac{(0.54 * v)^2}{11.26 * tand(30)} \quad (6.5)$$

$$R = \frac{R_f}{\frac{3.28}{1000}} \quad (6.6)$$

$$l_c = 0.5 * \pi * R \quad (6.7)$$

Here R_f is the possible radius in foot, which is dependent of the velocity v of the UAV. In formula 6.6, the radius is transformed from foot to kilometer. In formula 6.7 the minimum length of the turn is calculated. This is 363 meter. Based on previously mentioned outcomes, a flight path is chosen. This can be seen in figure 6.4.

The total flight range is calculated via formula 6.8. Here l_{fl} is the length of the flight lines, which is based on the length of the TU Delft and is 2.1km. l_{ctop} and l_{cdown} are the lengths of the turning circles for the top part of the figure and bottom part of the figure respectively, which are 686m and 609m . n_{rtop} and n_{rdown} are the number of turns for the top and bottom part respectively, which are 9 and 8. l_{to} and l_l are the take-off length and the length for landing respectively. They are both chosen to be 1 km to be on the safe side.

$$d_{tot} = (n_{fl} * l_{fl}) + (l_{ctop} * n_{rtop}) + (l_{cdown} * n_{rdown}) + l_{to} + l_l \quad (6.8)$$

This gives a total flight path length of 48.75 km. The corresponding flight time, given that the speed of the UAV is 65km/h is 00:45 hours.

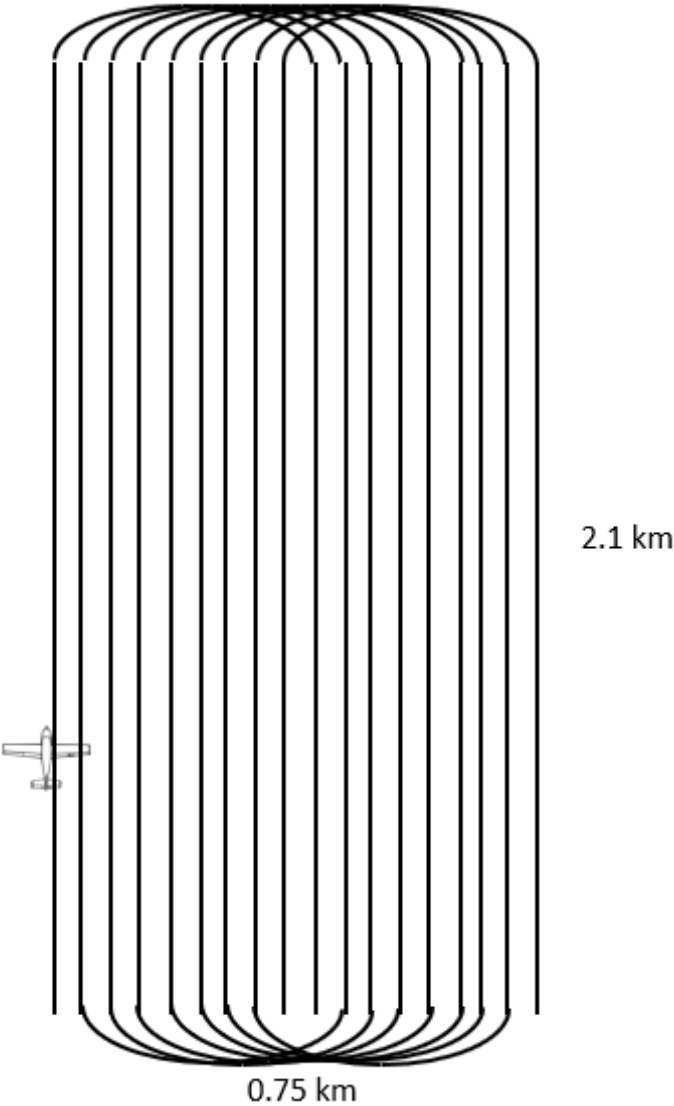


Figure 6.4: Flight path of the area of the TU Delft

6.5. Power consumption in flight

Figure 6.5 shows the power consumption by the system and the power generated from the battery and PV in the best case scenario. The Solar irradiation equals 887 W/m^2 and the temperature equals 21.2 degrees. From this graph, it becomes visible that the solar panels generate about 50W, the battery generates about 60W and the motor + secondary system consume about 110W. Figure 6.6 shows the power consumption by the system

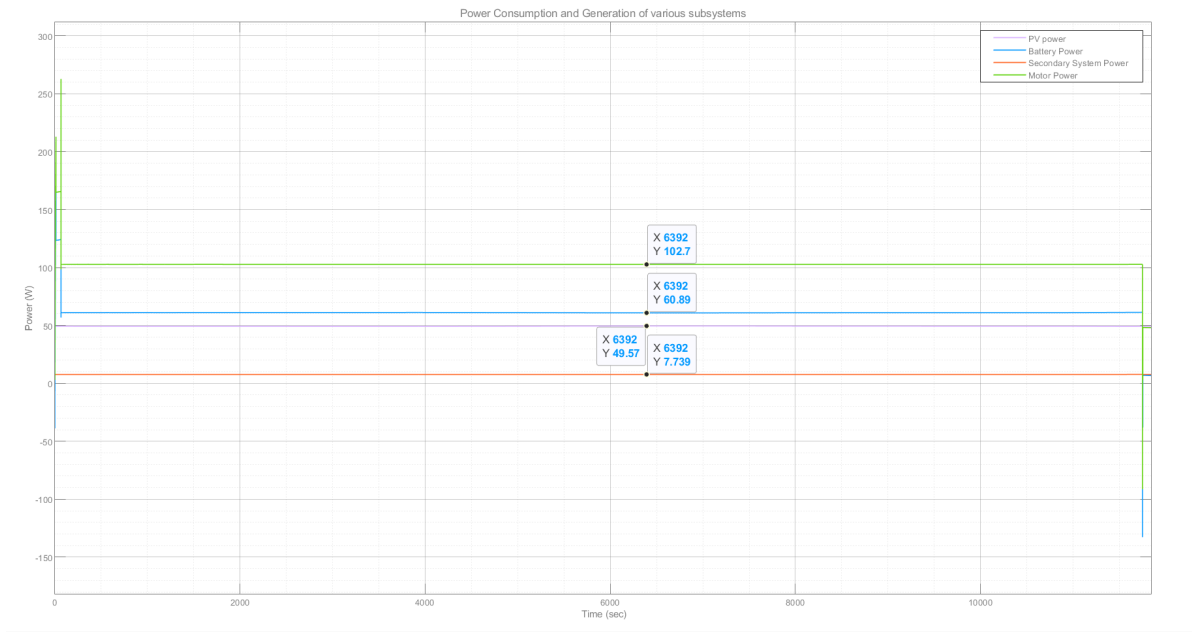


Figure 6.5: Power consumption of the system in the best case scenario

and the power generated from the battery and PV in the worst case scenario. The Solar irradiation equals 0 W/m^2 and the temperature equals 4.4 degrees. From this graph, it becomes visible that the solar panels generate 0W, the battery generates about 100W and the motor + secondary system consume about 110W.

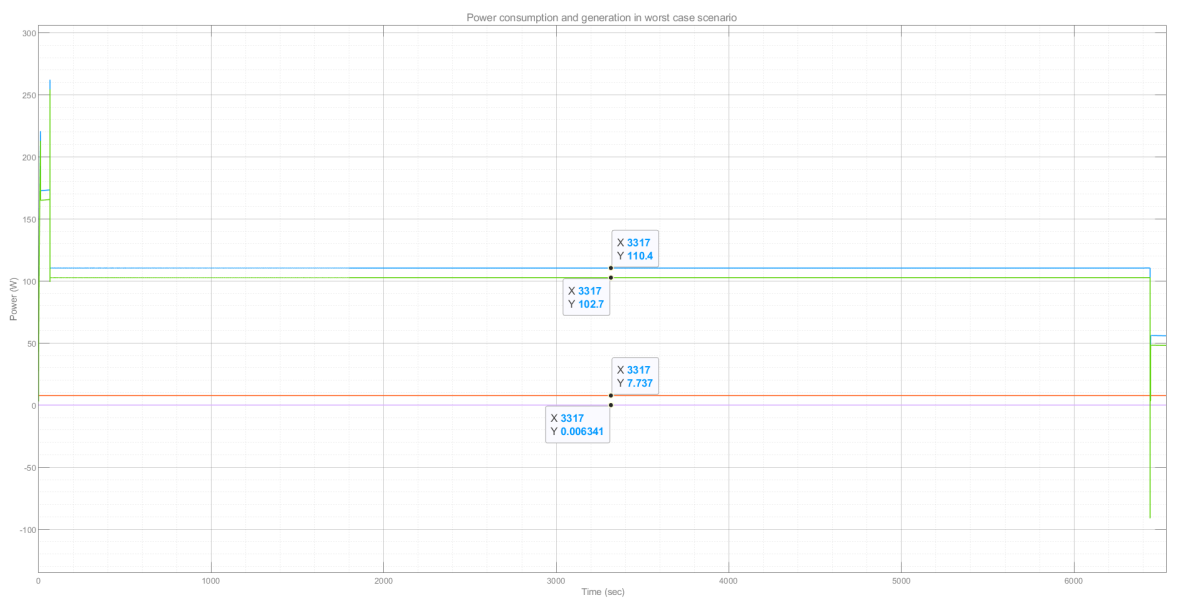


Figure 6.6: Power consumption of the system in the worst case scenario

Figure 6.6 shows the power consumption by the system and the power generated from the battery when no PV panels are added. From this graph, the battery generates about 82W and the motor + secondary system consume about 89W.

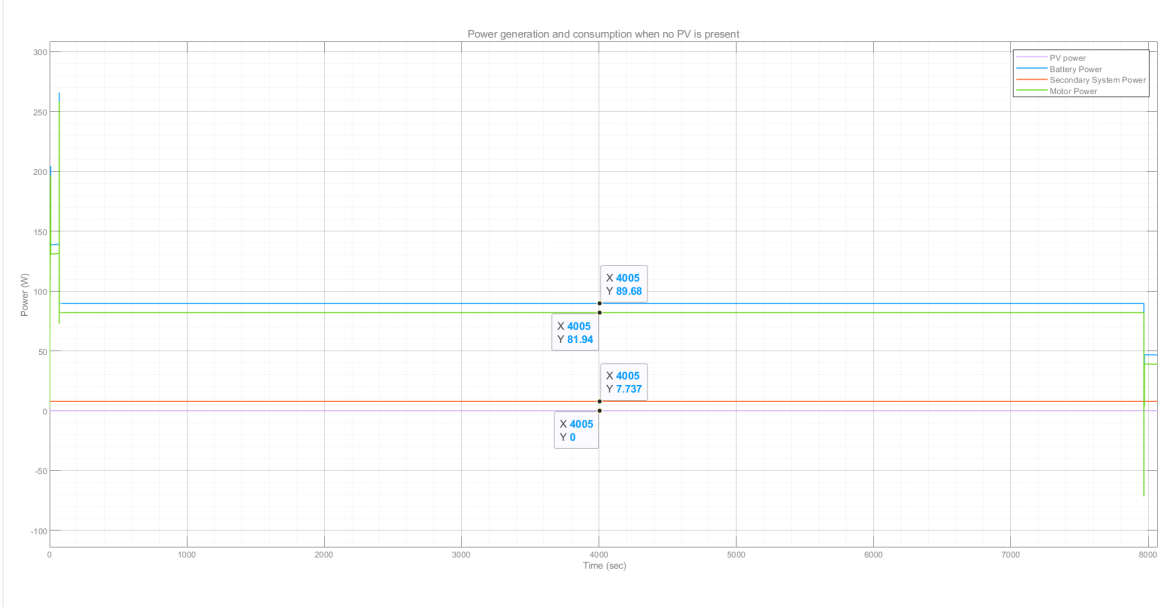


Figure 6.7: Power consumption of the system when no PV panels are added

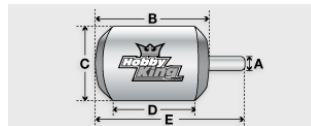
Bibliography

- [1] Alibaba. Single rotor drone. URL https://www.alibaba.com/product-detail/2018Years-Single-rotor-Drone-Agriculture-Sprayer_60761797076.html.
- [2] Allegro. Silnik sk3 4250 kv500 4s-6s li-po turnigy rc. URL <https://allegro.pl/oferta/silnik-sk3-4250-kv500-4s-6s-li-po-turnigy-rc-7150196451>.
- [3] Banggood. Holybro pixhawk 4. URL https://nl.banggood.com/Holybro-Pixhawk-4-PX4-Flight-Controller-STM32F765-32-Bit-ARM-for-RC-Drone-FPV-Racing-p-1302139.html?ID=534789&cur_warehouse=CN.
- [4] Bol. Sony alpha 6000. URL <https://www.bol.com/nl/p/sony-a6000-16-50mm/9200000025106838/>.
- [5] Hobby Direkt. Graupner propeller. URL <https://www.hobbydirekt.de/Zubehoer/Luftschrauben/Nylon/Plastikpropeller/Prop-28x18cm-11x7-Zoll-Graupner-1316-28-18::37462.html?language=en>.
- [6] Dario Floreano and Robert J Wood. Science, technology and the future of small autonomous drones. *Nature*, 521(7553):460–466, 2015.
- [7] Idea Forge. Hybrid fixed wing drone. URL <https://www.ideaforge.co.in/drones/switch-uav/>.
- [8] Geekbuying. Quadcopter,. URL <https://nl.geekbuying.com/item/SHRC-H2-Locke-2K-WIFI-\FPV-RC-Quadcopter-RTF-White-Two-Battery-413824.html>.
- [9] Kristofer Gryte, Richard Hann, Mushfiqul Alam, Jan Roháč, Tor Arne Johansen, and Thor I Fossen. Aerodynamic modeling of the skywalker x8 fixed-wing unmanned aerial vehicle. In *2018 International Conference on Unmanned Aircraft Systems (ICUAS)*, pages 826–835. IEEE, 2018.
- [10] jojo. Types of drones – explore the different models of uav’s, ?? URL <http://www.circuitstoday.com/types-of-drones>.
- [11] Hobby King. Aerostar rvs 60a. URL https://hobbyking.com/nl_nl/aerostar-rvs-60a-electronic-speed-controller-w-reverse-function-and-5a-bec-2-6s.html.
- [12] Betsy Lillian. sensefly’s latest fixed-wing mapping drone is here, October, 2016. URL <https://nl.geekbuying.com/item/SHRC-H2-Locke-2K-WIFI-\FPV-RC-Quadcopter-RTF-White-Two-Battery-413824.html>.
- [13] David Lundström, Kristian Amadori, and Petter Krus. Validation of models for small scale electric propulsion systems. In *48th AIAA Aerospace Sciences Meeting Including the New Horizons Forum and Aerospace Exposition*, page 483, 2010.
- [14] Lygte. Molicel inr21700-p42a 4200mah (gray). URL [https://lygte-info.dk/review/batteries2012/Molicel%20INR21700-P42A%204200mAh%20\(Gray\)%20UK.html](https://lygte-info.dk/review/batteries2012/Molicel%20INR21700-P42A%204200mAh%20(Gray)%20UK.html).
- [15] Rioku. Skywalker x8 drone, 2018. URL <http://www.regimage.org/skywalker-x8-drone/>.
- [16] Birute Ruzgiene. Requirements for aerial photography. page 79, 12 2004.
- [17] Helmut Schenk. Propeller calculator, ?? URL <http://www.drivecalc.de/PropCalc/>.
- [18] Steve Miller Zhao Wang. Electric aircraft model in simscape, 2018. URL <https://www.mathworks.com/matlabcentral/fileexchange/64991>.

A

Components

Turnigy Aerodrive SK3 - 4250-500kv Brushless Outrunner Motor



SKU: SK3-4250-500

425 g

Config Table

K_v	500 RPM/V
Weight	269 g
Max Current	57 A
Max Voltage	19 V
Power	1350 W
Internal resistance	18 mohm
Shaft (A)	5 mm
Length (B)	58 mm
Diameter (C)	42 mm
Can Length (D)	34 mm
Total Length (E)	80 mm

Figure A.1: Motor - Turnigy Aerodrive SK3 - 4250-500kv specifications

pixhawk[®] 4 mini

The power of Pixhawk[®] 4 in a compact form

Product Features

- Half the footprint of the *Pixhawk[®] 4*
- The same FMU processor and memory resources as the *Pixhawk 4*
- Aluminum casing for great thermal performance
- Easy to connect to commercial ESCs
- The latest sensor technology from Bosch[®] and InvenSense[®]
- Redundant IMUs for reliable performance
- NuttX real-time operating system
- Pre-installed with the most recent PX4 firmware



The *Pixhawk[®] 4 Mini* autopilot is designed for engineers and hobbyists who are looking to tap into the power of *Pixhawk 4* but are working with smaller drones. *Pixhawk 4 Mini* takes the FMU processor and memory resources from the *Pixhawk 4* while eliminating normally unused interfaces. This allows the *Pixhawk 4 Mini* to be small enough to fit in a 250mm racer drone. The *Pixhawk 4 Mini* is easy to install; the 2.54mm (0.1in) pitch connector makes it easier to connect the 8 PWM outputs to commercially available ESCs.

Pixhawk 4 Mini was designed and developed in collaboration with Holybro[®] and Auteiron[®]. It is based on the Pixhawk FMUv5 design standard and is optimized to run PX4 flight control software.

Figure A.2: Auto pilot - Pixhawk 4 mini specifications

TURNIGY Manual for Brushless Motor Speed Controller

Thank you for purchasing our Electronic Speed Controller (ESC). High power systems (or RC model) can be very dangerous; we strongly suggest you read this manual carefully. We have no control over the correct use, installation, application, or maintenance of our products; no liability shall be assumed for any damages, losses or costs resulting from the use of the product. Any claims arising from the operation, failure or malfunctioning etc. will be denied. We assume no liability for personal injury, property damage or consequential losses resulting from our product or our workmanship. As far as is legally permitted, the obligation of compensation is limited to the invoice amount of the affected product.

- **Features:**
 - Lithium battery Balance Discharge Monitoring and Protecting (BDM) Design, monitors in real time the discharge voltage of each lithium (Li-ion/Li-Poly) cell in a battery pack. Don't worry about the over discharge problem again, your lithium battery pack will have a much longer life. (Remark: This BDM function is ONLY available for "SENTRY" series ESC)
 - Full protection features: Low-voltage cutoff protection / Over-heat protection / Throttle signal lost protection
 - Extreme low resistance, high current endurance.
 - 3 different throttle modes: Throttle neutral, Throttle forward and Throttle reverse
 - Throttle range can be configured, fully compatible with all kinds of servable transmitters.
 - Smooth and accurate speed control, excellent throttle linearity.
 - Microprocessor uses separate voltage regulator IC (except PULSAR-6A and PULSAR-10A) with high anti-jamming capability.
 - Supports up to: 210000 RPM (2 poles), 70000 RPM (12 poles), 35000 RPM (12 poles) motors.
 - The program card is a very small device which can be purchased additionally for easy programming the ESC in the field.
 - With a program card, you can activate the music playing function of ESC, and there are 15 songs can be selected.

Specifications:

Class	Model	PULSAR Series				Balance Discharge Protection	Weight	Size L*W*H		
		Cont. Current (-1lb)	Burst Current (-1lb)	BEC Output	Battery Cell Li-Ion/ NiMH					
6A	PULSAR-6	6A	8A	Linear 5V/2A	2-4	5-12	Available	N/A	68	24*12*6
10A	PULSAR-10	10A	12A	Linear 5V/2A	2-4	5-12	Available	N/A	9g	27*17*6
12A	PULSAR-12	12A	15A	Linear 5V/2A	2-4	5-12	Available	N/A	19g	32*29*6
18A	PULSAR-18	18A	22A	Linear 5V/2A	2-4	5-12	Available	N/A	13g	32*24*10
25A	PULSAR-25	25A	35A	Linear 5V/2A	2-4	5-12	Available	N/A	21g	45*24*11
30A	PULSAR-30	30A	35A	N/A	N/A	2-4	5-12	Available	N/A	45*24*11
40A	PULSAR-40	40A	40A	Linear 5V/2A	2-4	5-12	Available	N/A	23g	45*28*11
40A	PULSAR-40-OTTO	40A	55A	N/A	N/A	2-6	5-18	Available	N/A	55*28*12
60A	PULSAR-60	60A	80A	Switch 5V/2A	2-6	5-18	Available	N/A	33g	55*29*11
60A	PULSAR-60-OTTO	60A	80A	N/A	N/A	2-6	5-18	Available	N/A	70*31*14
80A	PULSAR-80	80A	100A	Switch 5V/2A	2-6	5-18	Available	N/A	59g	70*31*14
80A	PULSAR-80-OTTO	80A	100A	N/A	N/A	2-6	5-18	Available	N/A	70*31*13

Class	Model	SENTRY Series				Balance Discharge Protection	Weight	Size L*W*H	
		Cont. Current (-1lb)	Burst Current (-1lb)	BEC Output	Battery Cell Li-Ion/ NiMH				
18A	SENTRY-18	18A	22A	Linear 5V/2A	2-4	5-12	Available	24g	45*28*11
25A	SENTRY-25	25A	30A	Linear 5V/2A	2-4	5-12	Available	27g	45*26*12
30A	SENTRY-30	30A	40A	Linear 5V/2A	2-4	5-12	Available	29g	45*26*12
40A	SENTRY-40	40A	55A	Switch 5V/2A	2-6	5-18	Available	40g	55*28*15
60A	SENTRY-60	60A	80A	Switch 5V/2A	2-6	5-18	Available	65g	70*31*14
80A	SENTRY-80	80A	100A	Switch 5V/2A	2-6	5-18	Available	67g	70*31*14

Class	Model	BASIC Series				Balance Discharge Protection	Weight	Size L*W*H	
		Cont. Current (-1lb)	Burst Current (-1lb)	BEC Output	Battery Cell Li-Ion/ NiMH				
18A	BASIC-18	18A	22A	Linear 5V/2A	2-4	5-12	Available	24g	45*26*11
25A	BASIC-25	25A	35A	Linear 5V/2A	2-4	5-12	Available	27g	45*26*12

BEC Output Capability

Standard micro servos(Max)	2S Li-Poly	5	3S Li-Poly	4	4S Li-Poly	3	5S Li-Poly	2	2S - 4S Li-Poly	5	5S Li-Poly	4
----------------------------	------------	---	------------	---	------------	---	------------	---	-----------------	---	------------	---

Linear Mode BEC(5V/2A) Switch Mode BEC(5V/2A)

IMPORTANT! The ESC named "BASIC" have a built-in BEC, so an UBEC (Ultra-Buck-ELEC) or an individual battery pack should be used to power the receiver. And an individual battery pack is needed to power the program card when setting the

TURNIGY Manual for Brushless Motor Speed Controller

programmable value of ESC, please read the user manual of program card for reference.



Labels Battery Balance Discharge Monitoring and Protecting Adapter For "SENTRY" Series ESC. We provide 2 kinds of Lithium Battery Balance Discharge Monitoring and Protecting Adapters for user to choose.



VERY IMPORTANT! You MUST contact the adapter with the balance charge connector on battery pack BEFORE connecting the main power to ESC. And if you use balance-charge connectors on main power wires (input wires), please connect the black wire (negative polarity) BEFORE red wire (positive polarity). So the right sequence is: Balance discharge adapter - BLACK wire of main power - RED wire of main power

Features Explanation:

1. Brake Settings: Brake Enabled / Brake Disabled, default is Brake Disabled
2. Battery Types: Li-Ion(Li-ion or Li-Poly) / Ni-MH(NiMH or NiCd), default is Li-Ion.
3. Low Voltage Protection Mode(Cutoff Mode): Reducer / Cutoff Output Power, default is Medium.
4. Low Voltage Protection Threshold(Cutoff Threshold): Low / Medium / High, default is Medium.
 - When using balance charge monitor and protecting function (i.e. Do NOT plug the balance charge connector into the balance-charge protecting socket on ESC, in this case, the ESC monitors not only the voltage of whole battery pack but also the voltage of each cell). For Li-Ion battery, low / medium / high cut off voltage for each cell are: 2.85V/2.8V/2.75V. For Ni-MH battery, low / medium / high cut off voltage for each cell are: 2.85V/2.8V/2.75V.
 - For Li-Ion battery, number of battery cells are calculated automatically. low / medium / high cutoff voltage for each cell are: 2.6V/2.65V/3.1V. For example: 3 cells Li-Poly, when medium cutoff voltage is set, the cutoff voltage is: 2.85*3=8.55V.
 - For Ni-MH battery, low / medium / high cutoff voltages are 0.6V/0.65V/0.68V. For example: 10 cells NiMH battery, fully charged voltage is 1.44*10=14.4V, when "medium" cutoff voltage is set, the cutoff voltage is: 14.4*5%-8.5V.
5. Startup Mode: Normal (ESC / Super-soft, default is Normal startup).
 - Normal is good for free-wing aircraft. Soft and Super-soft are good for helicopters. The initial speed of soft / super-soft mode is very slow, and the throttle stick is moved slowly with the motor. But if throttle is closed (throttle stick is moved to bottom) and opened again, throttle stick is moved slowly with the motor. The initial speed of soft / super-soft mode is very fast, and the throttle stick is moved slowly with the motor. The initial speed of soft / super-soft mode is very fast, and the throttle stick is moved slowly with the motor. The initial speed of soft / super-soft mode is very fast, and the throttle stick is moved slowly with the motor.
 - In normal cases, low timing can be used for most motors. But for high efficiency, we recommend the Low timing for 2 poles motor and medium timing for 6 poles and above. For higher speed, High timing can be chosen.
 - Timing: Low / Medium / High, default is Low.
6. Important: **Always your changing the timing setting, please test your RC model on ground firstly!**

Special Hint: Some high KV/out-turner motors have very special configuration, the space between each airfoil is very large, and lots of ESCs can't drive these motors. After updating the program of our ESCs, you can specify the name RC fans still have several questions about the programmable value for some special motors. So we just give some suggestions as follows:

Motor	Programmable Value Suggestion	Timing	Startup Mode
General in-turner motor		Low	Usually, aircraft uses "normal" startup mode
General out-turner motor		Low or Medium	Helicopter uses "super-soft" startup mode
Align 201E (Made in TAIWAN, out-turner)		High (MUST)	Soft (MUST)
ASHT (Made in TAIWAN, out-turner)		Low	Soft (MUST)

- English to Low Hour New ESC**
1. Please start up the ESC in the following sequence:
 2. Move the throttle stick to bottom position and then switch on the transmitter.
 3. Connect battery pack to ESC, the ESC begins the self-test process, a special tone " J 123" is emitted, which means the voltage of battery pack is in normal range, and then "N beep" tones will be emitted, the quantity of lithium battery cells. Finally a long "beep" tone will be emitted, which means self-test is OK, the aircraft/helicopter is ready to go flying.
 4. If nothing is happened, please check the battery pack and all the connections.

Figure A.3: Speed controller - Turnigy Plush 60

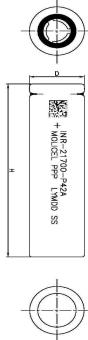
MOLICEL®
LITHIUM-ION RECHARGEABLE BATTERY

PRODUCT DATA SHEET
MODEL INR-21700-P42A

■ **CELL CHARACTERISTICS**

Capacity	Typical	4200 mAh
		15.5 Wh
	Minimum	4000 mAh
		14.7 Wh
Cell Voltage	Nominal	3.6 V
	Charge	4.2 V
	Discharge	2.5 V
Charge Current	Standard	4.2 A
Charge Time	Standard	1.5 hr
Discharge Current	Continuous	45 A
Typical Impedance	AC (1 KHz)	10 mΩ
	DC (10A/1s)	16 mΩ
Temperature	Charge	0°C to 60°C
	Discharge	-40°C to 60°C
Energy Density	Volumetric	615 Wh/l
	Gravimetric	230 Wh/kg

■ **PHYSICAL CHARACTERISTICS**

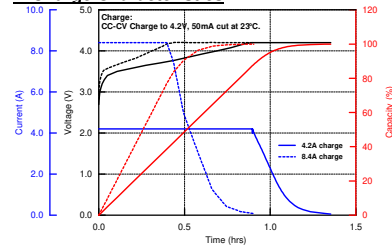


Shape	Cylindrical
Can	Steel
Diameter	21.7 mm (Max)
Height	70.2 mm (Max)
Weight	70 g (Max)

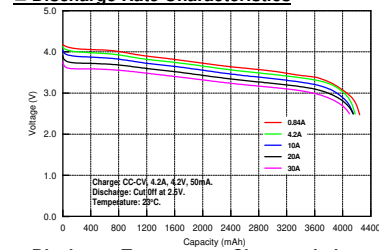
The information contained herein is for reference only and does not imply a performance guarantee or a product warranty. Specifications and characteristics are subject to change without prior notice.

For application specific information, please contact E-One Moli Energy Sales and Applications or the nearest MOLICEL® recognized agent.

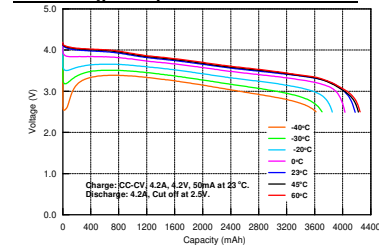
■ **Charge Characteristics**



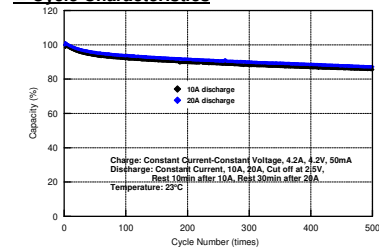
■ **Discharge Rate Characteristics**



■ **Discharge Temperature Characteristics**



■ **Cycle Characteristics**



■ **Taiwan Facility**
10 Dali 2nd Rd., Shan-Hwa, Tainan City, Taiwan, R.O.C.
Tel: 886-6-505-0866
Fax: 886-6-505-0777
mailto:service@molicel.com
http://www.molicel.com

■ **Canada Facility**
20 000 Stewart Crescent Maple Ridge, BC, Canada, V2X 9E7
Tel: 1-604-466-6654
Fax: 1-604-466-6600
mailto:molicel@molicel.com
http://www.molicel.com

■ **Headquarters**
10F, 113, Sec.2, Zhung Shan N Rd., Taipei, Taiwan, R.O.C.
Tel: 886-2-2567-3500
Fax: 886-2-2567-6500

Figure A.4: Battery cell - Molicel P42A specifications

BMS Specifications For 5S /18.5V Li-ion Battery Pack			
Model: LIM-5S1045L1606			
No.	Test item	Test item	Criterion
1	Voltage	Charging voltage	DC:21V CC/CV
		Balance voltage for single cell	4.180V ± 50 mV
2	Current	Balance current for single cell	80mA±10mA
		Current consumption for single cell	≤6μA
		Maximal continuous Charging current	10A
		Maximal continuous Discharging current	45A
3	Over charge Protection	Over charge detection voltage	4.25V \leq ±0.025V
		Over charge delay time	1S
		Over charge recovery voltage	4.15V \leq ±0.025V
4	Over discharge protection	Over discharge detection voltage	2.8V \leq ±0.1V
		Over discharge delay time	128ms
		Over discharge release voltage	3.0V \leq ±0.1V
5	Over current protection	Over current testing voltage	150mv \leq ± 15mv
		Over current detection current	90A± 10A
		Over current delay time	12MS
		Release condition	Automatic Recovery
6	Short protection	Detection condition	Exterior short circuit
		Detection delay time	≤300us
		Release condition	Automatic Recovery
7	Resistance	Protection circuitry (MOSFET)	≤20mΩ
8	Temperature	Operating Temperature Range	-40~+65°C
		Storage Temperature Range	-40~+ 125°C
9	Size		L60*W60*T9mm
10	Weight		30g

Figure A.5: Specifications battery protection component

B

Results

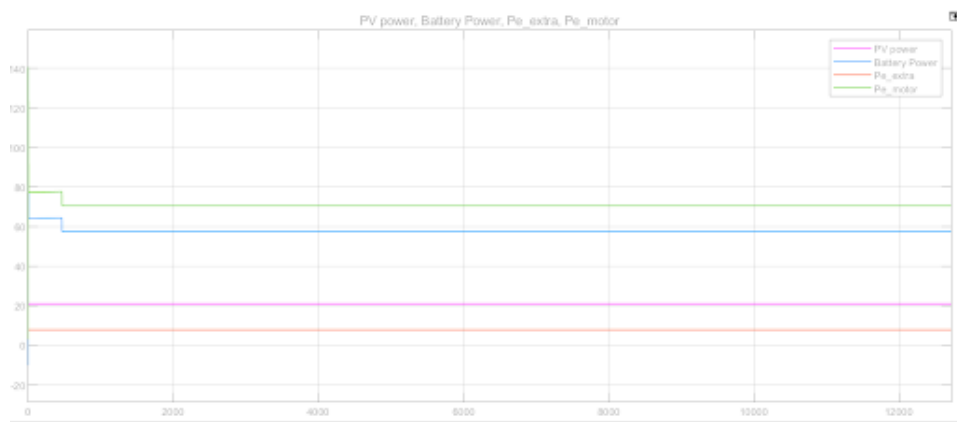


Figure B.1: Power distribution during flight

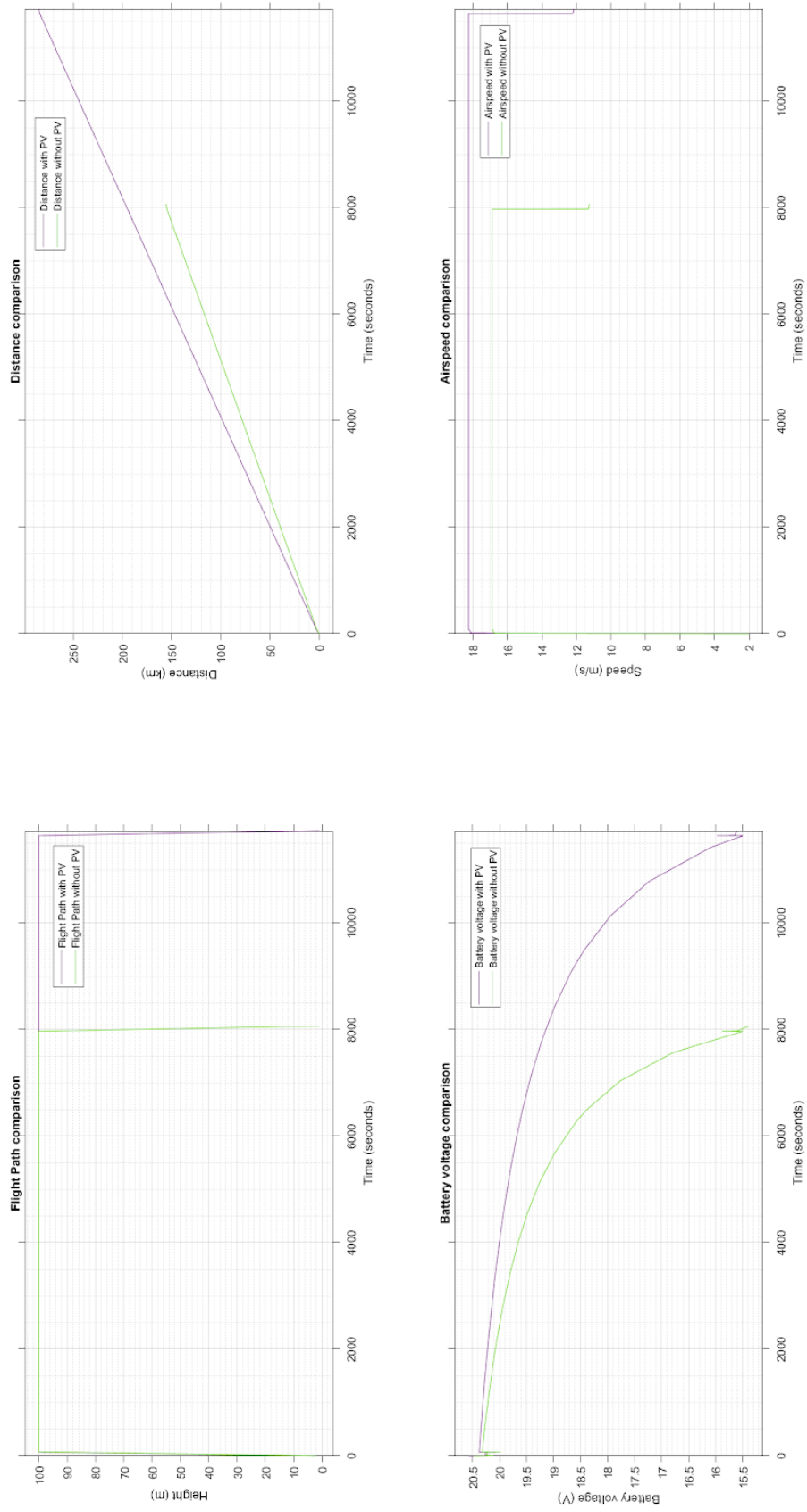


Figure B.2: Comparison between using PV panels and not using PV panels at a Solar irradiance of 782 W/m^2 and a Temp: 18.5 deg

C

Steady state analysis

A steady state analysis on the boost converter has been done. These calculations are a similar method to the one used by library. For the simplicity of calculation, it is assumed that the battery is detached.

MOSFET ON:

$$V_{PV} = L \frac{di}{dt} + i(R_L + R_{on}) \quad (C.1)$$

$$C \frac{dv_C}{dt} = -\frac{V_{out}}{R_{load}} \quad (C.2)$$

$$V_{out} = v_C \frac{R_{load}}{R_{load} + R_C} \quad (C.3)$$

$$\begin{bmatrix} \frac{di}{dt} \\ \frac{dv_C}{dt} \end{bmatrix} = \begin{bmatrix} \frac{-(R_L + R_{on})}{L} & 0 \\ 0 & -\frac{1}{(R_{load} + R_C)} \end{bmatrix} \cdot \begin{bmatrix} i \\ v_C \end{bmatrix} + \begin{bmatrix} \frac{1}{L} \\ 0 \end{bmatrix} V_{PV} = A_1 x + B_1 V_{PV} \quad (C.4)$$

$$V_{out} = q_1 x = \begin{bmatrix} 0 & \frac{R_{load}}{R_{load} + R_C} \end{bmatrix} x \quad (C.5)$$

MOSFET OFF:

$$V_{PV} = L \frac{di}{dt} + iR_L + V_{out} + V_D \quad (C.6)$$

$$i = C \frac{dv_C}{dt} + \frac{V_{out}}{R_{load}} \quad (C.7)$$

$$V_{out} = v_C \frac{R_{load}}{R_{load} + R_C} + i \frac{R_{load} R_C}{R_{load} + R_C} \quad (C.8)$$

$$\begin{bmatrix} \frac{di}{dt} \\ \frac{dv_C}{dt} \end{bmatrix} = \begin{bmatrix} \frac{-(R_L + \frac{R_{load} R_C}{R_{load} + R_C})}{L} & -\frac{R_{load}}{(R_{load} + R_C)L} \\ \frac{R_{load}}{(R_{load} + R_C)C} & -\frac{1}{(R_{load} + R_C)} \end{bmatrix} \cdot \begin{bmatrix} i \\ v_C \end{bmatrix} + \begin{bmatrix} \frac{1}{L} \\ 0 \end{bmatrix} (V_{PV} - V_D) = A_2 x + B_2 (V_{PV} - V_D) \quad (C.9)$$

$$V_{out} = q_2 x = \begin{bmatrix} \frac{R_{load} R_C}{R_{load} + R_C} & \frac{R_{load}}{R_{load} + R_C} \end{bmatrix} x \quad (C.10)$$

$$V_{out} = Ax + BV_{PV}, \quad (C.11)$$

$$\text{where } A = \frac{A_1 + A_2}{2} = A_1 D + (1 - D)A_2 \text{ and } B = \frac{B_1 + B_2}{2} = B_1 D + (1 - D)B_2 \quad (C.12)$$

In steady state:

$$A = \begin{bmatrix} -\frac{D(R_L + R_{on}) + (1 - D)[R_L + \frac{R_{load} R_C}{R_{load} + R_C}]}{L} & -\frac{(1 - D)R_{load}}{(R_{load} + R_C)L} \\ \frac{(1 - D)R_{load}}{(R_{load} + R_C)C} & -\frac{1}{(R_{load} + R_C)C} \end{bmatrix} \quad (C.13)$$

$$\dot{x} = \begin{bmatrix} \frac{di}{dt} \\ \frac{dv_C}{dt} \end{bmatrix} = \begin{bmatrix} 0 \\ 0 \end{bmatrix} = A \begin{bmatrix} I \\ V_C \end{bmatrix} + BV_{PV} \quad (C.14)$$

$$X = \begin{bmatrix} I \\ V_C \end{bmatrix} = -A^{-1}BV_{PV} \quad (C.15)$$

$$A^{-1} = \frac{1}{\det(A)} \cdot \begin{bmatrix} \frac{1}{(R_{load} + R_C)C} & \frac{(1 - D)R_{load}}{(R_{load} + R_C)L} \\ -\frac{(1 - D)R_{load}}{(R_{load} + R_C)C} & -\frac{D(R_L + R_{on}) + (1 - D)[R_L + \frac{R_{load} R_C}{R_{load} + R_C}]}{L} \end{bmatrix} \quad (C.16)$$

$$\text{where } \frac{1}{\det(A)} = \frac{(R_{load} + R_C)^2 CL}{(R_L + R_{on}D)(R_{load} + R_C) + (1 - D)R_{load}(R_C + (1 - D)R_{load})} \quad (C.17)$$

Similarly, the input/output voltage relationship can be calculated as in Equation C.18. For the simplification of the inverse A matrix, matrix E is found as in Equation C.20. This is possible due to the fact that the bottom row in matrix B is equal to zero.

$$\frac{V_{out}}{V_{PV}} = -CEB, \quad (C.18)$$

$$\text{where } C = [0 \quad 1] \text{ and } E \text{ is } A^{-1} \text{ with the second column set to } 0 \text{'s} \quad (C.19)$$

$$E = \begin{bmatrix} -\frac{(R_{load} + R_C)L}{(R_L + R_{on}D)(R_{load} + R_C) + (1 - D)R_{load}(R_C + (1 - D)R_{load})} & 0 \\ -\frac{(1 - D)R_{load}(R_{load} + R_C)L}{(R_L + R_{on}D)(R_{load} + R_C) + (1 - D)R_{load}(R_C + (1 - D)R_{load})} & 0 \end{bmatrix} \quad (C.20)$$

The input/output voltage relation is then found as in Equation C.21.

$$\frac{V_{out}}{V_{pv}} = \frac{(1 - D)R_{load}(R_{load} + R_C)}{(R_L + R_{on}D)(R_{load} + R_C) + (1 - D)R_{load}(R_C + (1 - D)R_{load})} \quad (C.21)$$

D

Simulation models

D.1. PV model

D.1.1. Parameters

Parameters of the PV system under STC ($G = 1000W/m^2$, $T = 25^\circ C$)

- $N_c = 19$
- $R_s = 0.001386 \cdot N_c [\Omega]$
- $R_p = 4.7091 \cdot N_c [\Omega]$
- $A = 0.96737$
- $I_s = 1.402 \cdot 10^{-12} [A]$
- $V_{oc} = 0.724 \cdot N_c [V]$
- $I_{sc} = 6.43 [A]$
- $V_{mpp} = 0.634 \cdot N_c [V]$
- $I_{mpp} = 6.06 [A]$
- $P_{mpp} = 3.84 \cdot N_c [W]$

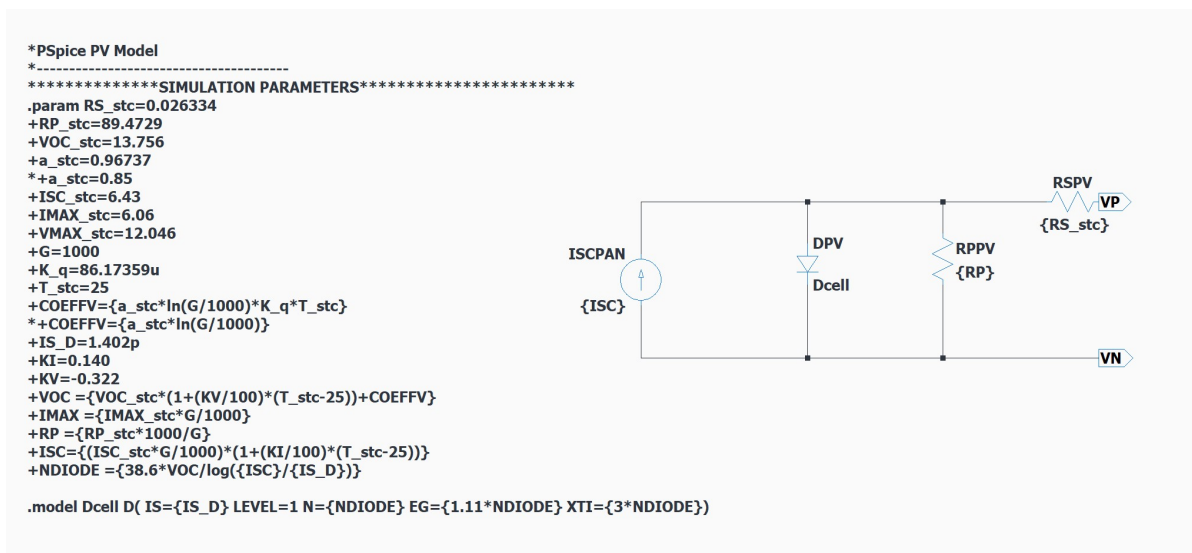
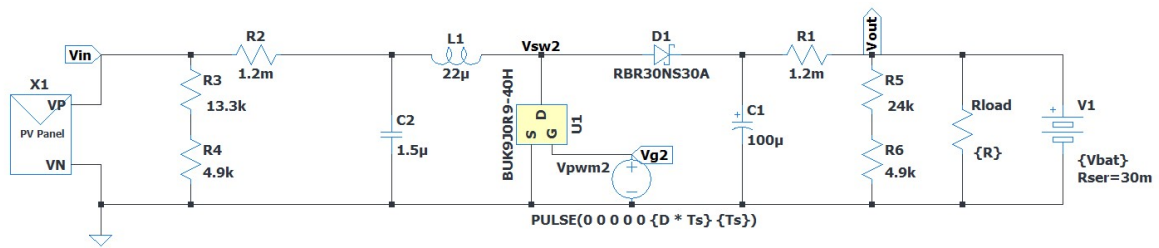


Figure D.1: The spice PV model used for the simulations

D.2. LT Spice Power Converter Model



PV System parameters

G={G}_T_stc=25 IS_D=1.402p KV=1 a_stc=0.96737

RS_stc=0.001386*{Cells} RP_stc=4.7091*{Cells} VOC_stc=0.724*{Cells} ISC_stc=6.43 IMAX_stc=6.06 VMAX_stc = 0.634*{Cells}

Simulation parameters

.param Ts=6.6u R=4.2 Cells=19

D 0 0.60 0.01 param G_50 1000 50 param Vbat 12.5 21 2.125

.tran 0 6m 5m

Figure D.2: LTSpice simulation model

D.3. Simulink General Simulation Model

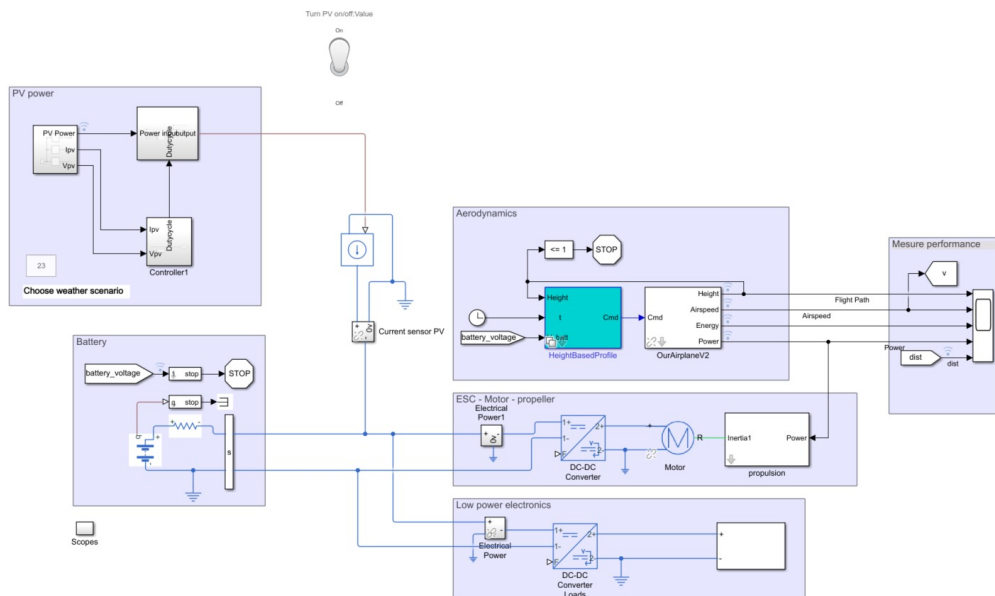


Figure D.3: Simulink general model for the UAV

D.4. Simulink Power Converter Model

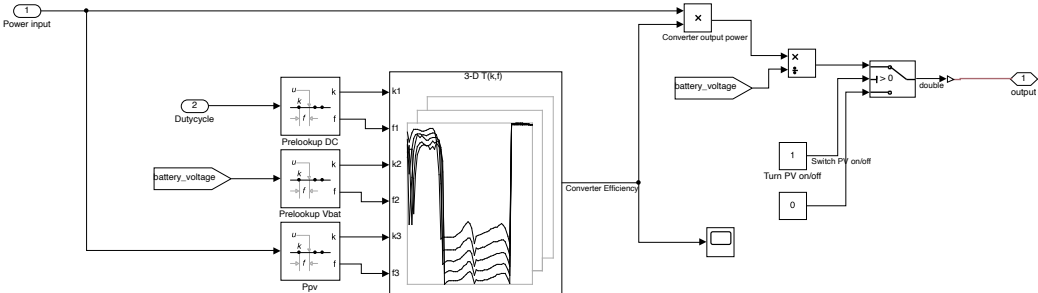


Figure D.4: Power converter simulink implementation

E

Codes

E.1. Data import

```
1 function [header, step_info, cycle_data] = import_data(file_name)
2 % Loads simulation data from LTSpice simulation
3 % IN:
4 %   - File name          [String]
5 % OUT:
6 %   - Header info       [String matrix]
7 %   - Step info         [
8 %                       Integer cell,
9 %                       - Duty cycles      [ /1000 ]
10 %                      - Irradiances     [ W/m^2 ]
11 %                      - Battery voltages [ Integer cell, V ]
12 %                       ]
13 %   - Cycle data        [ Double cell, simulation results]
14
15 %% Open file and check if successfull
16 [fid,msg] = fopen(file_name, 'rt');
17 assert(fid >= 3, msg)
18
19 %% Define file format
20 % Get simulation variables from header
21 header = fgetl(fid);
22 header = regexp(header, '\S+', 'match');
23
24 % Data format
25 format = repmat('%f', 1, numel(header));
26 options = {'CollectOutput', true};
27
28 %% Process
29 subheader = {};
30 cycle_data = {};
31
32 while ~feof(fid)
33     subheader{end+1} = fgetl(fid);
34     cycle_data(end+1) = textscan(fid, format, options{:});
35 end
36
37 fclose(fid);
```

```

38
39 %% Extract duty cycle
40 subheader = regexp(subheader, '(\d+)*', 'match');
41
42 step_info = [];
43 for i = 1:length(subheader)
44     step_info(1, i) = str2double(subheader{1, i}(1,1));
45     step_info(2, i) = str2double(subheader{1, i}(1,2));
46     if size(subheader{1, i},2) == 6
47         step_info(3, i) = str2num(string(char(subheader{1, i}(1,3)))
48             + "." + string(char(subheader{1, i}(1,4))));
49     else
50         step_info(3, i) = str2num(string(char(subheader{1, i}(1,3))));
51     end
52 end
53 end

```

E.2. Efficiency calculation

```

1 function [outputdata] = eff_power_avg(inputdata, header)
2 % Average efficiency by integrating the energie
3 %
4 %     inputdata      -> input data matrix with dimension: datatracks X
5 %     timestep       -> sample steps for new data
6 %     outputdata     -> output data matrix with dimension: datatracks X
7 %     samples/ratio
8
9 time = find(header == "time");
10 Vout = find(header == "V(vout)");
11 Vin = find(header == "V(vin)");
12 Iout = find(header == "I(R1)");
13 Iin = find(header == "Ix(x1:VP)");
14
15 steps = 1;
16
17 Ts = inputdata(end, time);
18 timestep = Ts/(steps+1);
19
20 %% calculate energy per time
21 % calculate P
22 Pin = -1*inputdata(:, Vin).*inputdata(:, Iin);
23 Pout = -1*inputdata(:, Vout).*inputdata(:, Iout);
24
25 %% calculate dt
26 time_temp(:, 1) = [0; inputdata(:, time)];
27 time_temp(:, 2) = [inputdata(:, time); 0];
28 time_temp(:, 3) = [inputdata(2:1:end, time); 0; 0];
29
30 time_mid = time_temp(:, 1:1:2) + diff(time_temp, 1, 2)/2;
31
32 dt = diff(time_mid, 1, 2);
33
34 Ttimes = table(time_temp, time_mid, dt);
35
36 %% calculate energy per time difference

```

```

36 Ein = 1;
37 Eout = 2;
38
39 E(:,Ein) = Pin.*dt(1:end-1);
40 E(:,Eout) = Pout.*dt(1:end-1);
41
42 %% sum energie
43
44 %cumtime = cumsum(inputdata(:,time));
45 %avgcumtime = cumtime./[1:1:length(cumtime)]';
46
47 E_sum = zeros(1,size(E,2));
48 time_sum = [];
49 points = [1];
50
51 for n = 1:steps
52     points(n+1) = find(inputdata(:,time) > n*timestep ,1) -1 ;
53
54     E_sum(n,:) = sum(E(points(n):points(n+1),:),1);
55     time_sum(n) = inputdata(points(n+1),time);
56 end
57
58 %% calculate efficiency
59 Eff = E_sum(:,Eout)./E_sum(:,Ein);
60 Pin_avg = round(2*E_sum(:,Ein)/Ts,1);
61
62 outputdata = [Pin_avg, Eff];

```

E.3. Data points to lookup conversion

```

1 %% Main Data Run
2 %
3 % By Martin & Jetserrr
4 clear all
5 close all
6
7 load lookupPE.mat
8
9 file_name = 'G_75_125_175.txt'; % give data filename to import
10
11 deletes = []; % skip this runs
12 stepvalues = [];
13
14 %% import data from file %%
15 [header, stepvalues ,data] = import_data(file_name);
16
17 %% column modus Jetse
18 time = find(header == "time");
19 Vout = find(header == "V(vout)");
20 Vin = find(header == "V(vin)");
21 Iout = find(header == "I(R1)");
22 Iin = find(header == "Ix(x1:VP)");
23
24 runs = size(data,2);
25 %runs = 10;
26
27 %% Calculate , downsample efficiencies -> save to matrix

```

```

28 results = {};
29
30 Pin = 1;
31 Eff = 2;
32
33 for i = 1:runs
34     if ismember(i, deletes)
35         results{1,i} = zeros(1,2);
36
37     else
38         results{1,i} = eff_power_avg(data{1,i},header);
39         % Results{1,i}(1, Eff)
40     end
41
42 end
43
44 %% Build lookup table
45 DC_lt = [0:0.01:0.60];
46 Vbat_lt = [12.5:2.125:21]; %just to know the indexes
47 Pin_lt = [0:0.1:75];
48
49 for i =1:runs
50     index_DC = (stepvalues(1,i)+10)/10;
51     index_Vbat = (stepvalues(3,i)-12.5)/2.125+1;
52     index_Pin = results{1,i}(1,Pin)*10+1;
53
54     lookup(index_DC,index_Vbat, index_Pin) = results{1,i}(1, Eff);
55 end
56
57 save('lookupPE.mat', 'lookup')
58
59 status = 'finished'
60
61 statussound(1)

```

E.4. Interpolation of the lookup matrix

```

1 load lookupPE.mat
2 % Counting the number of zeros
3 idx=lookup==0;out=sum(idx(:));
4 disp([num2str(100*out/numel(lookup)), '% of the points are zeros!'])
5
6 lookup_new = lookup;
7 % Step 1: substitute zeros with NaN
8 for i=1:61
9     for j=1:5
10        for k=1:729
11            if lookup(i,j,k)==0
12                lookup_new(i,j,k) = NaN;
13            end
14        end
15    end
16 end
17
18 % to visualize results, create 2-dimensional matrices.
19 % here, every matrix correspond to a battery voltage
20 lookup_1_buffer = reshape(lookup_new(:,1,:),61,729);

```

```

21 lookup_2_buffer = reshape(lookup_new(:,2,:),61,729);
22 lookup_3_buffer = reshape(lookup_new(:,3,:),61,729);
23 lookup_4_buffer = reshape(lookup_new(:,4,:),61,729);
24 lookup_5_buffer = reshape(lookup_new(:,5,:),61,729);
25
26 figure
27 s=surf(lookup_1_buffer);s.EdgeColor = 'r';s.FaceColor = 'r';s.FaceAlpha=1;
28 hold on
29 s=surf(lookup_2_buffer);s.EdgeColor = 'g';s.FaceColor = 'g';s.FaceAlpha=1;
30 s=surf(lookup_3_buffer);s.EdgeColor = 'b';s.FaceColor = 'b';s.FaceAlpha=1;
31 s=surf(lookup_4_buffer);s.EdgeColor = 'm';s.FaceColor = 'm';s.FaceAlpha=1;
32 s=surf(lookup_5_buffer);s.EdgeColor = 'y';s.FaceColor = 'y';s.FaceAlpha=1;
33 ylabel('Duty cycle index')
34 xlabel('Input Power index')
35 legend('V_b_a_t #1','V_b_a_t #2','V_b_a_t #3','V_b_a_t #4','V_b_a_t #5','
        location','southeast')
36 title('Very few points are not zero!!!')
37
38 figure
39 subplot(321)
40 s=surf(lookup_1_buffer);s.EdgeColor = 'r';s.FaceColor = 'r';s.FaceAlpha=1;
41 hold on
42 s=surf(lookup_2_buffer);s.EdgeColor = 'g';s.FaceColor = 'g';s.FaceAlpha=1;
43 s=surf(lookup_3_buffer);s.EdgeColor = 'b';s.FaceColor = 'b';s.FaceAlpha=1;
44 s=surf(lookup_4_buffer);s.EdgeColor = 'm';s.FaceColor = 'm';s.FaceAlpha=1;
45 s=surf(lookup_5_buffer);s.EdgeColor = 'y';s.FaceColor = 'y';s.FaceAlpha=1;
46 ylabel('Duty cycle index')
47 xlabel('Input Power index')
48 legend('V_b_a_t #1','V_b_a_t #2','V_b_a_t #3','V_b_a_t #4','V_b_a_t #5','
        location','southeast')
49
50 % Here, I try to fill all missing values (the zeros in your original
51 % matrix, now substituted with NaN) using a moving median filter along
52 % all
53 % the dimensions of your matrix.
54 % I do the moving median over 35 points in all dimensions because it is
55 % the
56 % lowest value that removes all the NaN. You can play with this value,
57 % and
58 % it can be different in the different dimensions. Perhaps, you do not
59 % need to remove all the NaN, since Simulink should not consider them
60 % when
61 % using the look up table.
62 lookup_new = fillmissing(lookup_new,'movmedian',35,1);
63 lookup_new = fillmissing(lookup_new,'movmedian',35,2);
64 lookup_new = fillmissing(lookup_new,'movmedian',35,3);
65
66 disp([num2str(sum(sum(sum(isnan(lookup_new))))), ' NaN remaining'])
67
68 % to visualize results, create 2-dimensional matrices.
69 % here, every matrix correspond to a battery voltage
70 lookup_1 = reshape(lookup_new(:,1,:),61,729);
71 lookup_2 = reshape(lookup_new(:,2,:),61,729);
72 lookup_3 = reshape(lookup_new(:,3,:),61,729);
73 lookup_4 = reshape(lookup_new(:,4,:),61,729);
74 lookup_5 = reshape(lookup_new(:,5,:),61,729);

```

```

71
72 i=2;
73 subplot(3,2,i)
74 i=i+1;
75 s=surf(lookup_1);s.EdgeColor = 'none';s.FaceColor = 'r';s.FaceAlpha=1;
76 ylabel('Duty cycle index')
77 xlabel('Input Power index')
78 hold on
79 subplot(3,2,i)
80 i=i+1;
81 s=surf(lookup_2);s.EdgeColor = 'none';s.FaceColor = 'g';s.FaceAlpha=1;
82 ylabel('Duty cycle index')
83 xlabel('Input Power index')
84 subplot(3,2,i)
85 i=i+1;
86 s=surf(lookup_3);s.EdgeColor = 'none';s.FaceColor = 'b';s.FaceAlpha=1;
87 ylabel('Duty cycle index')
88 xlabel('Input Power index')
89 subplot(3,2,i)
90 i=i+1;
91 s=surf(lookup_4);s.EdgeColor = 'none';s.FaceColor = 'm';s.FaceAlpha=1;
92 ylabel('Duty cycle index')
93 xlabel('Input Power index')
94 subplot(3,2,i)
95 i=i+1;
96 s=surf(lookup_5);s.EdgeColor = 'none';s.FaceColor = 'y';s.FaceAlpha=1;
97 ylabel('Duty cycle index')
98 xlabel('Input Power index')
99
100 figure
101 subplot(121)
102 s=surf(lookup_1_buffer);s.EdgeColor = 'r';s.FaceColor = 'r';s.FaceAlpha=1;
103 hold on
104 s=surf(lookup_2_buffer);s.EdgeColor = 'g';s.FaceColor = 'g';s.FaceAlpha=1;
105 s=surf(lookup_3_buffer);s.EdgeColor = 'b';s.FaceColor = 'b';s.FaceAlpha=1;
106 s=surf(lookup_4_buffer);s.EdgeColor = 'm';s.FaceColor = 'm';s.FaceAlpha=1;
107 s=surf(lookup_5_buffer);s.EdgeColor = 'y';s.FaceColor = 'y';s.FaceAlpha=1;
108 ylabel('Duty cycle index')
109 xlabel('Input Power index')
110 legend('V_b_a_t #1','V_b_a_t #2','V_b_a_t #3','V_b_a_t #4','V_b_a_t #5','
        location','southeast')
111
112
113 subplot(1,2,2)
114 s=surf(lookup_1);s.EdgeColor = 'none';s.FaceColor = 'r';s.FaceAlpha=1;
115 hold on
116 s=surf(lookup_2);s.EdgeColor = 'none';s.FaceColor = 'g';s.FaceAlpha=0.8;
117 s=surf(lookup_3);s.EdgeColor = 'none';s.FaceColor = 'b';s.FaceAlpha=0.6;
118 s=surf(lookup_4);s.EdgeColor = 'none';s.FaceColor = 'm';s.FaceAlpha=0.4;
119 s=surf(lookup_5);s.EdgeColor = 'none';s.FaceColor = 'y';s.FaceAlpha=0.2;
120 ylabel('Duty cycle index')
121 xlabel('Input Power index')

```

F

Datasheets

F.1. MOSFET datasheet



BUK9J0R9-40H

N-channel 40 V, 0.9 mΩ logic level MOSFET in LFPK56E

7 October 2019

Product data sheet

1. General description

Automotive qualified N-channel MOSFET using the latest Trench 9 low ohmic superjunction technology, housed in an enhanced LFPK56E package. This product has been fully designed and qualified to meet AEC-Q101 requirements delivering high performance and endurance.

2. Features and benefits

- Fully automotive qualified to AEC-Q101:
 - 175 °C rating suitable for thermally demanding environments
- Trench 9 Superjunction technology:
 - Reduced cell pitch enables enhanced power density and efficiency with lower R_{DSon} in same footprint
 - Improved SOA and avalanche capability compared to standard TrenchMOS
 - Tight $V_{GS(th)}$ limits enable easy paralleling of MOSFETs
- LFPK Gull Wing leads:
 - High Board Level Reliability absorbing mechanical stress during thermal cycling, unlike traditional QFN packages
 - Visual (AOI) soldering inspection, no need for expensive x-ray equipment
 - Easy solder wetting for good mechanical solder joint
- LFPK copper clip technology:
 - Improved reliability, with reduced R_{th} and R_{DSon}
 - Increases maximum current capability and improved current spreading

3. Applications

- 12 V automotive systems
- Motors, lamps and solenoid control
- Start-Stop micro-hybrid applications
- Transmission control
- Ultra high performance power switching

4. Quick reference data

Table 1. Quick reference data

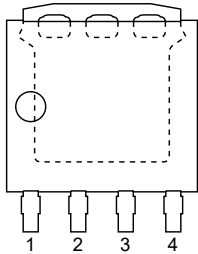
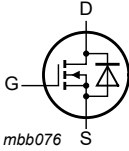
Symbol	Parameter	Conditions	Min	Typ	Max	Unit
V_{DS}	drain-source voltage	$25\text{ °C} \leq T_j \leq 175\text{ °C}$	-	-	40	V
I_D	drain current	$V_{GS} = 10\text{ V}; T_{mb} = 25\text{ °C};$ Fig. 2	[1]	-	220	A
P_{tot}	total power dissipation	$T_{mb} = 25\text{ °C};$ Fig. 1	-	-	500	W
Static characteristics						
R_{DSon}	drain-source on-state resistance	$V_{GS} = 10\text{ V}; I_D = 25\text{ A}; T_j = 25\text{ °C};$ Fig. 11	0.53	0.82	0.94	mΩ

Symbol	Parameter	Conditions	Min	Typ	Max	Unit
Dynamic characteristics						
Q_{GD}	gate-drain charge	$I_D = 25\text{ A}$; $V_{DS} = 20\text{ V}$; $V_{GS} = 4.5\text{ V}$; Fig. 13 ; Fig. 14	-	12.7	25.3	nC
Source-drain diode						
Q_r	recovered charge	$I_S = 25\text{ A}$; $di_S/dt = -100\text{ A}/\mu\text{s}$; $V_{GS} = 0\text{ V}$; [2] $V_{DS} = 20\text{ V}$; $T_j = 25\text{ }^\circ\text{C}$	-	52.6	-	nC
S	softness factor	$I_S = 25\text{ A}$; $di_S/dt = -100\text{ A}/\mu\text{s}$; $V_{GS} = 0\text{ V}$; $V_{DS} = 20\text{ V}$; $T_j = 25\text{ }^\circ\text{C}$; Fig. 17	-	0.77	-	

- [1] 220A continuous current has been successfully demonstrated during application tests. Practically the current will be limited by PCB, thermal design and operating temperature.
 [2] includes capacitive recovery

5. Pinning information

Table 2. Pinning information

Pin	Symbol	Description	Simplified outline	Graphic symbol
1	S	source	 <p>LPAK56E; Power-SO8 (SOT1023)</p>	 <p>mbb076</p>
2	S	source		
3	S	source		
4	G	gate		
mb	D	mounting base; connected to drain		

6. Ordering information

Table 3. Ordering information

Type number	Package		
	Name	Description	Version
BUK9J0R9-40H	LPAK56E; Power-SO8	plastic, single-ended surface-mounted package (LPAK56); 4 leads; 1.27 mm pitch	SOT1023

7. Marking

Table 4. Marking codes

Type number	Marking code
BUK9J0R9-40H	90H940E

8. Limiting values

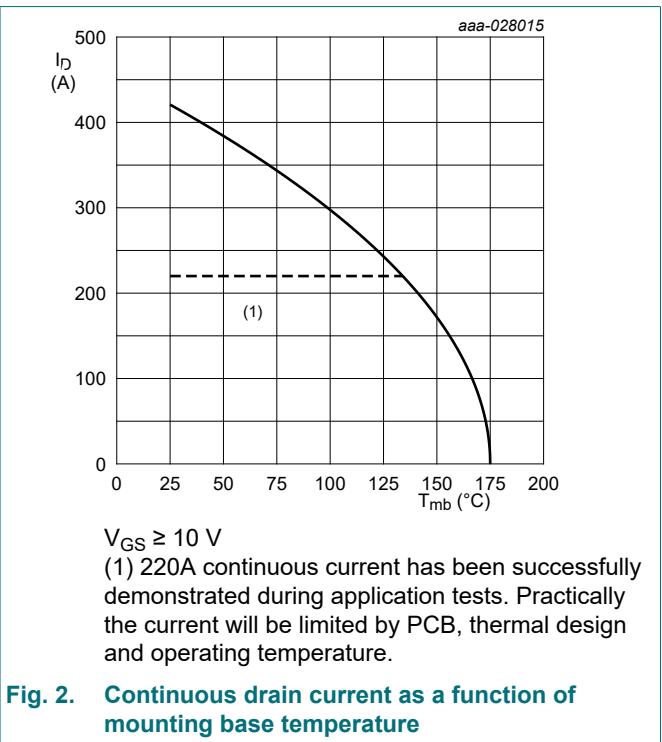
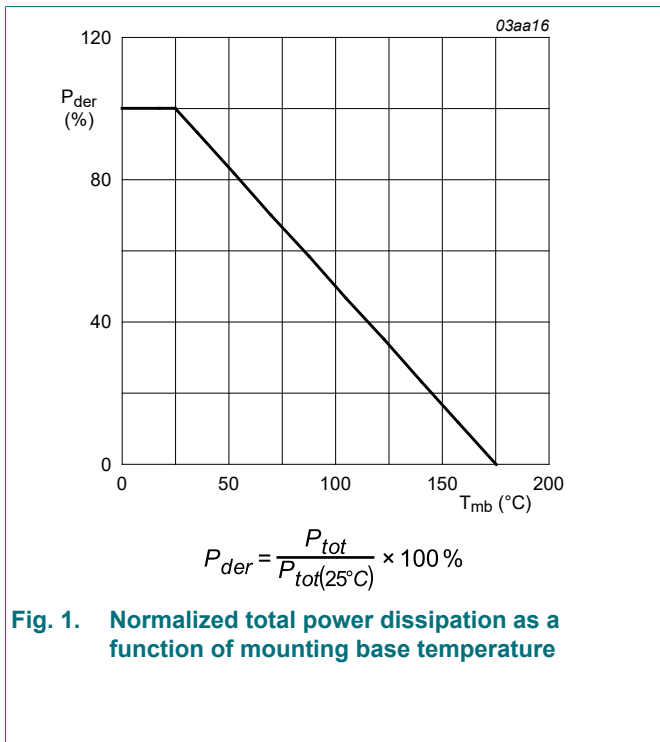
Table 5. Limiting values

In accordance with the Absolute Maximum Rating System (IEC 60134).

Symbol	Parameter	Conditions	Min	Max	Unit
V_{DS}	drain-source voltage	$25\text{ }^\circ\text{C} \leq T_j \leq 175\text{ }^\circ\text{C}$	-	40	V
V_{GS}	gate-source voltage	DC; $T_j \leq 175\text{ }^\circ\text{C}$	-10	16	V

Symbol	Parameter	Conditions		Min	Max	Unit
P _{tot}	total power dissipation	T _{mb} = 25 °C; Fig. 1		-	500	W
I _D	drain current	V _{GS} = 10 V; T _{mb} = 25 °C; Fig. 2	[1]	-	220	A
		V _{GS} = 10 V; T _{mb} = 100 °C; Fig. 2	[1]	-	220	A
I _{DM}	peak drain current	pulsed; t _p ≤ 10 μs; T _{mb} = 25 °C; Fig. 3		-	600	A
T _{stg}	storage temperature			-55	175	°C
T _j	junction temperature			-55	175	°C
Source-drain diode						
I _S	source current	T _{mb} = 25 °C	[2]	-	165	A
I _{SM}	peak source current	pulsed; t _p ≤ 10 μs; T _{mb} = 25 °C		-	600	A
Avalanche ruggedness						
E _{DS(AL)S}	non-repetitive drain-source avalanche energy	I _D = 160 A; V _{sup} ≤ 40 V; R _{GS} = 50 Ω; V _{GS} = 10 V; T _{j(init)} = 25 °C; unclamped; Fig. 4	[3] [4]	-	290	mJ

- [1] 220A continuous current has been successfully demonstrated during application tests. Practically the current will be limited by PCB, thermal design and operating temperature.
- [2] 165A continuous current has been successfully demonstrated during application tests. Practically the current will be limited by PCB, thermal design and operating temperature.
- [3] Single-pulse avalanche rating limited by maximum junction temperature of 175 °C.
- [4] Refer to application note AN10273 for further information.



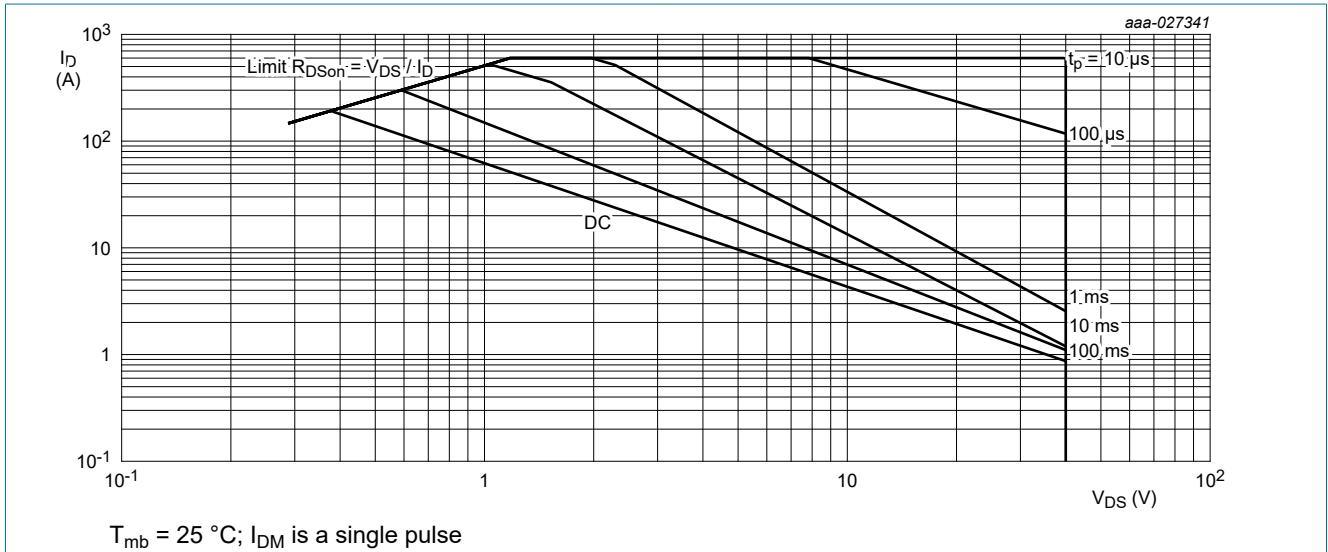


Fig. 3. Safe operating area; continuous and peak drain currents as a function of drain-source voltage

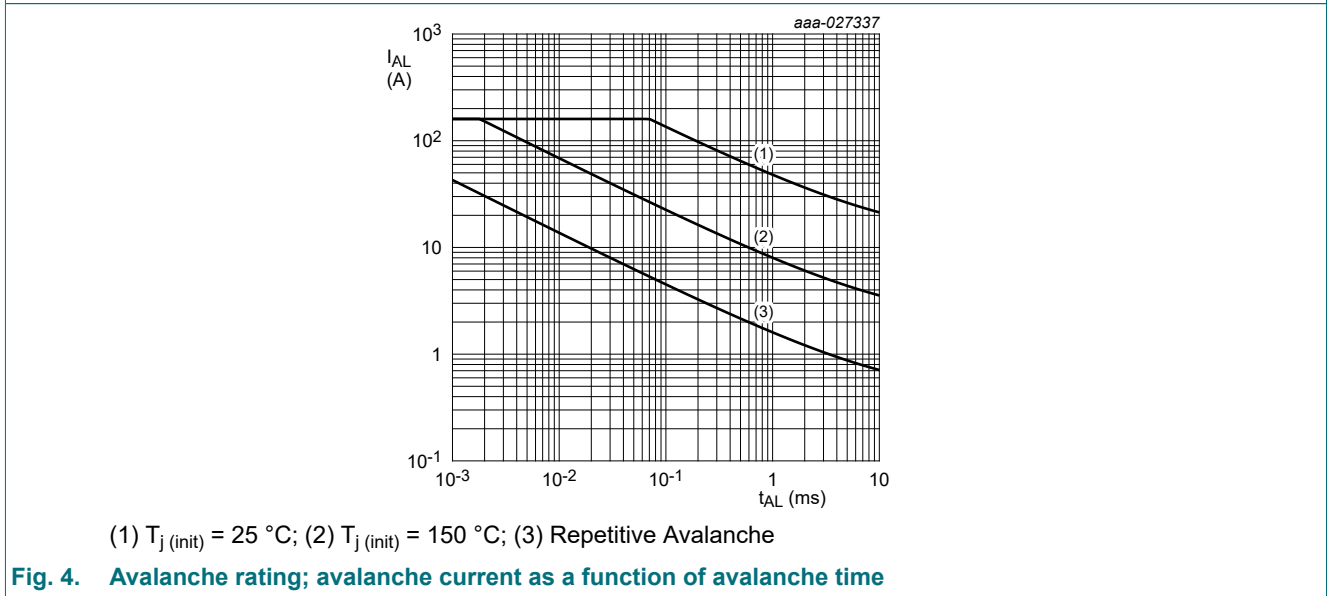


Fig. 4. Avalanche rating; avalanche current as a function of avalanche time

9. Thermal characteristics

Table 6. Thermal characteristics

Symbol	Parameter	Conditions	Min	Typ	Max	Unit
$R_{th(j-mb)}$	thermal resistance from junction to mounting base	Fig. 5	-	0.21	0.3	K/W

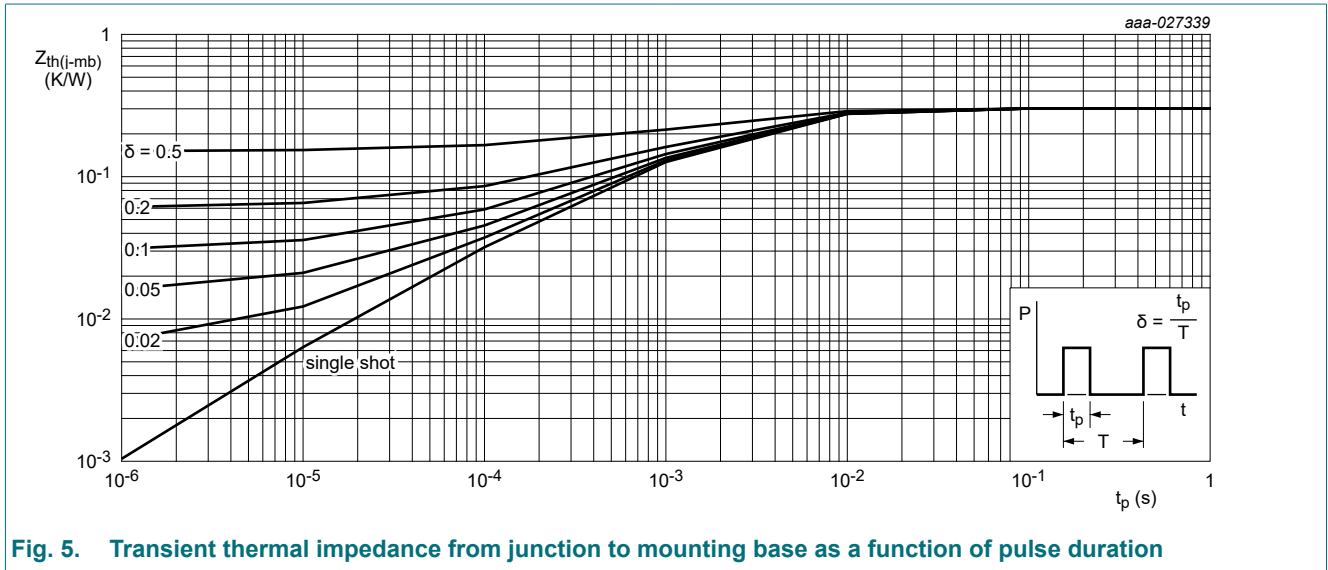


Fig. 5. Transient thermal impedance from junction to mounting base as a function of pulse duration

10. Characteristics

Table 7. Characteristics

Symbol	Parameter	Conditions	Min	Typ	Max	Unit
Static characteristics						
$V_{(BR)DSS}$	drain-source breakdown voltage	$I_D = 250 \mu A; V_{GS} = 0 V; T_J = 25 \text{ }^\circ C$	40	43	-	V
		$I_D = 250 \mu A; V_{GS} = 0 V; T_J = -40 \text{ }^\circ C$	-	40.5	-	V
		$I_D = 250 \mu A; V_{GS} = 0 V; T_J = -55 \text{ }^\circ C$	36	40	-	V
$V_{GS(th)}$	gate-source threshold voltage	$I_D = 1 \text{ mA}; V_{DS}=V_{GS}; T_J = 25 \text{ }^\circ C; \text{ Fig. 9}; \text{ Fig. 10}$	1.35	1.66	2.05	V
		$I_D = 1 \text{ mA}; V_{DS}=V_{GS}; T_J = 175 \text{ }^\circ C; \text{ Fig. 10}$	0.6	-	-	V
		$I_D = 1 \text{ mA}; V_{DS}=V_{GS}; T_J = -55 \text{ }^\circ C; \text{ Fig. 10}$	-	-	2.5	V
I_{DSS}	drain leakage current	$V_{DS} = 40 \text{ V}; V_{GS} = 0 \text{ V}; T_J = 25 \text{ }^\circ C$	-	0.4	5	μA
		$V_{DS} = 16 \text{ V}; V_{GS} = 0 \text{ V}; T_J = 125 \text{ }^\circ C$	-	3.2	25	μA
		$V_{DS} = 40 \text{ V}; V_{GS} = 0 \text{ V}; T_J = 175 \text{ }^\circ C$	-	405	1000	μA
I_{GSS}	gate leakage current	$V_{GS} = 16 \text{ V}; V_{DS} = 0 \text{ V}; T_J = 25 \text{ }^\circ C$	-	2	100	nA
		$V_{GS} = -10 \text{ V}; V_{DS} = 0 \text{ V}; T_J = 25 \text{ }^\circ C$	-	2	100	nA

N-channel 40 V, 0.9 mΩ logic level MOSFET in LPAK56E

Symbol	Parameter	Conditions	Min	Typ	Max	Unit
R _{DSon}	drain-source on-state resistance	V _{GS} = 10 V; I _D = 25 A; T _j = 25 °C; Fig. 11	0.53	0.82	0.94	mΩ
		V _{GS} = 10 V; I _D = 25 A; T _j = 105 °C; Fig. 12	0.79	1.17	1.48	mΩ
		V _{GS} = 10 V; I _D = 25 A; T _j = 125 °C; Fig. 12	0.87	1.29	1.64	mΩ
		V _{GS} = 10 V; I _D = 25 A; T _j = 175 °C; Fig. 12	1.1	1.63	2.05	mΩ
		V _{GS} = 4.5 V; I _D = 25 A; T _j = 25 °C; Fig. 11	0.68	0.97	1.2	mΩ
		V _{GS} = 4.5 V; I _D = 25 A; T _j = 105 °C; Fig. 12	1	1.47	1.9	mΩ
		V _{GS} = 4.5 V; I _D = 25 A; T _j = 125 °C; Fig. 12	1.1	1.62	2.1	mΩ
		V _{GS} = 4.5 V; I _D = 25 A; T _j = 175 °C; Fig. 12	1.4	2.03	2.6	mΩ
R _G	gate resistance	f = 1 MHz; T _j = 25 °C	0.42	1.04	2.6	mΩ
Dynamic characteristics						
Q _{G(tot)}	total gate charge	I _D = 25 A; V _{DS} = 20 V; V _{GS} = 10 V; Fig. 13 ; Fig. 14	-	120	168	nC
		I _D = 25 A; V _{DS} = 20 V; V _{GS} = 4.5 V; Fig. 13 ; Fig. 14	-	54.2	76	nC
Q _{GS}	gate-source charge		-	20.2	30.2	nC
Q _{GD}	gate-drain charge		-	12.7	25.3	nC
C _{iss}	input capacitance	V _{DS} = 25 V; V _{GS} = 0 V; f = 1 MHz; T _j = 25 °C; Fig. 15	-	8977	12568	pF
C _{oss}	output capacitance		-	1549	2168	pF
C _{rss}	reverse transfer capacitance		-	346	760	pF
t _{d(on)}	turn-on delay time	V _{DS} = 20 V; R _L = 0.8 Ω; V _{GS} = 4.5 V; R _{G(ext)} = 5 Ω	-	45.4	-	ns
t _r	rise time		-	46.2	-	ns
t _{d(off)}	turn-off delay time		-	59.2	-	ns
t _f	fall time		-	32.6	-	ns
Source-drain diode						
V _{SD}	source-drain voltage	I _S = 25 A; V _{GS} = 0 V; T _j = 25 °C; Fig. 16	-	0.76	1.2	V
t _{rr}	reverse recovery time	I _S = 25 A; dI _S /dt = -100 A/μs; V _{GS} = 0 V; V _{DS} = 20 V; T _j = 25 °C	-	44.6	-	ns
Q _r	recovered charge		[1]	-	52.6	-
S	softness factor	I _S = 25 A; dI _S /dt = -100 A/μs; V _{GS} = 0 V; V _{DS} = 20 V; T _j = 25 °C; Fig. 17	-	0.77	-	
		I _S = 25 A; dI _S /dt = -500 A/μs; V _{GS} = 0 V; V _{DS} = 20 V; T _j = 25 °C; Fig. 17	-	0.67	-	

[1] includes capacitive recovery

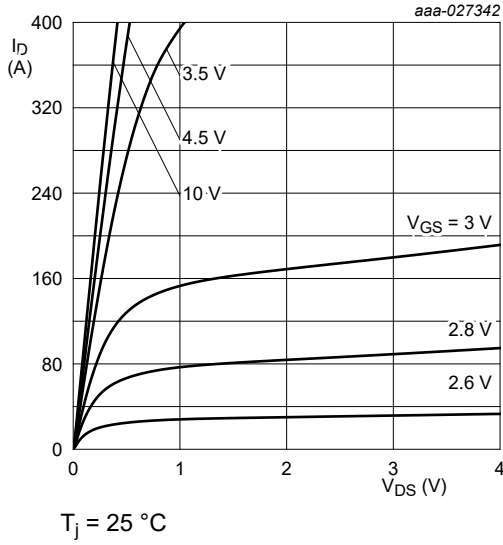


Fig. 6. Output characteristics; drain current as a function of drain-source voltage; typical values

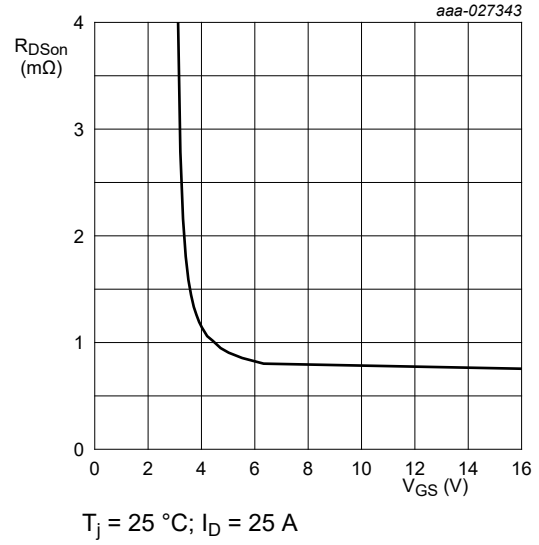


Fig. 7. Drain-source on-state resistance as a function of gate-source voltage; typical values

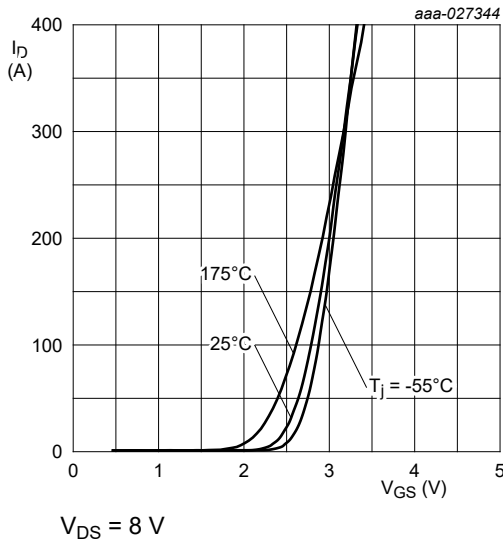


Fig. 8. Transfer characteristics; drain current as a function of gate-source voltage; typical values

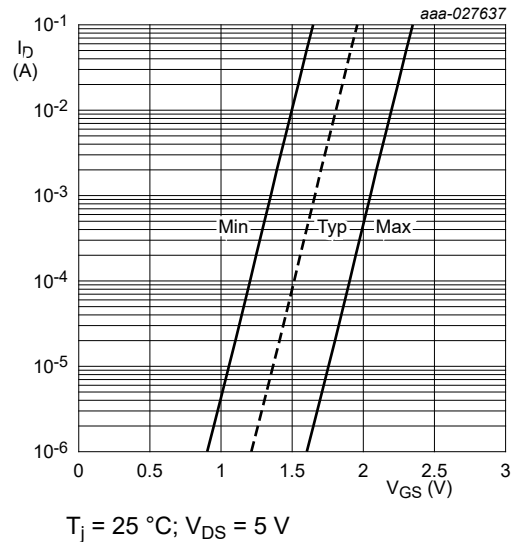


Fig. 9. Sub-threshold drain current as a function of gate-source voltage

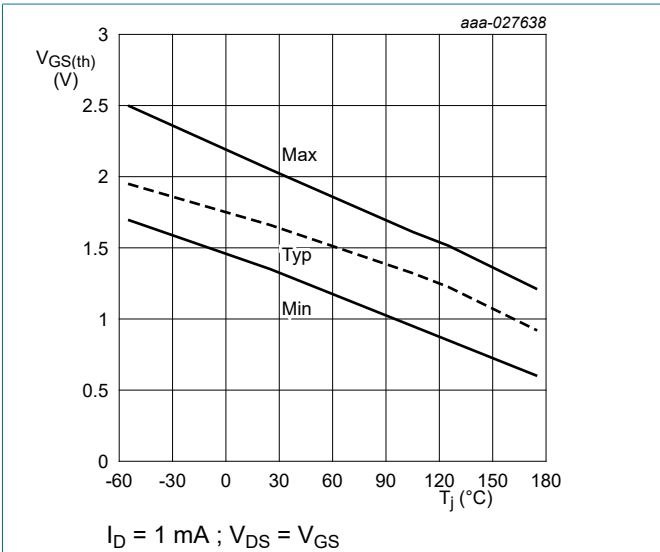


Fig. 10. Gate-source threshold voltage as a function of junction temperature

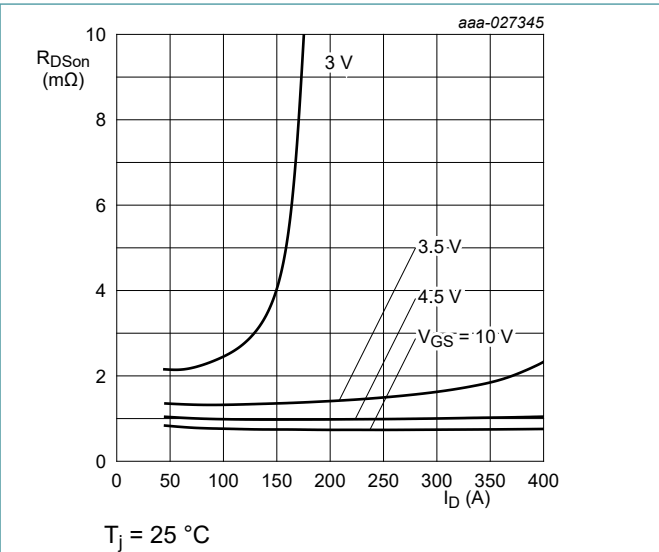


Fig. 11. Drain-source on-state resistance as a function of drain current; typical values

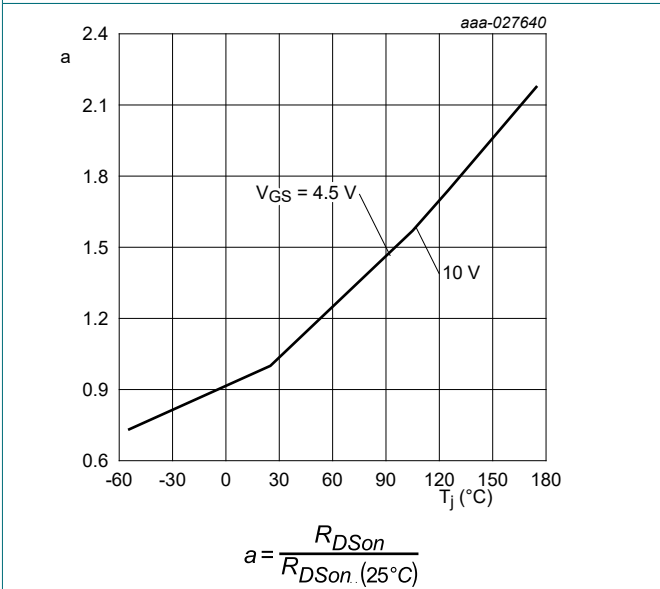


Fig. 12. Normalized drain-source on-state resistance factor as a function of junction temperature

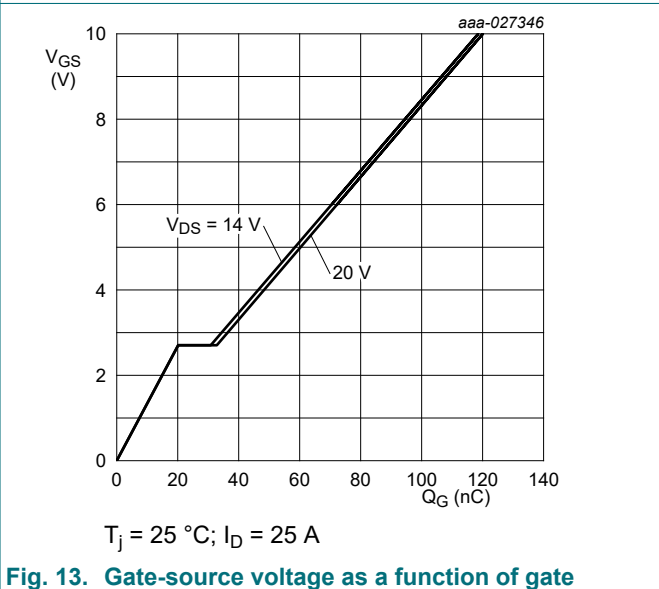


Fig. 13. Gate-source voltage as a function of gate charge; typical values

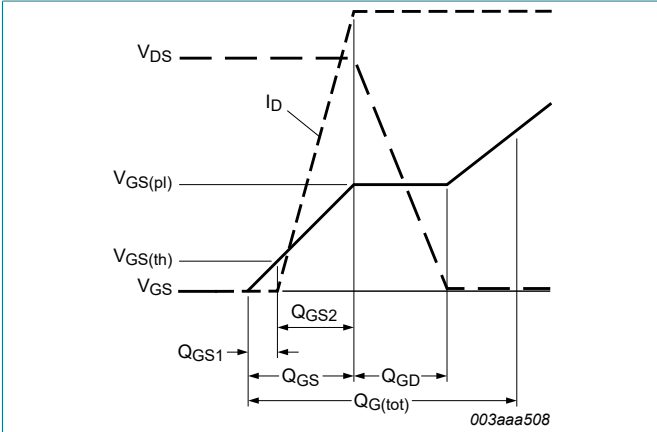


Fig. 14. Gate charge waveform definitions

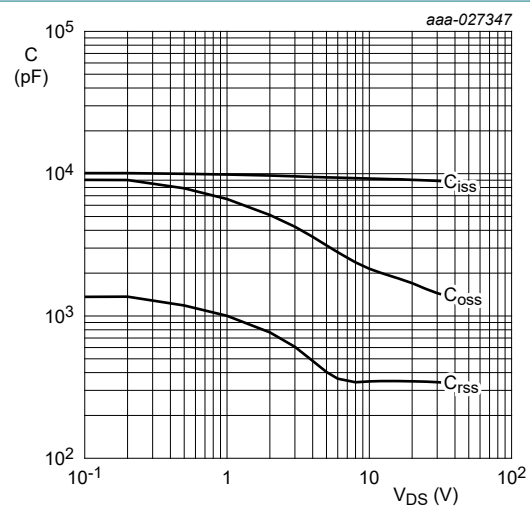


Fig. 15. Input, output and reverse transfer capacitances as a function of drain-source voltage; typical values

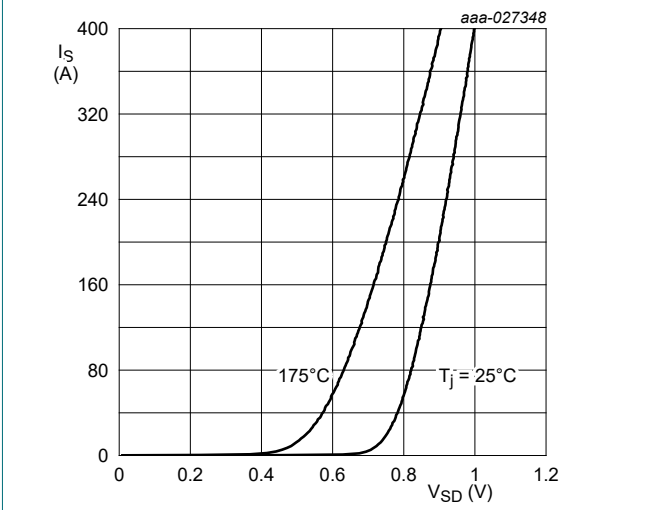


Fig. 16. Source-drain (diode forward) current as a function of source-drain (diode forward) voltage; typical values

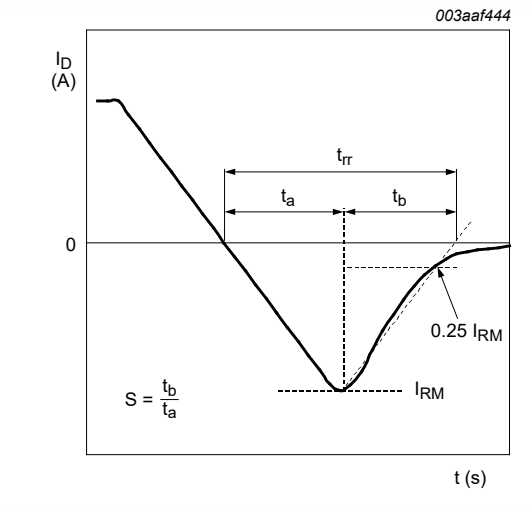


Fig. 17. Reverse recovery timing definition

11. Package outline

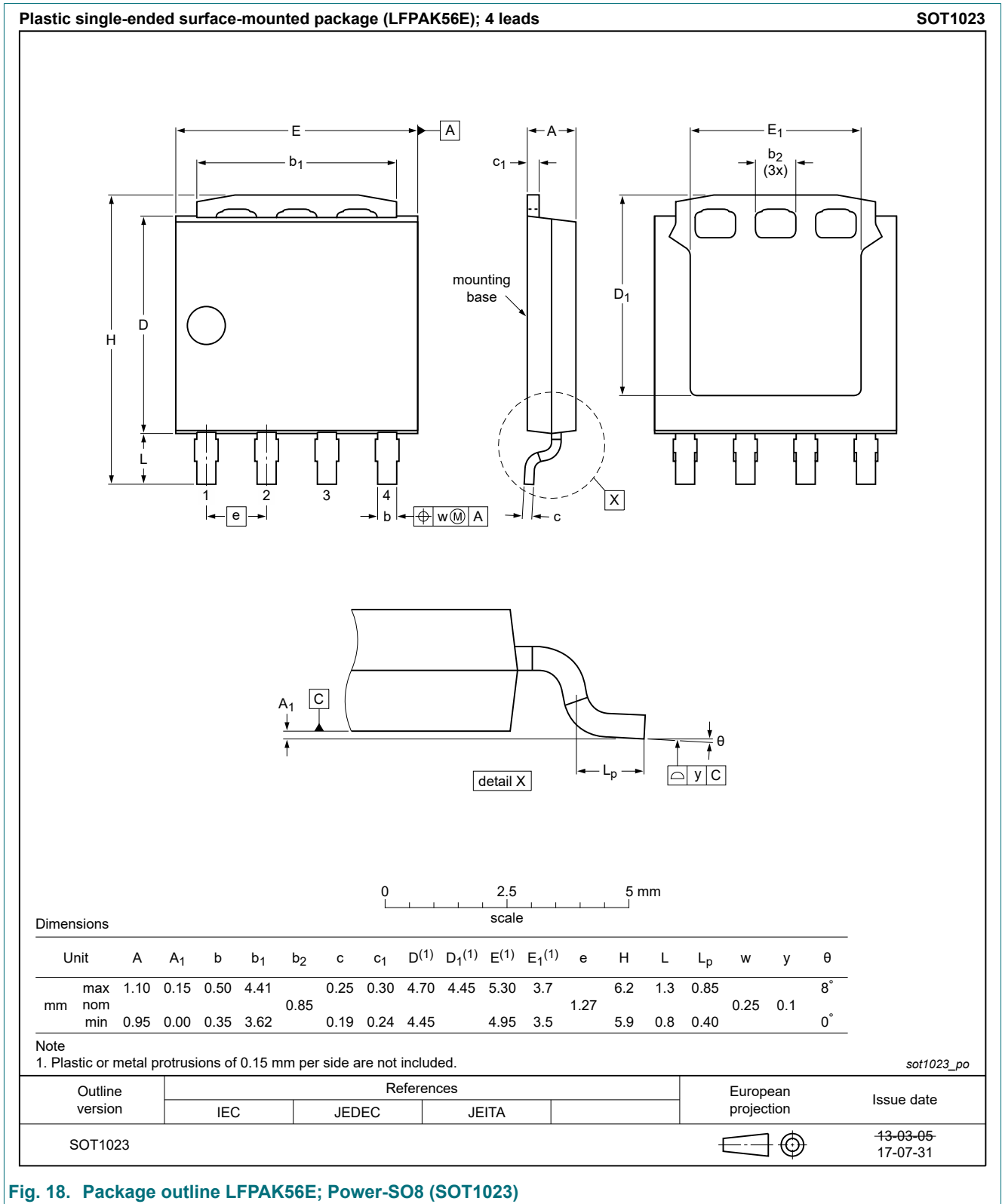


Fig. 18. Package outline LPAK56E; Power-SO8 (SOT1023)

12. Legal information

Data sheet status

Document status [1][2]	Product status [3]	Definition
Objective [short] data sheet	Development	This document contains data from the objective specification for product development.
Preliminary [short] data sheet	Qualification	This document contains data from the preliminary specification.
Product [short] data sheet	Production	This document contains the product specification.

- [1] Please consult the most recently issued document before initiating or completing a design.
- [2] The term 'short data sheet' is explained in section "Definitions".
- [3] The product status of device(s) described in this document may have changed since this document was published and may differ in case of multiple devices. The latest product status information is available on the internet at <https://www.nexperia.com>.

Definitions

Draft — The document is a draft version only. The content is still under internal review and subject to formal approval, which may result in modifications or additions. Nexperia does not give any representations or warranties as to the accuracy or completeness of information included herein and shall have no liability for the consequences of use of such information.

Short data sheet — A short data sheet is an extract from a full data sheet with the same product type number(s) and title. A short data sheet is intended for quick reference only and should not be relied upon to contain detailed and full information. For detailed and full information see the relevant full data sheet, which is available on request via the local Nexperia sales office. In case of any inconsistency or conflict with the short data sheet, the full data sheet shall prevail.

Product specification — The information and data provided in a Product data sheet shall define the specification of the product as agreed between Nexperia and its customer, unless Nexperia and customer have explicitly agreed otherwise in writing. In no event however, shall an agreement be valid in which the Nexperia product is deemed to offer functions and qualities beyond those described in the Product data sheet.

Disclaimers

Limited warranty and liability — Information in this document is believed to be accurate and reliable. However, Nexperia does not give any representations or warranties, expressed or implied, as to the accuracy or completeness of such information and shall have no liability for the consequences of use of such information. Nexperia takes no responsibility for the content in this document if provided by an information source outside of Nexperia.

In no event shall Nexperia be liable for any indirect, incidental, punitive, special or consequential damages (including - without limitation - lost profits, lost savings, business interruption, costs related to the removal or replacement of any products or rework charges) whether or not such damages are based on tort (including negligence), warranty, breach of contract or any other legal theory.

Notwithstanding any damages that customer might incur for any reason whatsoever, Nexperia's aggregate and cumulative liability towards customer for the products described herein shall be limited in accordance with the Terms and conditions of commercial sale of Nexperia.

Right to make changes — Nexperia reserves the right to make changes to information published in this document, including without limitation specifications and product descriptions, at any time and without notice. This document supersedes and replaces all information supplied prior to the publication hereof.

Suitability for use in automotive applications — This Nexperia product has been qualified for use in automotive applications. Unless otherwise agreed in writing, the product is not designed, authorized or warranted to be suitable for use in life support, life-critical or safety-critical systems or

equipment, nor in applications where failure or malfunction of an Nexperia product can reasonably be expected to result in personal injury, death or severe property or environmental damage. Nexperia and its suppliers accept no liability for inclusion and/or use of Nexperia products in such equipment or applications and therefore such inclusion and/or use is at the customer's own risk.

Quick reference data — The Quick reference data is an extract of the product data given in the Limiting values and Characteristics sections of this document, and as such is not complete, exhaustive or legally binding.

Applications — Applications that are described herein for any of these products are for illustrative purposes only. Nexperia makes no representation or warranty that such applications will be suitable for the specified use without further testing or modification.

Customers are responsible for the design and operation of their applications and products using Nexperia products, and Nexperia accepts no liability for any assistance with applications or customer product design. It is customer's sole responsibility to determine whether the Nexperia product is suitable and fit for the customer's applications and products planned, as well as for the planned application and use of customer's third party customer(s). Customers should provide appropriate design and operating safeguards to minimize the risks associated with their applications and products.

Nexperia does not accept any liability related to any default, damage, costs or problem which is based on any weakness or default in the customer's applications or products, or the application or use by customer's third party customer(s). Customer is responsible for doing all necessary testing for the customer's applications and products using Nexperia products in order to avoid a default of the applications and the products or of the application or use by customer's third party customer(s). Nexperia does not accept any liability in this respect.

Limiting values — Stress above one or more limiting values (as defined in the Absolute Maximum Ratings System of IEC 60134) will cause permanent damage to the device. Limiting values are stress ratings only and (proper) operation of the device at these or any other conditions above those given in the Recommended operating conditions section (if present) or the Characteristics sections of this document is not warranted. Constant or repeated exposure to limiting values will permanently and irreversibly affect the quality and reliability of the device.

Terms and conditions of commercial sale — Nexperia products are sold subject to the general terms and conditions of commercial sale, as published at <http://www.nexperia.com/profile/terms>, unless otherwise agreed in a valid written individual agreement. In case an individual agreement is concluded only the terms and conditions of the respective agreement shall apply. Nexperia hereby expressly objects to applying the customer's general terms and conditions with regard to the purchase of Nexperia products by customer.

No offer to sell or license — Nothing in this document may be interpreted or construed as an offer to sell products that is open for acceptance or the grant, conveyance or implication of any license under any copyrights, patents or other industrial or intellectual property rights.

Export control — This document as well as the item(s) described herein may be subject to export control regulations. Export might require a prior authorization from competent authorities.

Translations — A non-English (translated) version of a document is for reference only. The English version shall prevail in case of any discrepancy between the translated and English versions.

Trademarks

Notice: All referenced brands, product names, service names and trademarks are the property of their respective owners.

Contents

1. General description.....	1
2. Features and benefits.....	1
3. Applications.....	1
4. Quick reference data.....	1
5. Pinning information.....	2
6. Ordering information.....	2
7. Marking.....	2
8. Limiting values.....	2
9. Thermal characteristics.....	4
10. Characteristics.....	5
11. Package outline.....	10
12. Legal information.....	11

© Nexperia B.V. 2019. All rights reserved

For more information, please visit: <http://www.nexperia.com>
For sales office addresses, please send an email to: salesaddresses@nexperia.com
Date of release: 7 October 2019

Bibliography

- [1] Toshiba electronic devices storage corporation. *Please explain hard switching and soft switching using IGBTs*. https://toshiba.semicon-storage.com/ap-en/semiconductor/knowledge/faq/mosfet_igbt/igbt-012.html (cit. on p. 7).
- [2] Omid Naghash Almasi et al. “Analysis, control and design of a non-inverting buck-boost converter: A bump-less two-level T–S fuzzy PI control”. In: *ISA transactions* 67 (2017), pp. 515–527 (cit. on p. 6).
- [3] Jason Arrigo. “Input and output capacitor selection”. In: *SLTA055* (2006) (cit. on p. 16).
- [4] Laszlo Balogh. “Fundamentals of MOSFET and IGBT Gate Driver Circuits”. In: *Texas Instruments–Application report, SLUA618–March* (2017) (cit. on pp. 8, 9, 20).
- [5] *Buck Boost Converter image*. <https://riverglennapts.com/nl/converters/216-buck-boost-converter.html> [Online; accessed 11-May-2020] (cit. on p. 6).
- [6] Coilcraft. “Determining Inductor Power Losses”. In: *Coilcraft power conversion inductors; Document 486* (2018) (cit. on p. 15).
- [7] Robert W Erickson. “DC–DC power converters”. In: *Wiley encyclopedia of electrical and electronics engineering* (2001) (cit. on p. 5).
- [8] Texas Instruments. “Switching Regulator Fundamentals”. In: *Dallas, Texas. Texas Instruments Corporation* (2019) (cit. on pp. 5, 6).
- [9] Jasmijn Koning and Rik van der Hoorn. “PV generator”. In: *Solar powered drone* (2020) (cit. on pp. 2, 30).
- [10] Shodhganga library. “Boost Converter and its Performance Analysis”. In: (Year unknown) (cit. on p. 70).
- [11] Greg Lubarsky. “The forgotten converter”. In: *Texas Instruments Application Note, SLPY005* (2015) (cit. on p. 7).
- [12] Brian T Lynch. “Under the hood of a DC/DC boost converter”. In: *TI Power Supply Design Seminar*. Vol. 2009. 2008 (cit. on p. 5).
- [13] Sanjaya Maniktala. *Switching Power Supplies A-Z*. Elsevier, 2012 (cit. on pp. 15, 16).
- [14] M. Orellana et al. “Four Switch Buck-Boost Converter for Photovoltaic DC-DC power applications”. In: *IECON 2010 - 36th Annual Conference on IEEE Industrial Electronics Society*. 2010, pp. 469–474 (cit. on p. 6).
- [15] SK Parimala, MS Aspalli, and Laxmi Deshpande. “HIGH FREQUENCY DC-DC CONVERTER DESIGN USING ZERO VOLTAGE SWITCHING”. In: () (cit. on p. 7).
- [16] Jan M Rabaey, Anantha P Chandrakasan, and Borivoje Nikolić. *Digital integrated circuits: a design perspective*. Vol. 7. Pearson Education Upper Saddle River, NJ, 2003 (cit. on p. 7).
- [17] Michael Score. “Ceramic or electrolytic output capacitors in DC/DC converters—Why not both?” In: *Analog Appl. J., no. Texas Instruments* (2015), pp. 16–20 (cit. on p. 16).
- [18] MH Taghvaei et al. “A current and future study on non-isolated DC–DC converters for photovoltaic applications”. In: *Renewable and sustainable energy reviews* 17 (2013), pp. 216–227 (cit. on pp. 5–7).
- [19] Wikipedia contributors. *Single-ended primary-inductor converter Image—Wikipedia, The Free Encyclopedia*. https://en.wikipedia.org/w/index.php?title=Single-ended_primary-inductor_converter&oldid=950952709 [Online; accessed 17-May-2020]. 2020 (cit. on p. 7).